Master thesis and internship[BR]- Master's thesis : Towards simulations of supersonic oxygen blowing in steelmaking with OpenFOAM®[BR]- Internship

Auteur : Custine Colson, Léonore
Promoteur(s) : Terrapon, Vincent
Faculté : Faculté des Sciences appliquées
Diplôme : Master en ingénieur civil en aérospatiale, à finalité spécialisée en "aerospace engineering"
Année académique : 2023-2024
URI/URL : http://hdl.handle.net/2268.2/20938

Towards simulations of supersonic oxygen blowing in steelmaking with OpenFOAM®

Master's thesis completed in order to obtain the degree of
Master of Science in Aerospace Engineering
by Custine Colson Léonore

Supervisors:
Professor Vincent TERRAPON, *University of Liège*
Doctor Jean-Philippe THOMAS, *Soudobeam S.A.*

University of Liège
Faculty of Applied Sciences
Academic Year 2023-2024

Abstract

Seeking to reduce Europe's emissions, all the industrial processes are optimized. As steel is omnipresent in our lifestyles, making steel greener has become a key target. Steelmaking is a complex process subdivided into multiple stages. Each must be fully controlled to optimize the quality of the steel, the service life of the equipment, and reduce the required energy.
In this study, the conversion process of molten iron into steel inside the Basic Oxygen Furnace is investigated. This process is mainly driven by the blowing of supersonic oxygen jets onto molten iron. Understanding and being able to predict the behavior of the supersonic jets in this rough environment, and the way it penetrates the molten iron is mandatory for the process optimization. A great interest is thus paid to the modeling of these components. Simulations have already been conducted on licensed software. The objective of this paper is to develop this expertise with open source tools i.e., Gmsh and OpenFOAM®.

Hence a simplified model is considered to validate the tools. Firstly, a single supersonic jet in an atmosphere at room temperature is simulated. Then, a hot atmosphere at 1002K is introduced. The optimal simulation parameters are selected. The results are confronted to experimental, analytical and numerical references.

It is highlighted that structured meshes provide significantly more reliable results than unstructured ones. Moreover, the simulations with the $k-\varepsilon$ turbulence model estimate the most accurately the flow. In order to further improve the prediction, the standard C_μ value must however be adjusted for both cold and hot configurations. Due to the structure of OpenFOAM®, implementing a deep change of the model to take into account the temperature fluctuations is highly complex. Therefore, despite being less elegant, hard-coding the adjusted C_μ is selected. Additionally the tools to characterize and analyze the flow are developed. Particularly a new methodology of method validation is proposed to verify the model. Besides looking at the centerline quantities, the profiles at different axial distances are compared to observe self-similarity. Finally a first insight at the influence of the lance height and of the temperature on the flow, and thus on the oxidation, is highlighted.

The adequate parameters to model the flow are thus identified and further, more complex, simulations can be initiated. Particularly, a 3-dimensional simulation to consider the interactions between the multiple jets of the lance can be explored.

Keywords: Steelmaking, Basic Oxygen Furnace, CFD, open source tools, supersonic jets, hot atmosphere.

Contents

Nomenclature

$\cdot_{\text{amb}}$	Quantity in the ambiance	
$\cdot_{\text{core}}$	Quantity of the potential core	
$\cdot_{\text{ext}}$	Extrapolated quantity of the Richardson's interpolation	
$\cdot_{\text{in}}$	Quantity at the nozzle inlet	
$\cdot_{\text{out}}$	Quantity at the nozzle outlet	
$\cdot_{\text{sub}}$	Quantity of the subsonic zone	
$\cdot_{\text{super}}$	Quantity of the supersonic zone	
α	Dimensionless constant of the correlation of Sumi	–
β	Dimensionless constant of the correlation of Sumi	–
$\dot{m}_{\text{in}}$	Total inlet mass flow rate of the nozzle and the ambiance	$\mathrm{kg\,s^{-1}}$
$\dot{m}_{\text{out}}$	Total outlet mass flow rate of the ambiance	$\mathrm{kg\,s^{-1}}$
γ	Heat capacity ratio	–
κ	Proportionality constant	–
μ	Dynamic viscosity	$\mathrm{Pa\,s}$
ν_t	Turbulent viscosity	$\mathrm{m^2\,s^{-1}}$
$\overline{\rho}$	Dimensionless density, non-dimensionalized by ρ_{amb}	–
$\overline{r}$	Dimensionless radial distance, non-dimensionalized by D_{out}	–
$\overline{u}$	Dimensionless axial velocity, non-dimensionalized by U_{out}	–
$\overline{x}$	Dimensionless axial distance, non-dimensionalized by D_{out}	–
ϕ	Solution of interest of the Richardson's interpolation	
ψ	Refinement variations of the solution of interest of the Richardson's interpolation	
ρ	Density	$\mathrm{kg\,m^{-3}}$
ε	Turbulent kinetic energy dissipation rate	$\mathrm{m^2\,s^{-3}}$
a	Speed of sound	$\mathrm{m\,s^{-1}}$
a_0	First temperature constant of the JANAF tables	–
a_1	Second temperature constant of the JANAF tables	$\mathrm{K^{-1}}$
a_2	Third temperature constant of the JANAF tables	$\mathrm{K^{-2}}$
a_3	Fourth temperature constant of the JANAF tables	$\mathrm{K^{-3}}$
a_4	Fifth temperature constant of the JANAF tables	$\mathrm{K^{-4}}$

A_s	Coefficient of the Shuterland's law	$\mathrm{Pas}/\sqrt{\mathrm{K}}$
C_μ	Model coefficient for the turbulent viscosity	–
C_T	Coefficient of the Abdol-Hamid turbulence model, adapted by Alam	–
c_p	Heat ratio at constant pressure	$\mathrm{m^2\,s^{-2}\,K^{-1}}$
D	Nozzle diameter	m
e	Relative error on the mesh computed with the Richardson's interpolation	–
f	Refinement factor of the Richardson's interpolation	–
g	Apparent order of the Richardson's interpolation	–
$H(.)$	Heaviside function	–
h	Enthalpy	$\mathrm{kg\,m^2\,s^{-2}}$
JANAF	Joint Army–Navy–Air Force	
k	Turbulent kinetic energy	$\mathrm{m^2\,s^{-2}}$
M	Mach number	–
M_τ	Turbulent Mach number	–
$M_{\tau 0}$	Turbulent Mach number constant of the Abdol-Hamid turbulence model	–
N	Number of elements in the mesh	–
p	Static pressure	Pa
p^0	Total pressure	Pa
R	Gas constant	$\mathrm{m^2\,s^{-2}\,K^{-1}}$
r	radial coordinate	m
$r_{1/2}$	Half radius	m
RANS	Reynolds-averaged Navier–Stokes	
RNG	Renormalization Group	
S	Spreading rate of the jet	–
SST	Shear Stress Transport	
T	Static temperature	K
T^0	Total temperature	K
T_g	Local temperature dependant coefficient of the Abdol-Hamid turbulence model	–
T_s	Coefficient of the Shuterland's law	K
U	Axial velocity	$\mathrm{m\,s^{-1}}$
u^+	Mean velocity	–
U_c	Centerline axial velocity	$\mathrm{m\,s^{-1}}$

x	Axial coordinate	m
x_0	Virtual origin of the spreading of the jet	m
X_c	Dimensionless correlation parameter core length of the correlation of Witze	–
y^+	Dimensionless wall distance	–

List of Figures

List of Tables

Introduction

Tending towards sustainability has become one of the main targets of all industries. Particularly, as steel is omnipresent in our every day life, making steel greener is a key focus. The steelmaking industry therefore seeks to improve its process. This requires a better understanding of all aspects and the ability to predict, hence the development of models.

Steelmaking is a complex process, subdivided into different stages. The most common and the best controlled route is the Blast Furnace-Basic Oxygen Furnace. First, molten iron is obtained from coke, ores, and limestone in a Blast Furnace. Then it is refined in a Basic Oxygen Furnace. Finally, it is shaped and treated. In this study, the focus is on the refining of the steel in the Basic Oxygen Furnace. During this step, carbon and other impurities are removed from the molten iron to improve the steel quality and make it usable in industry. To oxidize the unwanted elements, supersonic jets of oxygen are blown onto and into the bath of molten iron. Numerous parameters influence the oxygen jet blowing, and thus the chemical reactions of steel conversion. For instance, the distance between the lance and the bath, and the ambiance temperature modify the blowing properties. Consequently the execution of the process is impacted. It is thus crucial to develop a deep understanding of the phenomena taking place to improve the process. In this regard, the behavior of the jet is investigated.

As this subject is at the core of current concerns, numerous experiments and simulations have already been conducted. However, the models are built with licensed software. This situation is increasingly seen as an obstacle for R&D departments. Commercial code is sometimes seen as a black box, leading to dependency on software publishers. More and more industries are therefore turning to open source code, despite the associated drawbacks: lack of support and lack of tool integration. Hence the aim of this paper is to develop this expertise on open source tools. Despite being more complex to handle, they offer more freedom to the user to customize the software to its own needs. Moreover, no license must be bought.
The selected open source tools are Gmsh [1] and OpenFOAM® [20]. Gmsh is a free software developed by Christophe Geuzaine and Jean-François Remacle. It allows to generate 3D finite element meshes. Here, both the geometry and the mesh are generated using this tool. The CFD software OpenFOAM® is used to simulate the flow. Two main versions of OpenFOAM® are available: the *.com* and the *.org* version. While the *.com* tends to be more commercial, the *.org* has stayed closer to its academical roots. Therefore, OpenFOAM®.org version 9 is used for these simulations.

In this paper, a model of a single supersonic jet in a hot atmosphere is developed with these open source tools. A simplified modeling of the BOF environment is thus achieved. This is the first step towards the development of a more complex modeling tool. To validate the model, it is compared to the results available in literature. Experimental, analytical, and numerical references are selected.

In Chapter 1, to better understand the benefits and the challenges, the industrial context is introduced. The steelmaking process is explained with a focus on the Basic Oxygen Furnace. A first characterization of supersonic jets is also presented.

Afterwards, in Chapter 2, the available results on which the validation is based are introduced. These include experimental, analytical, and numerical references.

The simulation of a cold supersonic jet in cold atmosphere is then started in Chapter 3. The reference experiments for this case have been carried out by Eggers [8]. Also, Witze has derived a correlation for the centerline axial velocity [9], and a reference simulation is available [11]. Those results are used as a comparison tool to validate the model. The case set-up is described and the choices are motivated. Their reliability is then verified by comparison with the references.

Subsequently, in Chapter 4, the hot atmosphere is considered. This corresponds to the experiments carried out by Sumi [16]. Additionally, as for the cold case, analytical and numerical results are available to further verify the results [10, 13]. Challenges associated to the high temperature gradients are highlighted. Their influence on the jet at different bath levels is investigated.

Finally, to conclude, an insight at the next steps of the simulation process is shared. As the models considered in this work assume a simplified environment, the paths of improvements are mentioned. The associated challenges that will arise are described.

1 Industrial Context

Moving towards sustainability is one of the main concern of the modern world. As steel is omnipresent in objects of the every day life, making it greener is a path that should be explored to reach the emissions target.

Determining the perspectives of improvements that can be made in the steelmaking process should therefore be investigated. Knowledge is thus gathered from literature. The focus is progressively then taken on a specific stage of the steelmaking process, the Basic Oxygen Furnace. The importance of the blowing for the smooth functioning of this operation is pointed out.

1.1 The steel industry

Steel is an alloy of iron and carbon. It is characterized by a carbon content of less than 0.5%. It is also composed of less than 1% of manganese and small amounts of oxygen, phosphorus, silicon and sulfur. Steel stands out for its strength, versatility, and infinite recyclability [21, 22].

Because of its properties, steel is omnipresent in every aspect of our lives. It is used in cars, ships and trains, in constructions products and tools, in households appliances, etc. In Europe, 140 million tonnes of steel are produced each year [21]. This represents 191 billion euros in gross value added. Thus the steel industry plays a significant role in modern economy.

Consequently, making steel greener is a current top priority to pursue sustainability [21]. This will indeed help Europe meet the objectives of carbon dioxide emissions reduction. Steel is already 100% recyclable. Therefore the focus is on improving the steelmaking process. Decreasing the greenhouse gases emissions, the energy consumption and the additional components quantity are thus the areas of improvements. The performance must be improved.

This study focuses on a specific stage of the steelmaking process. The overall process is described to understand the position of each step and highlight the role it can play to reach the target.

1.2 The steelmaking process

In Europe, two main routes are principally followed to produce steel: the Blast Furnace - Basic Oxygen Furnace and the Electric Arc Furnace routes. The former is often referred as "primary" path. It produces new steel. The latter, or "secondary' path, recycles steel scrap [21].

1.2.1 The Electric Arc Furnace route

The Electric Arc Furnace is represented in Figure 1.1. As mentioned, steel scrap is recycled during the process. However solidified iron can be added as well. Electric arcs are used to increase the temperature up to around 2000K and melt down the metal. Oxygen is then blown to remove impurities.

All kinds of steel can be produced via this route: basic, stainless or high alloyed special steels. Its flexibility is its main advantage. In a year, about 1.5 million tonnes of steel can be produced in an EAF. In Europe, this route is responsible for over 40% of the total production [21]. This method is interesting to reach sustainability. The instrumentation is however highly complex. Multiple types of fluids, oxygen and gas, are involved. Consequently numerous openings and fluid systems are present. Hence the route is not explored in this paper. The study of the Blast Furnace-Basic Oxygen Furnace is however applicable to this technology.

Figure 1.1: Illustration of an Electric Arc Furnace [2].

1.2.2 The Blast Furnace-Basic Oxygen Furnace route

The "primary" path is considered in the current study. Its main advantages with respect to the Electric Arc Furnace are numerous. First scrap, which is hard to find, is not required for the operation. Moreover, since the composition of scrap is not known, the inputs are fully controlled. Finally this process is mastered. The level of carbon content can be precisely controlled and the phosphorus level significantly lowered. This is very useful for cutting-edge industries, for instance the deep-drawing in the automotive industry.

The process is represented in Figure 1.2. The operation is as follows: extraction and preparation of the raw materials, reduction in the Blast Furnace, oxidation in the Basic Oxygen Furnace, and casting and treatments [23, 21].

Firstly the raw materials involved in the process are thus extracted. These include iron ores, limestone, and coal. They must then be treated to be usable. Impurities that could be harmful are indeed contained. Iron ores are transformed into pellets or sinter, and the coal into coke.

Afterwards those components are placed in the Blast Furnace. Hot air reacts with the coke and produces a reducing gas. Successively the oxygen is extracted from the iron in the form

of carbon dioxide. With this reduction reaction, pig iron is obtained. These reactions are exothermic. Temperatures up to 1600K are reached. Iron thus melts. Within 5 hours, 600 tons of pig iron is obtained.

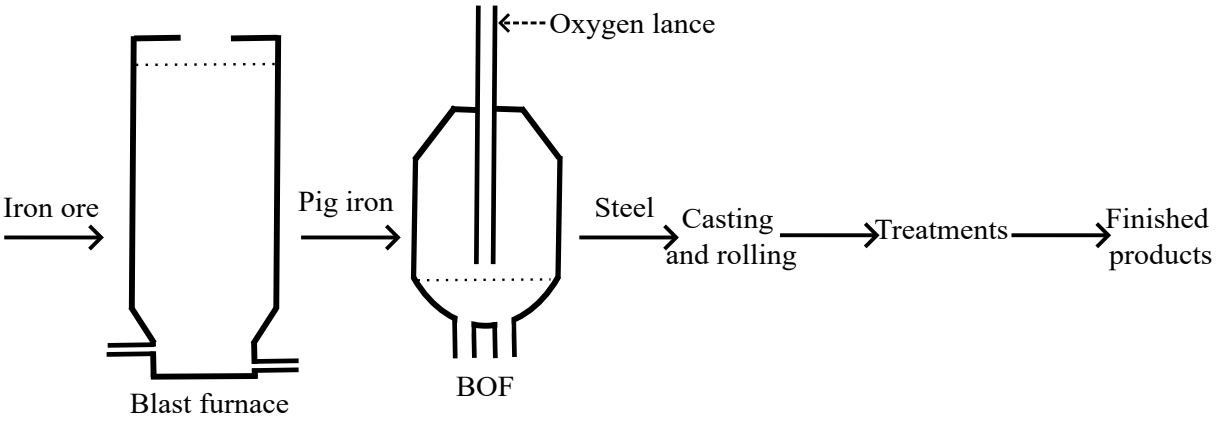

Figure 1.2: Steelmaking process: The Blast Furnace - Basic Oxygen Furnace route.

Pig iron is brittle and not easily formable due to the high level of carbon and impurities. They are therefore removed from the molten metal by oxidation in the Basic Oxygen Furnace, also known as BOF. It is illustrated in Figure 1.3. Oxygen is flown onto and into the metal bath to react with those unwanted elements. Oxides including carbon's are created. The carbon content must fall below 0.5% and the content of the other components must be under 1%. Good quality steel is then obtained. Up to 400 tonnes of liquid metal can be contained in the BOF. The process lasts for about 20 minutes and a temperature of 1900K is reached [4, 24].

Figure 1.3: Illustration of a Basic Oxygen Furnace [3].

Finally, the steel undergoes casting or rolling. Additional treatments can be applied to enhance some properties. Steel produced via this route represents about 60% of the total pro-

duction in Europe.

This route thus represents most of Europe's steel production. Moreover it is still developing in Asia, main global steel producer. Optimizing it is thus a key to improve Europe's emissions. It is also beneficial for the steel producers. In fact, greener steel is closely linked with significant savings. Less energy, less pig iron, less added fluxes to adapt equilibrium are indeed needed.

Each step of the process is associated with carbon dioxide production. Their performance should all be increased. In the current paper, the Basic Oxygen Furnace, in which the oxidation takes place, is studied. A deeper look at its operating context is thus taken.

1.3 The Basic Oxygen Furnace

The Basic Oxygen Furnace is represented in Figure 1.3. Its key dimensions are highlighted in Figure 1.4. The oxygen can be blown from the top, the bottom or both. In Europe, mostly top blowing is achieved.

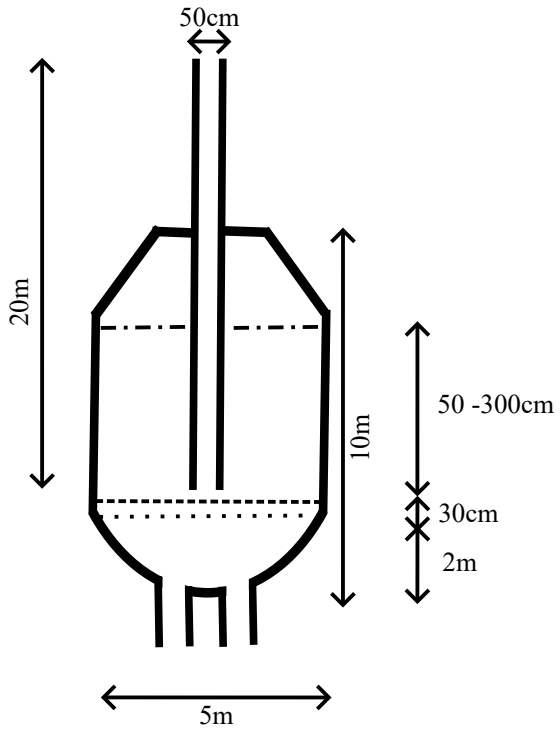

Figure 1.4: Key dimensions of the BOF and of the phases.

The main goal of the BOF is to remove the carbon content from the steel. Moreover, it aims at eliminating the impurities such as silicon and phosphorus. To remove efficiently these unwanted elements, two main parameters are controlled: the blowing and the phases. The different steps in the top-blowing configuration is represented in Figure 1.5.

Firstly, the molten metal is poured into the BOF. Oxygen then starts blowing. The lance position is high, at about 3m from the bath. At the bath level, the jet is smooth. The most oxidant component reacts: silicon. The slag is formed. It is a thin layer of metal and oxides

covering the bath, as represented in Figure 1.5. It is mainly composed of limestone. To adjust the slag composition, limestone or other fluxes can be added. This step lasts for the first quarter of the process as illustrated in Figure 1.6.

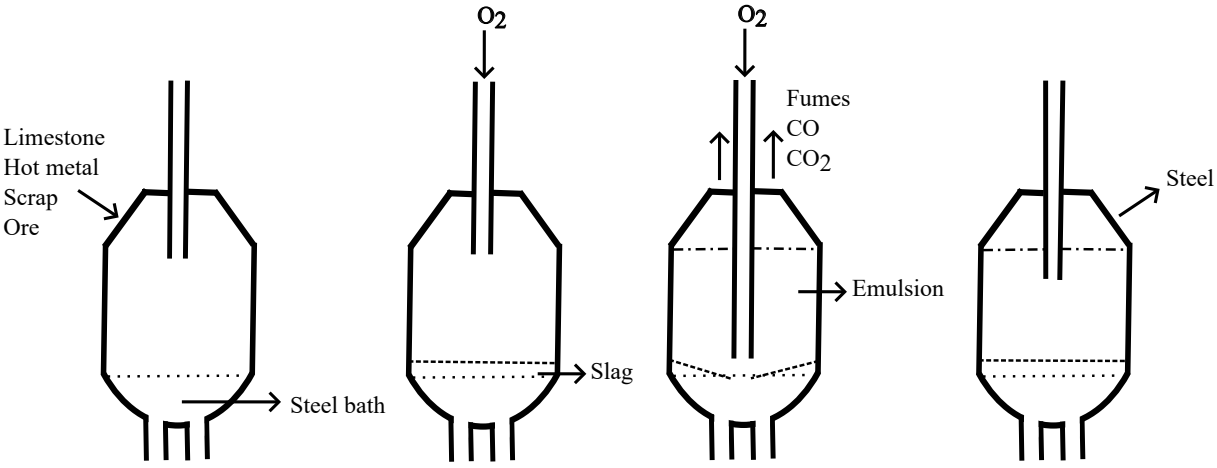

Figure 1.5: BOF process.

Afterwards, for the next half of the process duration, decarbonization occurs. The carbon content must decrease from 4% to less than 0.5%. It must fall below this value if high quality, resistant and malleable, steel is sought. To decrease the concentration of carbon, the lance is lowered to about 1.8m above the bath. Then the jet becomes more violent and the bath is stirred. Carbon monoxide is formed. To improve the sustainability of the process, it then reacts during a post-combustion reaction. This is however beyond the scope of this work. Carbon dioxide is then created and exits the BOF. Due to the violence of the blowing, an emulsion of metal and gas is produced as represented in Figure 1.5. That emulsion can cover the lance tip. Consequently the flow is impacted and the blowing changes. Finally, for the rest of the blowing, the remaining elements react and move into the slag. All the unwanted elements are therefore concentrated in the slag.

To achieve a smooth functioning, numerous parameters must thus be controlled. Reactions happen simultaneously in the bath, in the slag and in the ambiance air. Moreover, they influence each other. The composition of the phases must thus be monitored and adapted accordingly. The blowing also has a great impact on the reactions taking place. It has already been shown that the height of the lance affects the process. It is also interesting to investigate the parameters that influence the blowing itself. In fact, by developing a better understanding of the jet, the process can be improved towards a greener steel.

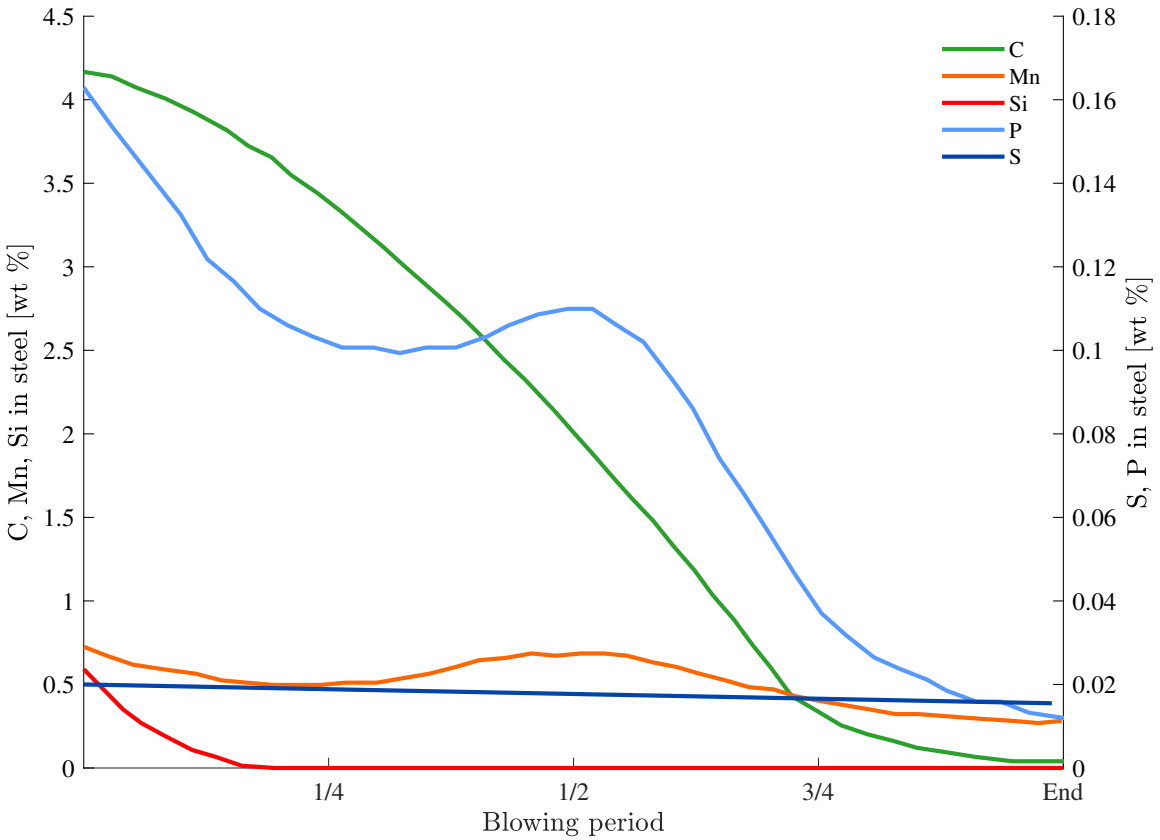

Figure 1.6: Evolution of the mass fraction of each component in the bath of steel during the blowing [4].

1.4 The oxygen lance

Oxygen is blown through a lance and exits at the lance tip. The latter is illustrated in Figure 1.7. As it can be seen, it is made of 3 to 6 nozzles inclined by 10° to 20° with respect to the axial centerline. Typically, the nozzle outlet diameter D_{out} is between $20 \cdot 10^{-3}$m and $40 \cdot 10^{-3}$m. The oxygen jets exit the nozzle at around Mach 2 [4, 24].

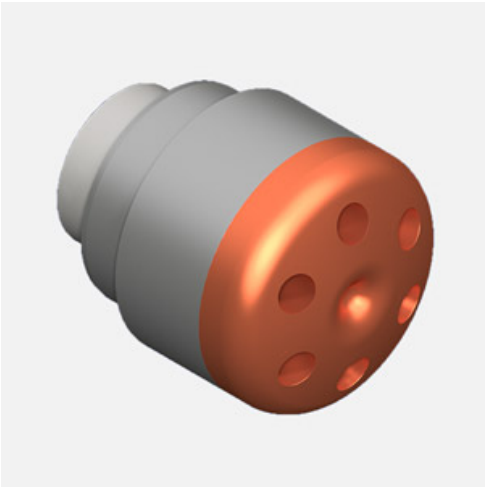

Figure 1.7: Lance tip produced at Soudobeam S.A.

1.4.1 The influence of the blowing on the oxidation process

An insight at the influence of the blowing has been presented, it is now interesting to take a deeper look at the multiple phenomena involved.

(a) Dimpling. (b) Splashing. (c) Penetrating.

Figure 1.8: The deformation modes of the bath by the gas jet [5].

Due to the blowing of the jet, a depression is created at the impacted area. The gas then travels radially, along the bath surface, outwards from the impact. Consequently the liquid metal near the surface is dragged into motion. Recirculation within the bath is then generated. Depending on the momentum of the jet and on the liquid properties, different blowing are observed [25]. Three different modes of deformation of the bath surface can be identified, depending on their depth and width. They are represented in Figure 1.8.

The smooth jet observed in dimpling mode is associated with the oxidation of silicon while the deeper penetration allows for all the carbon to react [26]. These modes of blowing are therefore determinant in the oxidation process.

Moreover, these phenomena are unstable and oscillating. Ripples move from the cavity towards the BOF walls. Slag formation is promoted. For deeper penetration, as splashing, edges surround the depression. Droplets are spit and return the bath with dragged gas bubbles [27]. Emulsion is formed [26]. The blowing thus also plays an essential role in the formation of phases.

For deep penetrating blowing, the droplets sometimes impact the lance and the converter walls. This splashed metal causes wear, which results in a loss of production [28]. However emulsion can protect the equipment from these droplets. By controlling the blowing process, the lifetime of the facilities can then be increased.

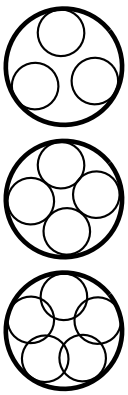

Figure 1.9: Influence of the number of nozzles on the impacted area of the bath [4].

The blowing thus impacts significantly all the phenomena occurring in the BOF. Experiments and simulations have been conducted to identify the influence of the various parameters. Firstly, the higher is the lance and the lower is the mass flow rate, the more shallow is the penetration and the smoother is the jet [29]. The magnitude and the frequency of the fluctuations are also smaller. The depth and diameter of the cavity are increased as well by increasing the BOF back-temperature and decreasing the bath density [30]. Additionally the forward splashing rate increases with the increase of the lance angle with the vertical, while the penetration depth decreases [28]. Regarding the manufacturing of the lance tip, the more the nozzles, the larger is the impacted area as represented in Figure 1.9. Consequently the rate of oxidation is higher [4]. Finally the mixing of the bath increases with the bath depth [30].

The key role that the blowing plays in the success of the BOF operation is thus highlighted. Mastering the blowing allows to control the oxidation of the unwanted elements in the bath itself, the phases generation, which chemical equilibrium also impacts the removal of the impurities, and the damage of the equipment. The height of the lance, the oxygen mass flow rate, the BOF back-pressure, the bath density, the depth of the phases, the number of nozzles, they all impact the oxidation process. Hence, the blowing is at the core of the BOF operations. Understanding its behavior is thus the key to improve the process. The main characteristics of the jet and the parameters that influence its properties at the nozzle exit are therefore developed.

1.4.2 The characterization of the supersonic jet

A schematic of the supersonic jet is illustrated in Figure 1.10. Different zones can be highlighted. The potential core lasts for about $6D_{\text{out}}$. It is characterized by constant velocity and constant pressure. The length of this zone can thus be easily identified from results. The accurate prediction of this quantity is thus a useful tool to validate models [31, 6, 29].

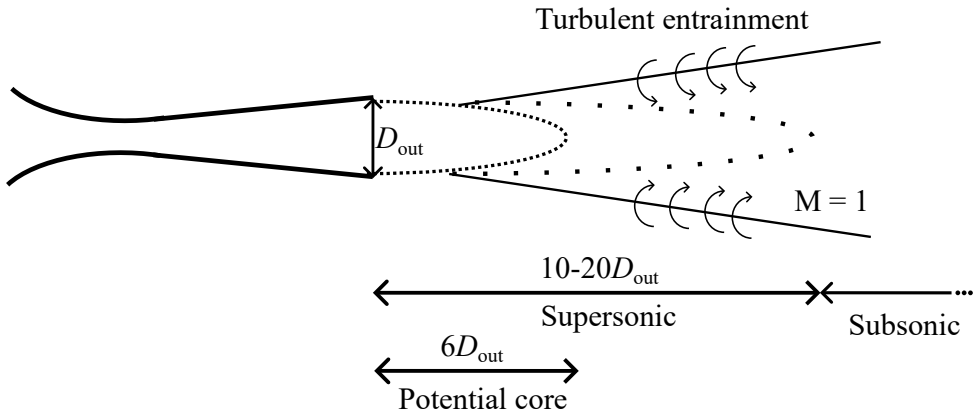

Figure 1.10: Characteristics of the supersonic jet and illustration of the different zones [6].

Afterwards, the velocity starts decreasing. Between $10D_{\text{out}}$ to $20D_{\text{out}}$, sonic point is reached. the jet then becomes subsonic. The velocity decay is caused by the turbulent entrainment, which also induced spreading of the jet. From this characterization of the jet, the influence of the lance height can be understood. In fact, the higher is the lance, the lower is the gas velocity at the bath and the larger is the spreading. Consequently, the jet is smoother [29].

In a high temperature field, the supersonic region is longer than in the case of a supersonic jet at room temperature. In fact, the lower is the ambient density, the longer is the supersonic region [16, 13]. The mass addition by entertainment is then lower and there is less dissipation [13]. As a benchmark, at 1900K, the air density is 6 times lower than at room temperature. This

ascertains the influence of the BOF temperature on the blowing [30].

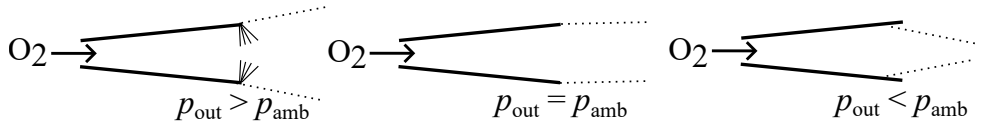

Figure 1.11: Influence of the exit pressure on the jet behavior.

The exit pressure of the nozzle also influences the behavior of the jet [32]. If the exit pressure is higher than in the ambiance, the nozzle is under-expanded, shocks appear. On the contrary, it is over-expanded. The end of the nozzle is no longer cooled down by the jet and it erodes. The nozzle characteristics are then modified. To increase the lifetime of the nozzle, this case should therefore be avoided [4]. These phenomena are represented in Figure 1.11. The case of an adapted nozzle where the pressures match is never observed in real-life applications. Consequently, the jet characteristics differ from the design and its influence on the bath changes.

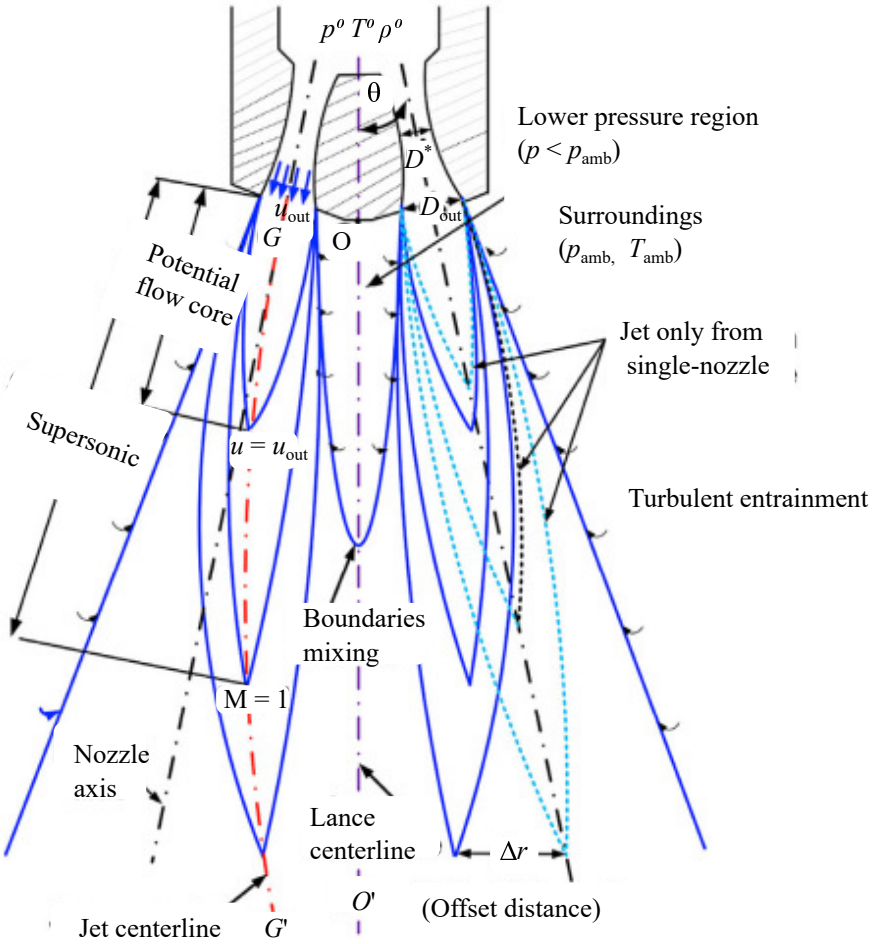

Figure 1.12: Schematic of the coalescence of the jets [7].

Additionally, as the lance tip is composed of 3 to 6 nozzles, the supersonic jets interact with each other. Subsequently this coalescence of the jets influences the blowing. The phenomena is

represented in Figure 1.12. It can be seen that the jets tend to deviate from the nozzle axis and form one single bigger jet. Above about a 11° angle, there is no longer interaction between the jets [7, 30]. Moreover, the more inclined are the nozzles, the more agitated and stirred is the bath [28].

Mastering the blowing technique thus involves improving the lance tip design. Optimizing the manufacturing of the latter is thus an element to work on.

1.4.3 The manufacturing of the tip

As represented in Figure 1.13, the nozzle design is complex. The oxygen jet must indeed be cooled down from the ambiance. There are numerous ways to build such a lance tip. Depending on the manufacturing, the properties of the jets will differ. Optimizing the nozzles is therefore tricky. Once the model is developed and guidelines are drawn, the adaptation of the tip design must not be underestimated. It it thus important to master the different techniques available. Luckily, the tools used at Soudobeam S.A. were observed during the internship.

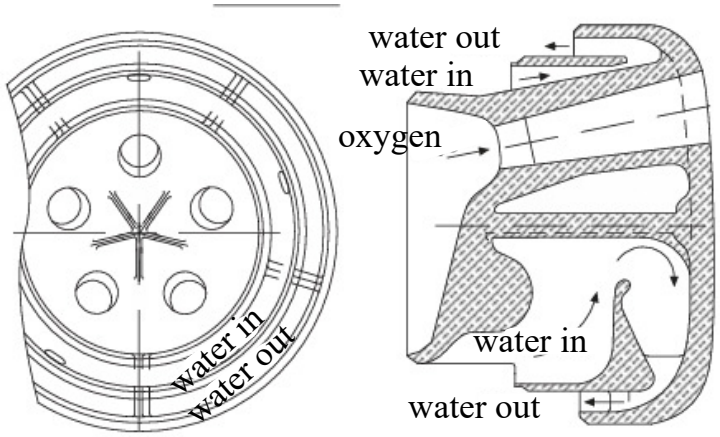

Figure 1.13: Schematic of typical lance tip [4].

Through the investigation of the steelmaking process, it is demonstrated that improving the oxidation in the Basic Oxygen Furnace is a possible path to make steel greener. Particularly it is highlighted that the blowing of oxygen jets determines the smooth functioning of the operation. It indeed influences all the phenomena occurring in the furnace. Understanding and controlling the jets is therefore the key to improve the BOF performance and increase sustainability.

To develop such an expertise, experiments can be carried out or models can be built. As a special attention is paid to this topic, numerous research have already been conducted. However, all of the simulations have been run on licensed software. The latter offer little freedom to the user to customize and adapt the solver to its own needs. The aim of the paper is therefore to develop an accurate model with open source tools.

Thanks to this model, the characteristics of the flow are extracted. Consequently the information is interpolated to determine the impact on the bath and the oxidation process. Also the features at the nozzle exit are useful to predict damage of the lance.

To build and validate such model, comparison tools must be selected. The available results should therefore be investigated to form a reference portfolio.

2 Supersonic jet modeling - The state-of-the-art

With the aim of improving the BOF process and consequently meet the demand of greener steel, predicting the behavior of supersonic jets in free atmosphere has become a key concern. In fact, knowing its characteristics at the bath, its penetration can be approximated. Successively the rate of oxidation of the components can be inferred. The process can be optimized. Additionally the properties at the nozzle outlet are valuable to estimate the damage of the lance. Accordingly the influence of the nozzle deterioration on the flow can be studied. With the jets velocity, density and spreading, the behavior can be reconstructed. Therefore developing such model is attractive.

As mentioned in Section 1, numerous phenomena are observed during the oxidation process. Among others, the formation and the reactions in the slag, the production of emulsion, the mixing of the bath, the post-combustion reactions, the temperature and the pressure variations take place in the BOF. However all of these phenomena cannot be taken into account in the model. Assumptions must thus be stated.

In this study, the first validation step of the open source tools is pursued. Thus a significantly simplified model is considered. A single-phase adapted flow through a nozzle exiting in quiescent air is assumed. This hypothesis differs from the BOF environment on multiple levels. An adapted flow is indeed never observed in reality. Moreover the ambiance and the jet do not have the same composition. These assumptions are further described here after.

The validity of these hypotheses must be verified. Reference results are thus sought in the literature to build comparison tools. The reliability of the predictions can then be validated. The gathered knowledge falls into three categories: experimental, analytical and numerical. For each group, cold and hot atmospheres are separately studied. The cold case is introduced to observe the main characteristics of the supersonic free shear flow. With the second configuration, the effects of a high temperature field on the flow are highlighted. This provides a closer insight into the BOF operating context.

2.1 Experimental results

Two experiments are selected as a reference to build the model. The first one is carried out by Eggers [8]. It considers a single supersonic jet in cold atmosphere. The second reference examines a single supersonic jet in a high temperature field. It is carried out by Alam [13].

2.1.1 Single supersonic jet in cold atmosphere - Eggers' experiments

Seeking to validate formulations for the eddy viscosity function, Eggers studied a Mach 2.22 jet from a circular axisymmetric nozzle exiting in quiescent air [8]. The first aim of the paper is not relevant to this study. However, the extracted results are useful to validate a model. The evolution of the centerline axial velocity and the axial velocity profiles at multiple axial distances are provided. Hence it is a useful comparison tool.

Moreover the experimental conditions display similarities with the oxygen lance operation. The jet exits in quiescent air. The design Mach number of 2.2 is in the range of the lance's. Also the ambiance is at atmospheric pressure. Finally the nozzle exit diameter is equal to $25.58 \cdot 10^{-3}$m, which is in the range a common lance nozzle. Since the results are non-dimensionalized, this should nevertheless not be relevant. A limited similarity to the lance jet is thus reproduced.

However some parameters differ. The ambiance is here at room temperature whereas it reaches 1900K during the BOF process. As mentioned, the current case is thus studied to validate the tool for a simple supersonic jet. Additionally, the experiments are conducted with ambient air. Nevertheless, in the BOF, a nearly pure oxygen jet is blown into a complex environment composed of different species. Also, the nozzle is adapted and the total inlet temperature of the nozzle is equal to the ambient temperature. While it is the desired operating context, this cannot be reached due to the numerous complex phenomena. These deviations are expected to impact the mixing and the spreading of the jet.

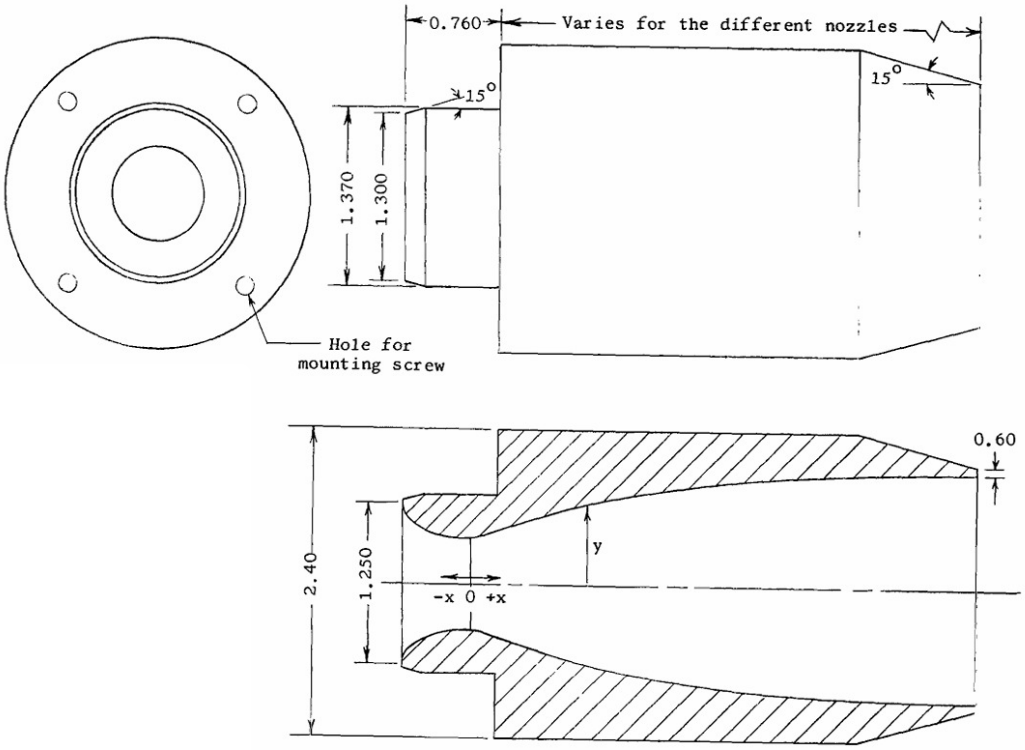

Figure 2.1: Eggers' experiments: Illustration of the nozzle [8]. The dimensions are in inches.

The inflow conditions of the experiments are listed in Table 2.1 and in Table 2.2. The nozzle geometry is precisely described in Reference [33] and is illustrated in Figure 2.1.

Table 2.1: Eggers' experiments: Ambiance conditions [8].

M	p	T
-	Pa	K
0	101352	291.67

Table 2.2: Eggers' experiments: Nozzle inflow conditions [8].

M_{out}	p^0	T^0
-	Pa	K
2.2	1118330	291.67

2.1.2 Single supersonic jet in hot atmosphere - Sumi's experiments

To improve the understanding of the BOF operation, Sumi carried out experiments with multiple ambiance temperatures [16]. The centerline velocity and temperature of the jet are measured. An experiment with a SCOPE-JET for the Electric Arc Furnace is also carried out but it is not relevant to this study. Because the paper aims at estimating the impact of the temperature in the BOF, it is highly valuable in the modeling process and complements Eggers' experiments.

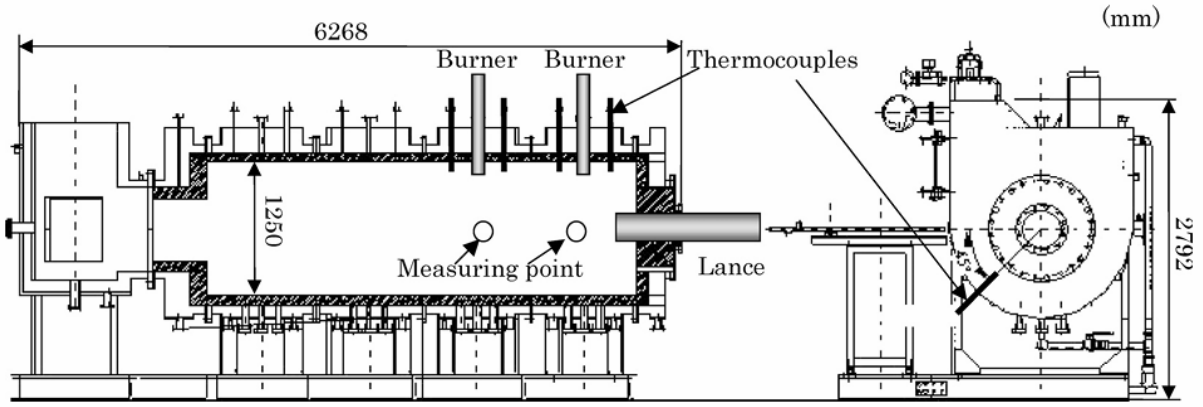

Figure 2.2: Sumi's experiments: The set-up of the experimental apparatus.

The set-up of the experimental apparatus is represented in Figure 2.2. The highest temperature reached by the burners is 1002K, which is still lower than the BOF's operating values. Its environment is thus not yet accurately modeled. Nevertheless, it provides an insight into the influence of the temperature on the jet. Moreover, the nozzle exit diameter is equal to $9.2 \cdot 10^{-3}$m. This is more than 2 times smaller than the lower limit of the common range for oxygen lance nozzles. Because of the non-dimensionalization of the results, this should have a limited impact. Also the nozzle design Mach number is slightly lower than the one for nozzles in oxygen blowing. Additionally, similarly to the cold case, the total inlet temperature of the nozzle is equal to the ambiance temperature and the nozzle is adapted, which is not achievable in real-life applications.

Here, as listed in Table 2.3, the ambiance composition varies with temperature. At the highest temperature field, the composition is closer to the BOF's. The reproduction is thus more accurate than for the cold configuration. However, as for the cold case, both the jet and the ambiance still have the same composition, contrary to the BOF operation. Similarly to the cold case and to the BOF, the ambiance is at atmospheric pressure.

The nozzle coordinates are not provided in the paper. They have however been reconstructed. They are listed in Appendix A. The ambiance and nozzle inflow conditions are listed in Table 2.3 and Table 2.4. The ambiance composition varies depending on the temperature.

.

Table 2.3: Sumi's experiments: Ambiance conditions [16].

T	M	O_2	N_2	CO_2
K	-	%	%	%
285	0	54	46	0
772	0	85	9	6
1002	0	88	3	9

Table 2.4: Sumi's experiments: Nozzle inflow conditions [16].

M_{out}	T^0
-	K
1.72	285

The pressures are not given. However, the nozzle is adapted. The pressure ratio can thus be expressed as a function of the nozzle outlet Mach number M_{out},

$$M_{out}^2 = \frac{2}{\gamma - 1}\left(\left(\frac{p_{in}^0}{p_{out}}\right)^{\frac{\gamma-1}{\gamma}} - 1\right), \tag{2.1}$$

where p_{in} is the pressure at the nozzle inlet, p_{out} is the pressure at the nozzle outlet, and γ is the ratio of the heat capacities.

2.2 Analytical results

From both of these experiments, analytical correlations have been derived. Based on the Eggers' experiments, the correlation of Witze is constructed [9]. The correlation of Ito and Muchi is built with Sumi's experiments [10].

2.2.1 Single supersonic jet in cold atmosphere - The correlation of Witze

The correlation of Witze is based on experimental results of hot and cold subsonic jets as well as cold supersonic jets, which includes the results from Eggers [9, 8]. The correlation describes the axial centerline velocity as a function of the axial distance from the nozzle exit. The parameters are the Mach number M_{out}, the static temperature T_{out}, the density ρ_{out} of the jet at the nozzle exit, and on the ambiance density ρ_{amb}.

$$\overline{u}_c(x/r_{out}) = 1 - \exp\left(\frac{-1}{\kappa(x/r_{out})(\overline{\rho}_{out})^{0.5} - X_c}\right). \tag{2.2}$$

The correlation is expressed in Eq. (2.2) where $\overline{u}_c$ is the dimensionless centerline axial velocity equal to U_c/U_{out}, κ is a proportionality constant which depends on whether the jet is supersonic or subsonic, x is the axial coordinate, non-dimensionalized by the nozzle exit radius r_{out}, $\overline{\rho}_{out}$ is equal to ρ_{amb}/ρ_{out}, and X_c, equal to 0.70 as found by Kleinstein [34], is the dimensionless correlation parameter core length.

Thus, in this case of a supersonic jet, the axial velocity is first described as constant in the potential core. Its length is computed as

$$\left(\frac{x}{r_{\text{out}}}\right)_{\text{core}} = \frac{X_c}{\kappa_{\text{super}}(\overline{\rho}_{\text{out}})^{0.5}}, \tag{2.3}$$

where

$$\kappa_{\text{super}} = 0.063(\text{M}_{\text{out}}^2 - 1)^{-0.15}, \tag{2.4}$$

is the expression of the proportionality constant for a supersonic jet. This value is used to compute the axial velocity until the sonic point. Then, in the subsonic region, the constant is evaluated as

$$\kappa_{\text{sub}} = 0.08(1 - 0.16\text{M}_{\text{out}})(\overline{\rho}_{\text{out}})^{-0.22}, \tag{2.5}$$

where M_{out} is equal to 1. Regarding the jet density ratio, it has been shown that it is a good approximation to assume it equal to the one of the supersonic region [9]. Additionally, the axial position must be adapted according to

$$\left(\frac{x}{r_{\text{out}}}\right)' = \left(\frac{x}{r_{\text{out}}}\right) - \left(\frac{x}{r_{\text{out}}}\right)_{\text{M}=1}\left(1 - \frac{\kappa_{\text{super}}}{\kappa_{\text{sub}}}\right). \tag{2.6}$$

A typical estimation of the dimensionless axial centerline velocity provided by the correlation is plotted in Figure 2.3.

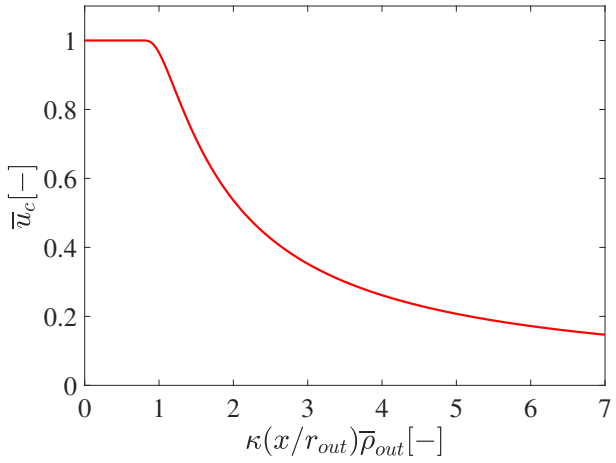

Figure 2.3: Typical estimation of dimensionless the axial centerline velocity with the correlation of Witze [9].

2.2.2 Single supersonic jet in hot atmosphere - The correlation of Ito and Muchi

The correlation of Ito and Muchi has been developed to predict the axial centerline velocity of a cold jet in hot atmosphere [10]. This tool is based, among others, on Sumi's experiments [16]. It expresses the evolution of the axial centerline velocity as

$$\overline{u}_{\text{c}}(\overline{x}) = 1 - \exp\left(\frac{-1}{2(\alpha\overline{x}\sqrt{\overline{\rho}_{\text{out}}} - \beta)}\right), \tag{2.7}$$

where α and β are dimensionless constants which values are determined experimentally. They are respectively equal to 0.0841 and 0.6035. Both the dimensionless axial centerline velocity $\overline{u}_{\text{c}}$, and the dimensionless density $\overline{\rho}_{\text{out}}$ are defined similarly as in the correlation of Witze [9]. However, the dimensionless axial distance $\overline{x}$ corresponds to the axial distance x non-dimensionalized by

the nozzle exit diameter D_{out}. This convention is used in the paper.
The dimensionless potential core length is then computed as

$$\overline{x}_{\text{core}} = \frac{\beta}{\alpha\sqrt{\overline{\rho}_{\text{out}}}}. \tag{2.8}$$

An example of the estimation of the dimensionless axial centerline velocity computed with the correlation of Ito and Muchi is illustrated in Figure 2.4.

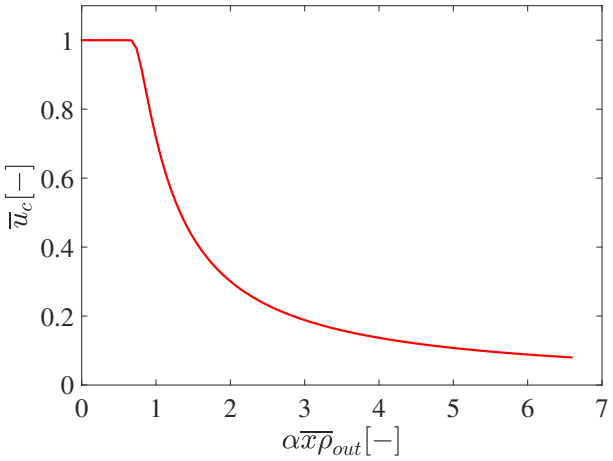

Figure 2.4: Typical estimation of the dimensionless axial centerline velocity with the correlation of Ito and Muchi [10].

2.3 Numerical results

Both the experimental results obtained by Eggers and Sumi are reproduced numerically. They are respectively conducted by Slater at NASA and Alam [11, 13].

2.3.1 Single supersonic jet in cold atmosphere - Slater's simulations at NASA

The experiments conducted by Eggers were simulated numerically by John W. Slater at NASA on Wind-US [11]. The simulation is run on a structured mesh. The set of boundary conditions are represented in Figure 2.5. The initial conditions are not uniform. The geometry is separated into two regions: the nozzle and the ambiance. Thus, the fields inside the nozzle are initialized with the value of the inflow conditions while the rest of the domain is set to the ambient freestream conditions. The case in run with Spalart-Allmaras turbulence model.

A freestream of Mach 0.05 is set in the ambiance. Quiescent air is indeed not numerically stable. Moreover, it has been shown by the NASA that considering an ambiance with low Mach number does not significantly influence the flow [12]. The results of the study carried out by the NASA on the effects of the freestream on the axial centerline velocity are illustrated in Figure 2.6. A subsonic Mach 0.5 cold jet is simulated in cold atmosphere. Thus, assuming a freestream in the ambiance avoids numerical instabilities while conserving the key characteristics of the flow.

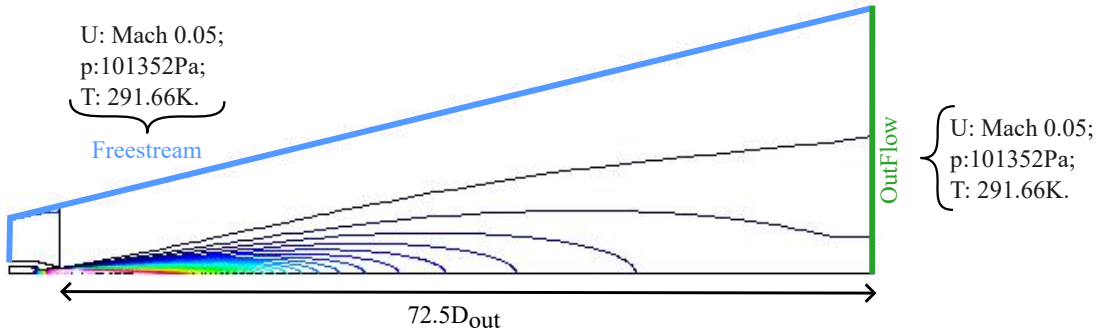

(a) Overall domain.

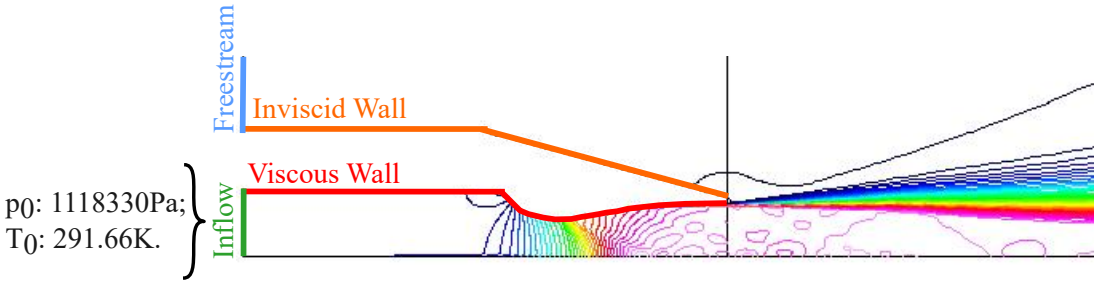

(b) Zoom on the nozzle.

Figure 2.5: Slater's simulation: Geometry and boundary conditions [11].

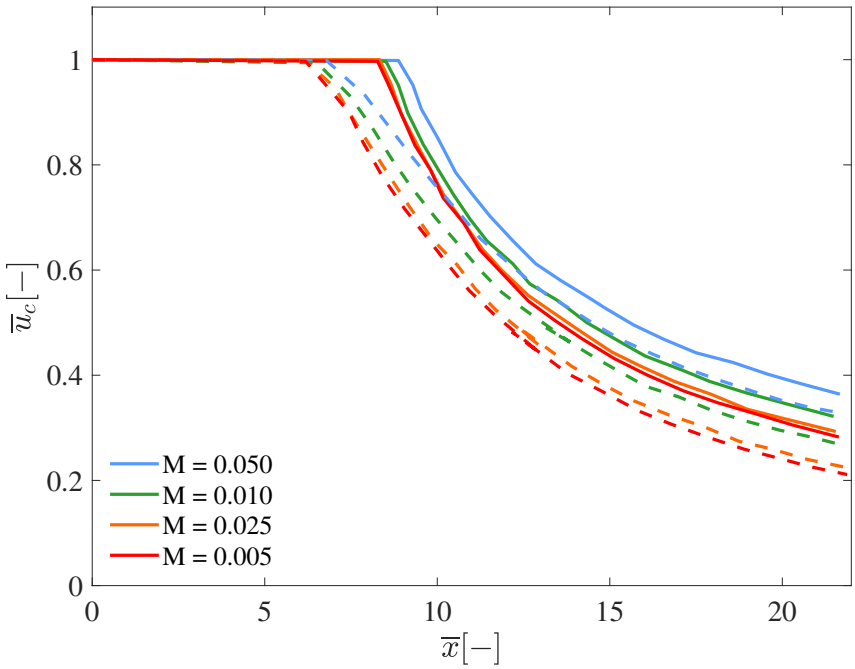

Figure 2.6: Influence of the freestream Mach number on the centerline axial velocity of a Mach 0.5 jet for both $k-\omega$ SST (in solid line) and Spalart-Almaras (in dashed line) turbulence models [12].

2.3.2 Single supersonic jet in hot atmosphere - Alam's simulations

Regarding the supersonic jet in a hot temperature field, Alam reproduced the experimental results obtained by Sumi on the CFD software AVL FIRE 2008.2 [13]. The boundary conditions are represented in Figure 2.7. As it can be seen, the nozzle is not simulated. Instead, the theoretical outlet quantities of the nozzle are set at its exit. Also, in this case, the quiescent air boundary condition in the ambiance is respected.

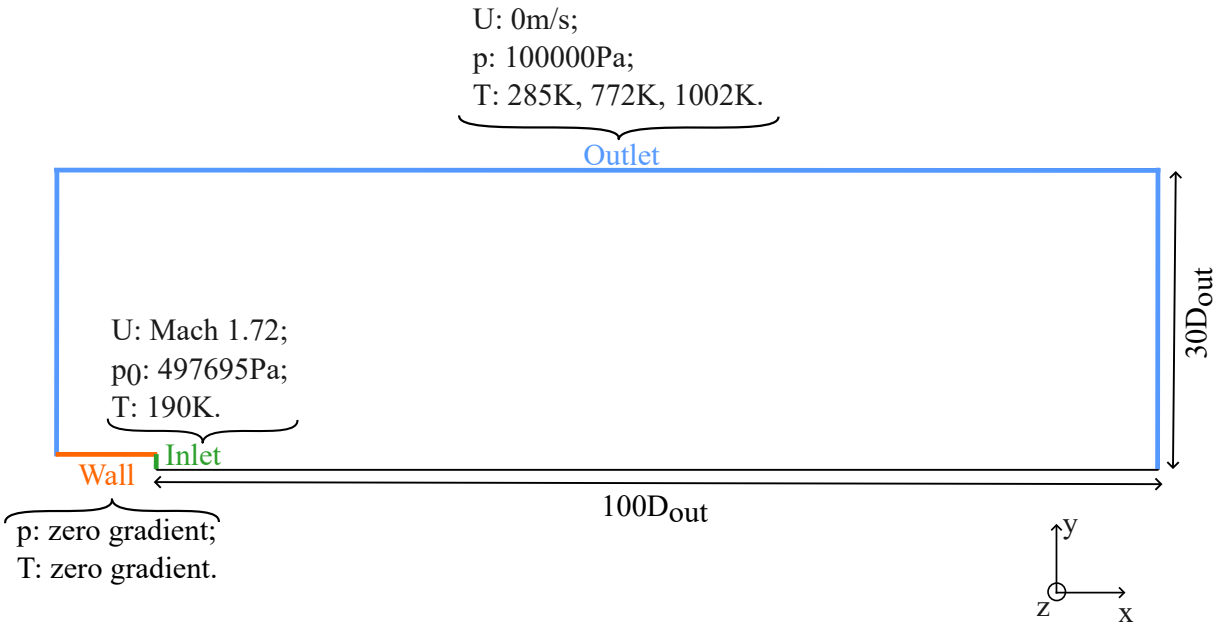

Figure 2.7: Alam's simulations: Boundary conditions and geometry for a single supersonic jet [13].

The $k-\varepsilon$ turbulence model for compressible flows is modified. In fact, it has been shown that the potential length is under-predicted by the model at high temperatures. Due to the lower density, the mass addition to the jet is reduced. Consequently, the growth rate of the turbulent mixing layer is decreased. The model is thus modified according to an adapted version of the temperature corrected turbulence model developed by Abdol-Hamid [35].

The mesh is also structured in this case. It has indeed been shown by the NASA that, for a hot jet at Mach 2.0, the simulations run on an unstructured mesh underestimate the potential length of the flow [12]. The results are illustrated in Figure 2.8. Also, the $k-\omega$ SST model is plotted against the $k-\varepsilon$ model. No major difference between the results can be observed. Therefore, both models are suitable to initiate the modeling.

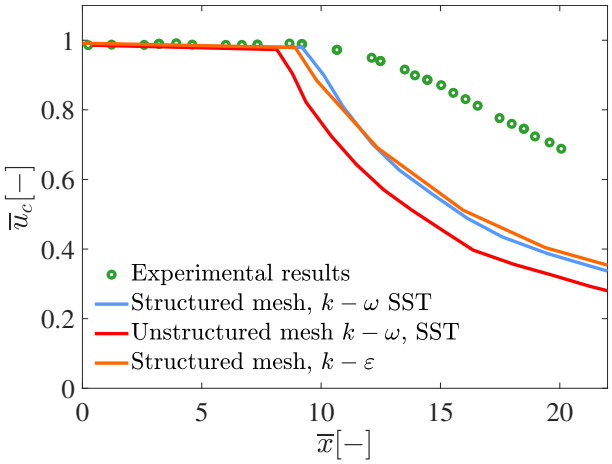

Figure 2.8: Comparison of the evolution of the dimensionless centerline axial velocity of a Mach 2.0 nozzle obtained with experiments, and numerical simulations run on structured and unstructured meshes with a $k-\omega$ SST model and on a structured mesh with a $k-\varepsilon$ model [12].

In conclusion, through this investigation of the literature, two experiments are selected as reference tools. The experiments carried out by Eggers [8] consider a supersonic jet in cold atmosphere. The influence of the temperature field in the ambiance is studied by Sumi [16]. For each set of experiments, the similarities and the differences with the BOF operating context are highlighted. Their impact on the flow is discussed in the following modeling process.

These experiments are the primary comparison tools selected to validate the modeling. They are complemented by analytical and numerical results. The correlation of Witze and the simulations of Slager at NASA [9, 11] are implemented based on the cold case. For the hot configuration, the references are developed by Ito and Muchi, and Alam [10, 13].

A set of comparison tools is thus established. With this portfolio, the modeling of the supersonic jet with open source tools can be validated. The demand of developing a greater understanding of the BOF process with free software can then be met. In the following, the cold atmosphere is first studied. Since no significant temperature fluctuations then occur in the flow, it is easier to build the model. Afterwards, the high temperature field is introduced. Its influence on the flow is investigated.

3 Supersonic jet in cold atmosphere

It has been highlighted that one path to tend towards greener steel is to improve the blowing in the BOF. Developing a model to determine the characteristics and the influence of the jet is therefore a key aspect to achieve this goal. Subsequently a portfolio of references is established to validate such model. The latter must now be constructed and validated.

The major difference with previous studies is that the model is build with open source tools. The meshing tool Gmsh and the CFD software OpenFOAM® are selected [1, 36]. The development of models is therefore more complex than with licensed software but offers more freedom.

Therefore, firstly, the supersonic jet in cold atmosphere which corresponds to the experiments of Eggers are modeled [8]. Hence the high temperature field in the ambiance is not yet considered. The simulation is thus simpler.

To build the model, the geometry of the domain and the mesh are constructed. Afterwards, the case set-up in OpenFOAM® is presented. An insight into the convergence strategy is shared. Afterwards the model is validated. The influence of the assumptions and modeling choices are verified. Finally the results are presented. Links with the BOF operation are highlighted.

3.1 Mesh generation

The geometry of the domain is firstly defined. It is generated within the meshing tool Gmsh [1]. Similarly to the reference simulations, the geometry is parameterized depending on the nozzle inlet and outlet diameters. The key dimensions are represented in Figure 3.1. The nozzle coordinates are given in Reference [33].

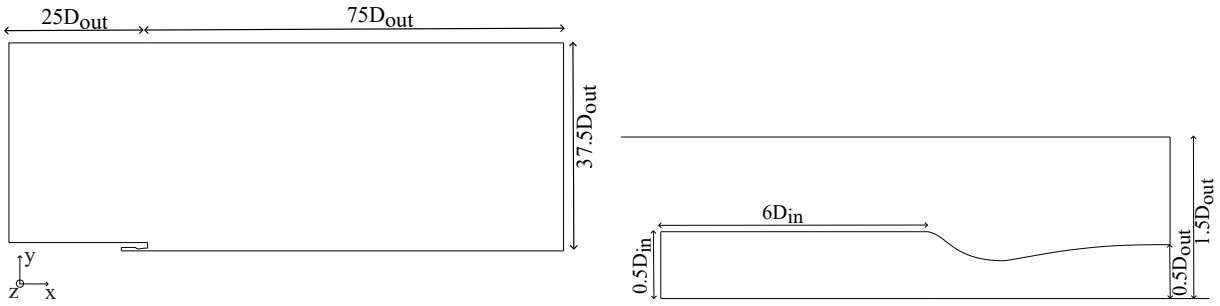

(a) Overall domain. (b) Zoom on the nozzle.

Figure 3.1: Supersonic jet in cold atmosphere: Parameterization of the geometry.

In Section 1, it is highlighted that the supersonic jet reaches the subsonic region within $10D_{\text{out}}$ to $20D_{\text{out}}$. In the domain, all the zones of the jet are therefore captured. Moreover the characteristics at the bath level are sought. The lance height varies between 1.8m and 3m. Since the nozzle diameter ranges between $20 \cdot 10^{-3}$m and $40 \cdot 10^{-3}$m. If the larger nozzle is taken as a reference, this corresponds to a maximum distance of $75D_{\text{out}}$. The wanted quantities can therefore be extracted at the boundaries of the domain. Regarding the radial dimensions, the BOF radius is about 2.5m. This is equivalent to $62.5D_{\text{out}}$. The domain is in this case smaller. Consequently, the presence of walls would have a bigger impact on the flow. The boundaries

conditions are subsequently adapted.

Two types of meshes can be built: structured and unstructured. Structured meshes are differentiated from unstructured's by the regular shapes of the elements. Consequently the generation of structured meshes is difficult for complex geometries. They however offer better convergence. As highlighted in Figure 2.8, for this model, structured meshes provide better results. With the aim of validating the tools, the case will be run on both types of meshes.

The finer is the mesh, the more precise is the model. However, this also comes with the need of a smaller time step and an increased computational cost. The mesh should therefore be refined strategically. Along the walls, the mesh must be refined to capture accurately the boundary layer. Also, in the shear layer, where the flow from the nozzle and the ambiance mix, elements must be fine enough to capture the phenomena. In the ambiance, the mesh can be coarsened. The generation of unstructured and structured meshes meeting these requirements is presented.

To avoid any incompatibilities, the mesh format exported from Gmsh is *Gmsh mesh Version 2 ASCII*. Also, all the meshes pass the *checkMesh* utility in OpenFOAM®. Their quality is thus ensured [20].

3.1.1 Unstructured mesh

The Frontal-Delaunay algorithm is used in Gmsh to generate a 2D unstructured mesh. This algorithm indeed creates high quality elements [37]. To create the associated 3D extruded mesh required by OpenFOAM®, the Delaunay algorithm, which is very robust, is applied. The triangles are then recombined into quadrangles with the Blossom algorithm. Those are the default algorithms in Gmsh.

The size of the elements are computed as the minimum of the prescribed sizes. Thus, at each point of the domain, the size of the elements at this location is given. Also the size of the elements in the surrounding of a line can be imposed. Additionally a boundary layer is constructed along the reservoir, the nozzle and the lance wall. The constraints and the resulting mesh are represented in Figure 3.2. As OpenFOAM® does not accept meshes with single nodes along the axis of symmetry i.e., a quadrangle with only one corner on the symmetry axis, a structured surface is created along the axis. The mesh contains 99913 elements.

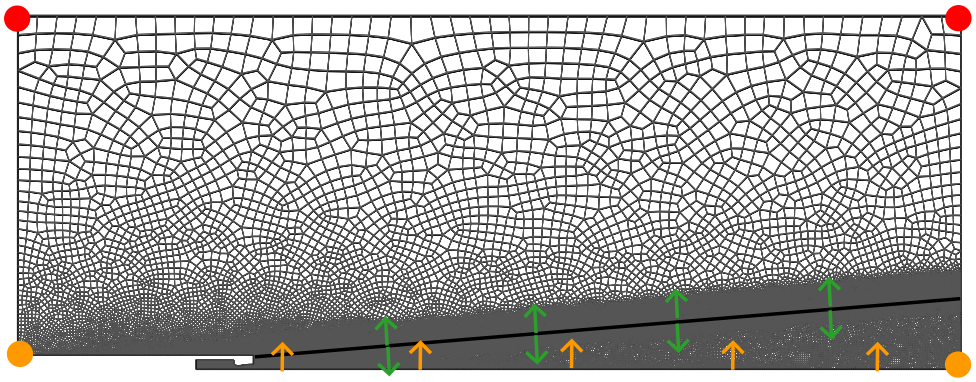

(a) Overall domain.

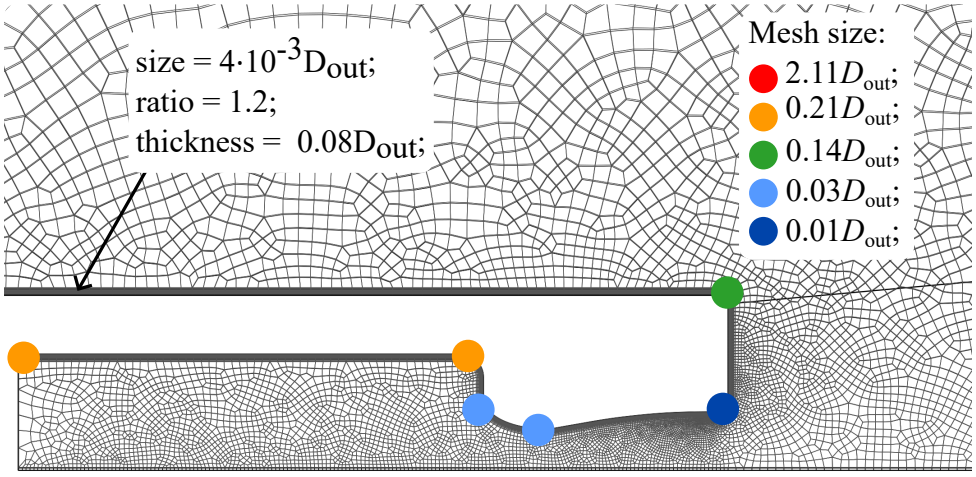

(b) Zoom on the nozzle.

Figure 3.2: Supersonic jet in cold atmosphere: Unstructured mesh.

3.1.2 Structured mesh

The structured mesh is built with the transfinite tool. To refine the mesh in the nozzle and in the shear layer, the domain is subdivided into different zones illustrated in Figure 3.3. Each transfinite volume can only be made up of five or six transfinite surfaces, while one transfinite surface can be defined by multiple curves as long as they form a closed loop. Eight transfinite volumes are therefore created.

For each curve, the number of nodes must be imposed. Additionally, a geometric progression or a refinement at both ends of the curve can be set. The set of constraints for each curve is represented in Figure 3.3. The mesh is thus refined at the walls, at the nozzle exit and in the shear layer. The resulting mesh contains 128685 elements.

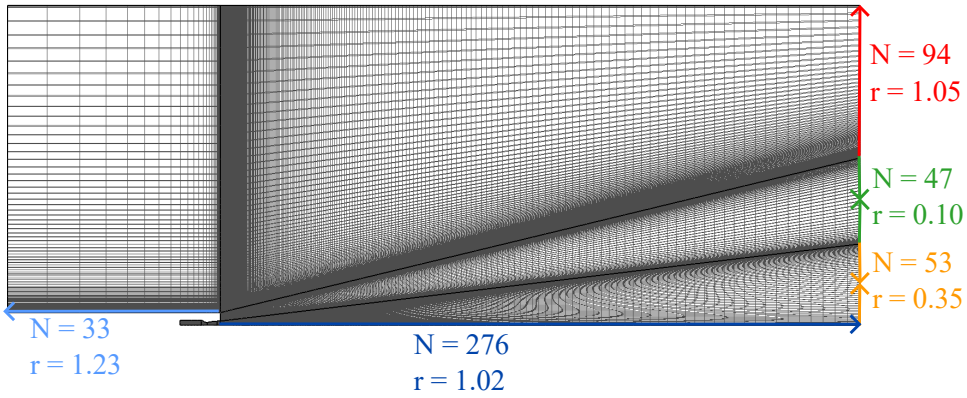

(a) Overall domain.

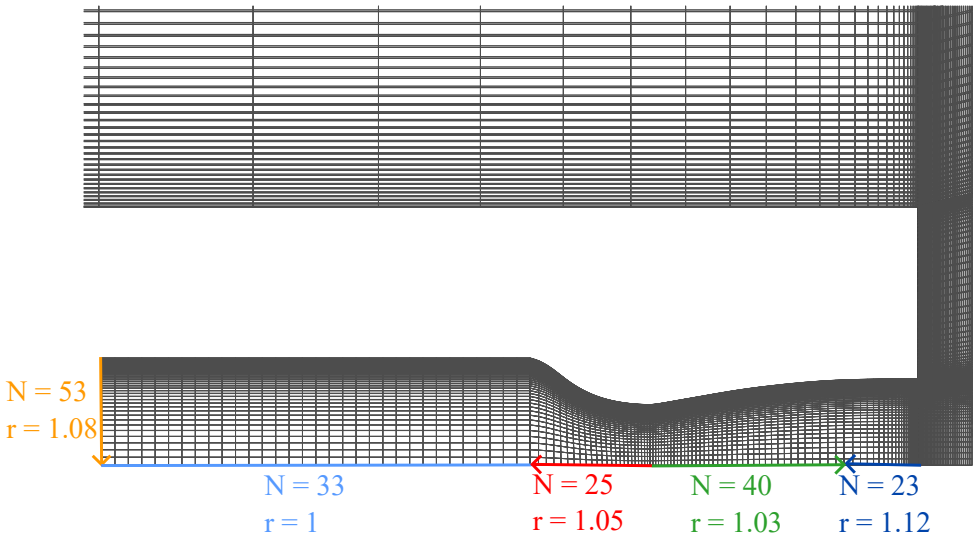

(b) Zoom on the nozzle.

Figure 3.3: Supersonic jet in cold atmosphere: Structured mesh.

3.2 Case set-up in OpenFOAM®

After building the mesh, the different options of an OpenFOAM® case must be defined. These include the boundary conditions, the initial conditions, the thermophysical properties, the turbulence model, the solver, the numerical schemes, and the algorithms. The choices are motivated in the light of the BOF operation, and of the reference experiments and simulations.

3.2.1 Boundary conditions

The boundary conditions illustrated in Figure 3.4 match the experimental conditions of Eggers presented in Section 2.1. The initial fields are represented in Figure 3.4 as well. They are also in accordance with the reference numerical simulation conducted by the NASA introduced in Section 2.3. A few differences should however be highlighted.

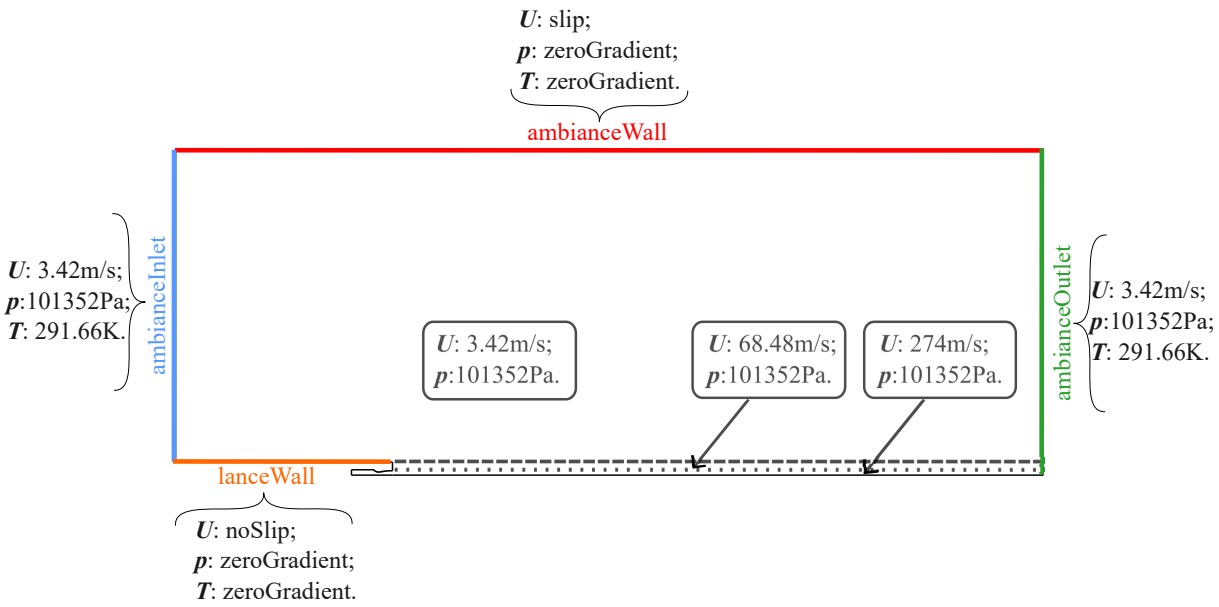

(a) Overall domain.

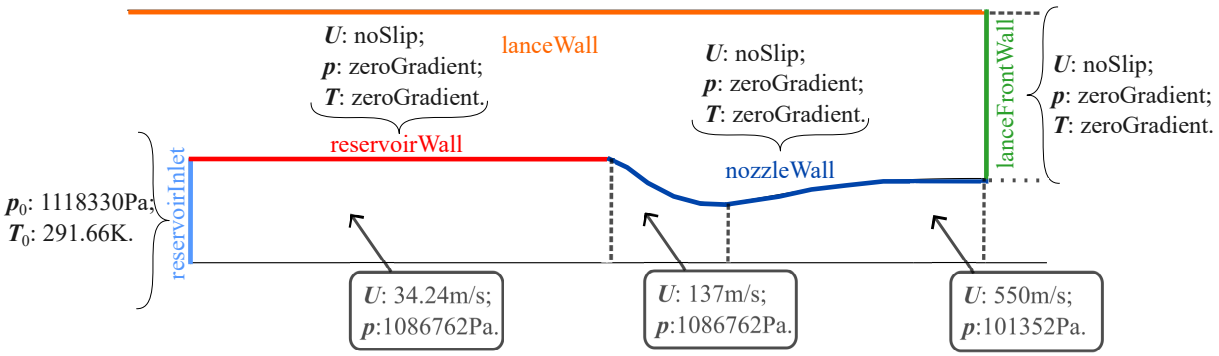

(b) Zoom on the nozzle.

Figure 3.4: Supersonic jet in cold atmosphere: Boundary conditions, in color, and initial conditions, in gray.

First, a freestream of Mach 0.01 is imposed in the ambiance. As it has been shown in Figure 2.6, the influence of such freestream on the results is small, and it will avoid any numerical instability. Secondly, the *ambianceWall* is, in this case, an inviscid wall rather than a freeastream as in the reference simulation [11]. This choice of boundary condition provides a closer reproduction of the BOF environment while limiting the impact of the closer wall. The influence of those two boundary conditions is studied in Section 3.3. The other walls of the domain are viscous.

With respect to the BOF environment, the nozzle outlet Mach number is therefore similar as well as the pressures. The temperature of the ambiance is not accurately reproduced. Consequently, the spreading and the velocity decay are larger, as mentioned in Section 1. Also the bath is not modeled. The change of direction of the jet and its influence on the nozzle and the ambiance flow cannot be predicted. Finally, the effects of gravity are disregarded.

The freestream boundary condition is used at the *ambianceInlet*. The inflow is therefore fixed. In the case of outflow, a zero gradient is prescribed. At the *ambianceOutlet*, as recommended for supersonic flows, a *waveTransmissive* boundary condition is selected [20]. As its name

indicates, this boundary does not reflect the waves that may appear during the simulation of supersonic jets. Numerical instabilities are therefore avoided. The initial values are defined as well as the far field. The latter corresponds to the values towards which the flow should tend at the outlet. The flow is therefore not prescribed but its tendency is.

At the *reservoirInlet*, the velocity is inferred from the total pressure. This indeed corresponds to the BOF operation. Oxygen is kept static in a pressurized tank. The pressure difference between the reservoir and the ambiance induces the flow.

For the viscous walls, the turbulent wall function for each turbulent field is used. These wall functions should be used with y^+ ranging between 20 and 100, i.e. in the log region [38]. The first cell of the mesh then does not fall into the viscous sub-layer. The latter corresponds to $y^+ < 5$ in Figure 3.5. The boundary layer can be accurately estimated by blending of the calculations for each region.

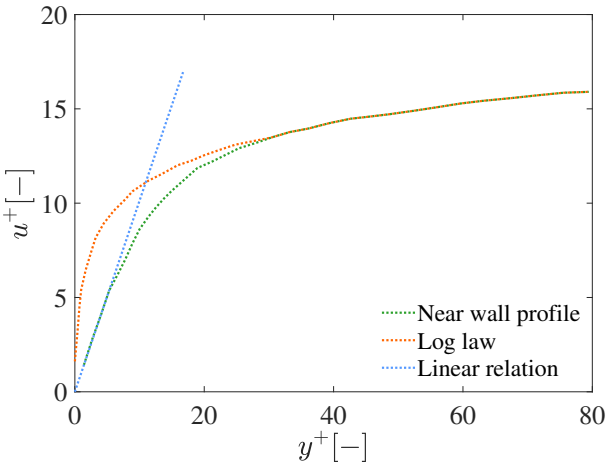

Figure 3.5: Supersonic jet in cold atmosphere: Near wall profile of the mean velocity [31].

To set the initial conditions, six zones are defined within the domain. Non-uniform initial conditions can consequently be set. The zones have been defined to be physical, according to the converged flow. Uniform initial fields indeed could not reach convergence. The definition of the zones with a relatively smooth variation of the fields value thus plays a role in the convergence strategy.

3.2.2 Thermophysical properties

Besides the boundary conditions of the flow, the properties of the fluid in the model must be defined. The experiments are conducted with air [8]. A pure mixture with air properties is thus considered. However, in the BOF, pure oxygen is flown into an atmosphere composed of multiple species. The densities of the fluids are consequently not accurately modeled. This impacts the spreading and the velocity decay of the jet. The possible reactions between both flows are also disregarded. The BOF operating conditions are thus not closely reproduced. However the experimental conditions of Eggers are respected. The validation process can smoothly be conducted, which is currently the main objective.

Regarding the other properties, the specific heat is constant. The enthalpy and the entropy are evaluated consequently. The general thermophysical model is calculated based on enthalpy, internal energy, and compressibility. The transport properties are computed according to Suth-

erland's law [14],

$$\mu = A_s \frac{\sqrt{T}}{1 + T_s/T}, \tag{3.1}$$

where μ is the dynamic viscosity, T is the temperature, and A_s and T_s are the model coefficients [20]. Thus, Sutherland's model takes into account the effects of the temperature on the dynamic viscosity. Its evolution is plotted in Figure 3.6. It can be seen that it varies significantly around 296K, the temperature of the simulation. Taking into account this variation thus allows to model more accurately the gas.

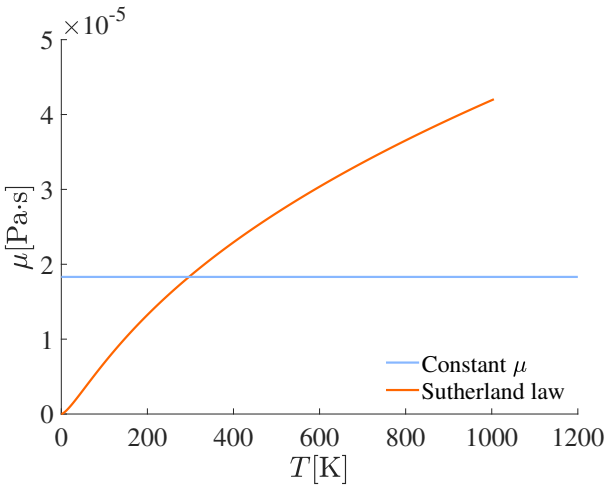

Figure 3.6: Comparison of Sutherland's law with the constant dynamic viscosity as a function of the temperature [14].

3.2.3 Turbulence model

All the flow features are now defined. Subsequently the options of the numerical simulation can be selected. For the momentum properties, since only the mean flow is of interest in this study, a RANS simulation is conducted. This choice is in accordance with other simulations of supersonic round jets [11, 13, 39, 40, 41].

Regarding the turbulence model, in the case of a cold jet in cold atmosphere [11], the Spalart-Allmaras model is selected. However, this is a one-equation model. It is thus the lowest level at which a model can be built. Hence it comes with clear limitations. For instance, it overestimates the spreading of the planar jet by over 40% [31]. To simulate a cold jet in hot atmosphere, the $k-\varepsilon$ turbulence model is chosen in the reference study [13]. However, in that case, the model had to be corrected to take into account the large fluctuations of the temperature. The choice of an adequate turbulence model thus cannot be inferred from the reference simulations. In the study conducted by the NASA [12] of a cold jet in cold atmosphere, the results from $k-\varepsilon$ and $k-\omega$ SST models are compared. They are reproduced in Figure 2.8. No major difference can be observed between both results. Therefore a model must be selected. Its validity is then verified by comparison with the other available models.

In OpenFOAM®, the turbulence models suitable for this application can be divided into two categories: the $k-\varepsilon$ and the $k-\omega$ based model. They are all two-equations turbulence models. In the former, the turbulence is solved depending on the turbulent kinetic energy k and the turbulence kinetic energy dissipation rate ε. In the latter, the turbulence specific dissipation rate ω is solved rather than ε. The initial models are thus $k-\varepsilon$ and $k-\omega$. From these, the

RNG $k-\varepsilon$, the $k-\varepsilon$ Realizable, the $k-\omega$ SST, and the $k-\omega$ (2006) models are derived [20].

The $k-\varepsilon$ model is reliable and widely used in industry [31, 42]. This model is used to simulate supersonic jet in a hot temperature field [6, 30]. However, it is known that this model over-predicts the spreading rate of round jets [31].

To counteract this limitation, the $k-\varepsilon$ Realizable model has been developed. The model coefficient for the turbulent viscosity C_μ is no longer constant. It depends on the mean strain- and rotation-rate tensors as well on the turbulence quantities. The spreading rate of round jets is consequently better estimated [31].
In the RNG $k-\varepsilon$ model, the mathematical technique called "renormalization group" is applied. Successively, the rate of production of turbulent kinetic energy and the rate of dissipation decrease. This model was implemented to answer one of the major criticisms of the $k-\varepsilon$ model. The latter is not derived from the Navier-Stokes equations in any systematic fashion [43].

The $k-\omega$ model is also a common solver. However, it is highly dependent on the turbulence of the freestream. This limitation is critical for this application. The derived models are therefore often preferred.

The $k-\omega$ (2006) includes the Wilcox correction. The latter involves different eddy viscosities to compute the eddy diffusivity of turbulent variables and Reynolds-stress tensor. Enhanced capability for supersonic flows are displayed into compression corners and hypersonic shock-wave/boundary-layer interaction. Moreover, it is less sensitive to the ω-value of the freestream than the $k-\omega$ model. Improvements in the modelisation of free shear flow is thus promised [44].

Due to its hybrid character, combining the $k-\omega$ model near the walls and the $k-\varepsilon$ model in the far field, the $k-\omega$ SST model is also widely used. Its reliability for transonic and supersonic flows has been shown [45, 46]. Moreover, the model was used to run similar simulations [12, 39].

In Section 3.3, during the validation process, the results obtained with these different turbulence models are confronted. The most adequate for this case can then identified. Meanwhile, since no major difference between the $k-\varepsilon$ and the $k-\omega$ SST models is highlighted, the latter is selected.

3.2.4 Solver

The solver for the simulation must be selected. The two solvers *rhoCentralFoam* and *rhoPimpleFoam* are conventionally used in industry to model supersonic flows in OpenFOAM®. Both solvers can thus handle supersonic, compressible flows. While *rhoCentralFoam* is a density-based solver, *rhoPimpleFoam* is pressure-based [20]. The solver *rhoCentralFoam* captures better flow separations, shocks, shear layers, and pressure profiles [40]. Therefore, this solver was preferentially used in similar simulations [39, 41]. However, Local Time Stepping is not available for this solver [20]. Since *rhoPimpleFoam* still provides good results, with the aim of reducing the computational time, the latter is rather selected.

3.2.5 Numerical schemes

An insight into the selected numerical schemes can be taken. As mentioned, the *localEuler* time scheme, performing Local Time Stepping, is selected [20]. The time step is thus locally computed depending on the maximal Courant number. The time step is therefore not uniform over the domain. It depends on the local velocity and local size of the elements. The evolution of the

flow over the iterations is therefore not physical. Only the converged simulation can be analyzed. Additionally, damping between each time step and smoothing of the time step over the domain is applied. According to the documentation, this scheme is explicit/implicit. Both behaviors are therefore observed. Consequently the Courant number cannot be drastically increased.

The divergence schemes are firstly set to *Gauss upwind*. This first order scheme is robust but too dissipative to provide acceptable results [20, 38, 42]. It is thus used to obtain a first solution quickly. Then the schemes are changed, for all fields except the turbulent quantities, to *Gauss limitedLinear* with the maximal limitation. As a result, this second order scheme switches to first order when the gradients are important. Hence this scheme is still robust but also reliable.

For the other schemes, their respective typical entry is selected [20].

3.2.6 Solution and algorithm control

To solve the pressure field, the GAMG, Generalised geometric-algebraic multi-grid, solver is used with a tolerance of $1{\cdot}10^{-6}$, and a relative tolerance of 0.01. For the last loop on the pressure, the relative tolerance is 0. The *GaussSeidel* smoother is selected. On the one hand, the tolerance is the value under which the residuals must fall. On the other hand, the relative tolerance prescribes the maximum value of the ratio between the current and initial residuals. For the record, multi-grid solvers solve the flow on coarser meshes. Then the solution is mapped onto a finer mesh and the flow is solved again. This procedure is applied until the solution on the mesh of the model is obtained [20].

Regarding the velocity field, the *PBiCGStab* solver, which is a stabilized version of Preconditioned bi-conjugate gradient, is applied with a *DILU* preconditioner, standing for diagonal incomplete-LU. It can thus handle asymmetric matrices. The tolerance is $1{\cdot}10^{-8}$, and the relative tolerance is 0.

For the turbulence quantities, the *smoothSolver* with a *symGaussSeidel* smoother is set. The same tolerances as for the velocity field are prescribed. Those solvers are selected because they are conventionally used for each respective field [20, 42]. The low tolerance imposed for the resolution leads to precise results.

3.2.7 Convergence strategy

The reach convergence, multiple parameters are adapted during the simulation. During the first iterations, entries associated to poor prediction of the flow are set. This helps the convergence of the solution. Once the flow starts to establish, the parameters are progressively modified. The residuals are monitored to determine the right time to make changes.

As already mentioned, the initial conditions must be carefully defined in order to reach convergence. They are illustrated in Figure 3.4.

At first, a relaxation of 0.5 is set on the velocity field. With relaxation, convergence is slower. However, it eases the first iterations of the simulation. Moreover the maximum Courant number is restrained to 0.2. This variable determines the local time step depending on the local velocity and the local element size. A low Courant number induces a low time step. At first, the convergence is therefore slow. Those two parameters are gradually increased over the iterations. Eventually, no more relaxation is set on the velocity field. The Courant number is increased to 0.8. If it is further raised, the simulation crashes.

Once the current simulation has converged, the parameters of the solver are modified throughout the simulation. The number of inner loops, in which the pressure field is corrected, and outer loops, during which all the fields are computed, of the PIMPLE algorithm are gradually increased over the iterations. They are initially set to a low value, respectively 1 and 3 to start the simulation. Then, they are increased to 3 and 5. Consequently, each iteration is longer but the resolution is more accurate as well.

Finally, the first order divergence schemes are changed to second order's. The latter indeed provides more reliable results. Once the simulation converges, an accurate model is therefore obtained.

The case is now set-up. The mesh is generated. Refinements of the elements is applied in the critical zones to capture effectively the boundary and the shear layers. The boundary conditions are defined to match the experimental conditions. The air properties are defined. The $k-\omega$ SST turbulence model is selected to run the RANS simulations. The *rhoPimpleFoam* solver is chosen. This allows to perform Local Time Stepping. A convergence strategy is also developed. The results must now be validated to ensure the accuracy of the modeling.

3.3 Validation

The choices and assumptions introduced in previous sections must be verified. Thus to validate the results, multiple parameters are studied. First, the convergence of the residuals and of the mass flow rate is checked. Additionally, the y^+ value is controlled to ensure that they fall in the prescribed range [38]. This validation process is carried out for each simulation. However, a reference simulation on a structured mesh with the parameters previously described is selected to lay out the procedure. Afterwards, a mesh convergence analysis is conducted with the help of Richardson interpolation [18]. This tools provides calculations to estimate the quantities obtained with a converged mesh. Consequently the error made by using the current mesh can be estimated. Finally, the influence of the modeling choices is studied. The effects of the boundary conditions are analyzed, and the impact of the turbulence model is investigated.

3.3.1 Convergence of the monitored quantities

In Figure 3.7 is represented the evolution of the residuals. A drastic increase can be observed at around $2.5 \cdot 10^4$ iterations, when the divergence schemes are switched from first to second order. Except for the internal energy e, the residuals then fall below $1 \cdot 10^{-5}$. Since the residuals of the internal energy are below $1 \cdot 10^{-4}$ and do not seem to further decrease, the solution has converged.

Regarding the mass flow rate, its evolution at the inlets is represented in Figure 3.8. It can be seen the inlet mass flow rate convergences rapidly, and that it is coherent with the estimated values. It can thus be taken as a reference to compute the relative error on the mass flow rate at the outlet illustrated in Figure 3.9a. During the last iterations, it can be seen in Figure 3.9b that the outlet mass flow rate differs of less than 0.1 % from the inlets'. The mass flow rate has thus converged.

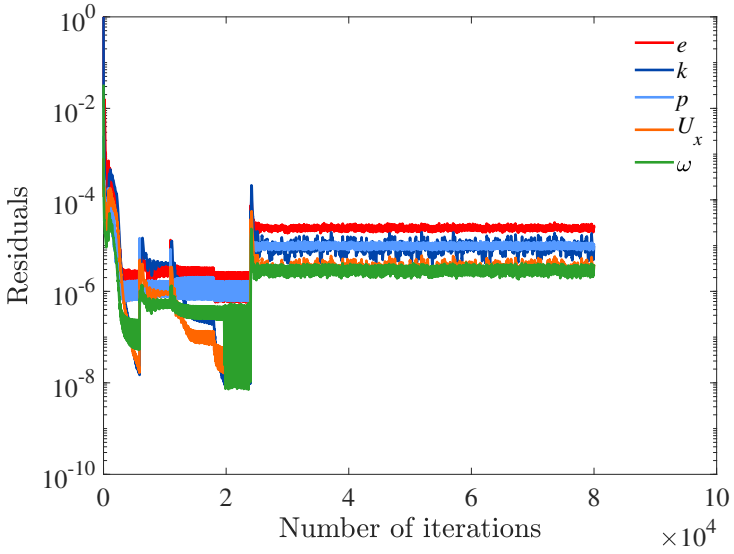

Figure 3.7: Supersonic jet in cold atmosphere: Evolution of the residuals over the iterations.

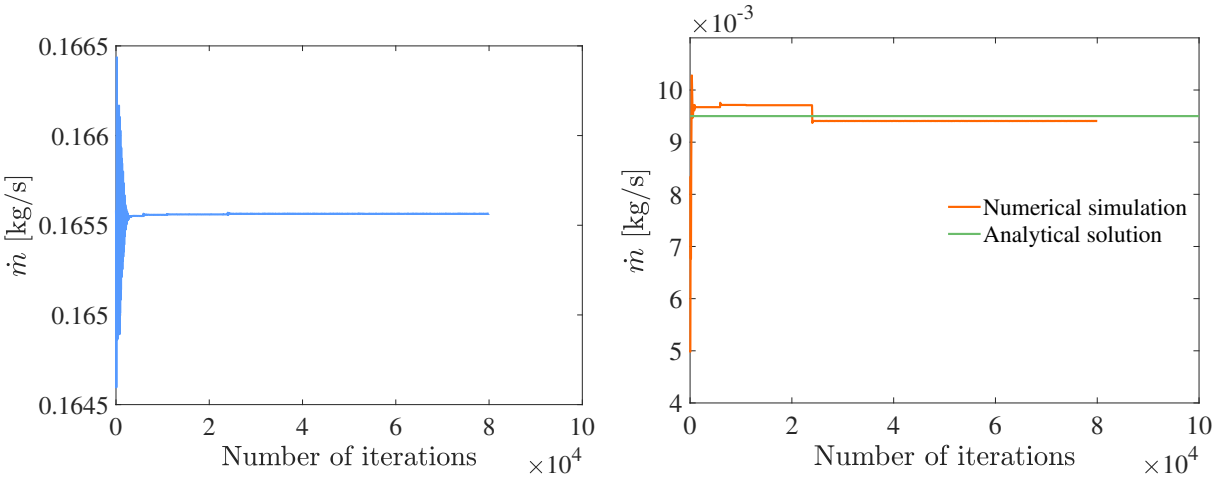

(a) AmbianceInlet. (b) ReservoirInlet.

Figure 3.8: Supersonic jet in cold atmosphere: Evolution of the mass flow rate through the inlets over the iterations.

Regarding the y^+ value at the walls, it is recommended to adapt the mesh such that y^+ ranges between around 20 and 100 [38]. Then, the first cell does not fall into the viscous sub-layer and the resolution of the boundary layer is adequate. The values at each wall is represented in Figure 3.10.

Since the walls are in the continuity of each other, the mesh near the wall is dependent. The modification of the size of the cells is thus limited. Moreover, at the nozzle outlet corner, the mesh should be refined to capture efficiently the interaction between the jet and the ambiance, and thus the development of the shear layer. Compromises on the refinement is thus necessary.

In Figure 3.10a and Figure 3.10b, it can be seen that the minimum and maximum value is close to the required range for the *nozzleWall* and the *reservoirWall*. The averaged value at the *lanceFrontWall* is in the prescribed range. At the lanceWall, the y^+ values are smaller that desired. However, the freestream velocity is small and has little influence on the jet [12]. The effects of its boundary layer should thus be negligible as well. Therefore, the trade-off on y^+ is adequate.

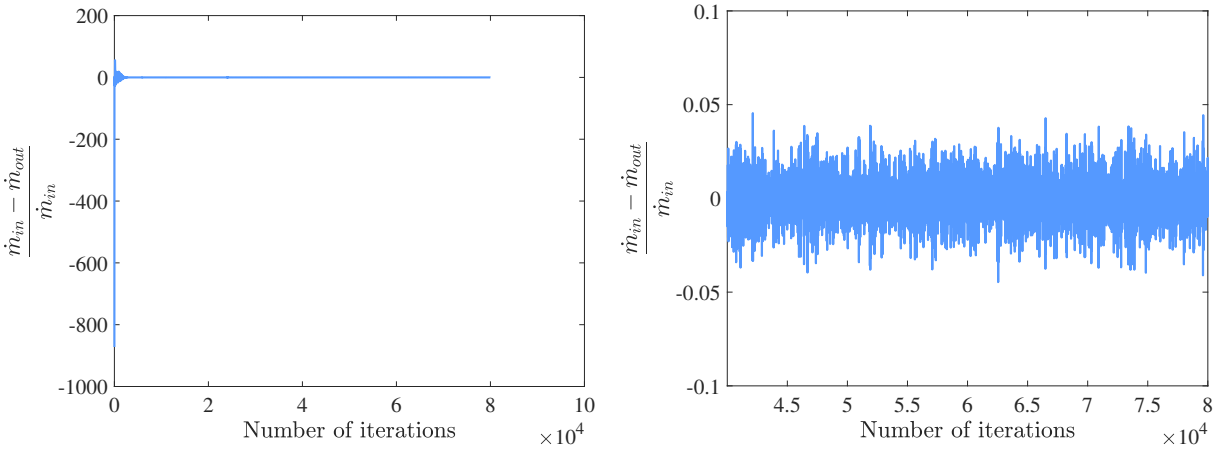

(a) Entire simulation. (b) Zoom on the last iterations.

Figure 3.9: Supersonic jet in cold atmosphere: Evolution of the relative error on the outlet mass flow rate over the iterations.

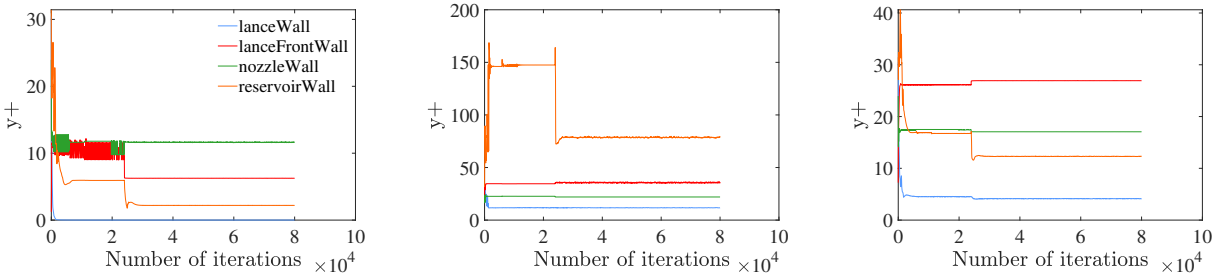

(a) Minimum value. (b) Maximum value. (c) Averaged value.

Figure 3.10: Supersonic jet in cold atmosphere: Evolution of the y^+ values over the iterations at each wall.

3.3.2 Mesh convergence

Now that the convergence of the simulation has been demonstrated, the convergence of the mesh is studied. In Figure 3.11 and Figure 3.12 are plotted the dimensionless centerline axial velocity for different sizes of structured and unstructured meshes against the experimental results.

It can be observed that with refinements, the results obtained on an unstructured mesh predict smaller potential core length. Contrary to the structured mesh, the unstructured leads to results which differ largely from the experiments as illustrated in Figure 3.13. This observation was already made by the NASA [12] and represented in Figure 2.8. As explained during the mesh generation process, unstructured meshes have non-regular elements. Consequently they are not oriented along the direction of the flow contrary to structured ones. The jet is therefore less accurately predicted. The option of simulating on unstructured meshes is thus definitely discarded. The mesh convergence is studied only for structured meshes.

To conduct the mesh convergence study, Richardson's interpolation is used. This tool quantifies the relative error made on the current mesh with respect to the extrapolated results on a converged mesh. As mentioned in Section 1, the length of the potential core is the quantity to consider to easily validate the results. It lasts until the centerline velocity drops to 90% of the

nozzle outlet velocity [17].

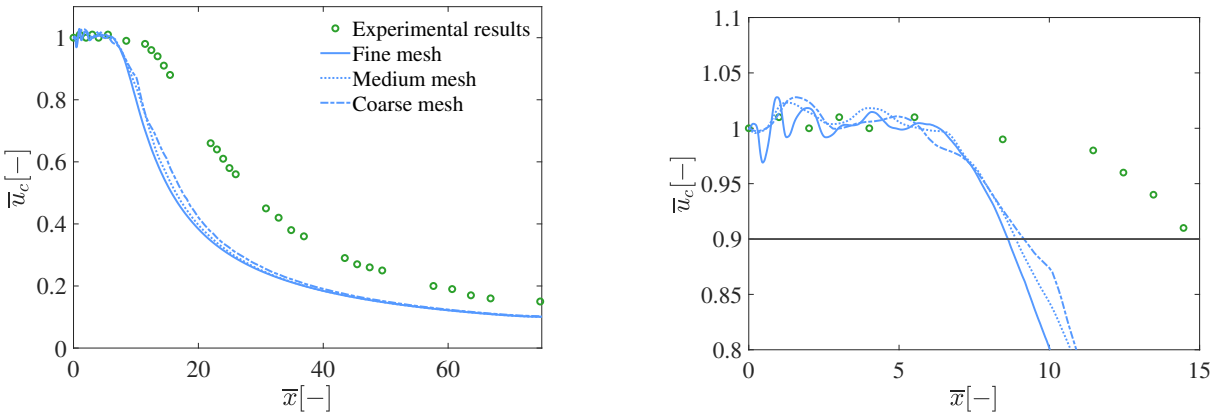

(a) Entire jet.

(b) Zoom on the potential core.

Figure 3.11: Supersonic jet in cold atmosphere: Comparison of the dimensionless axial centerline velocity for different refinements, gradually of 25425, 41848 and 99913 elements, of unstructured meshes with the experiments.

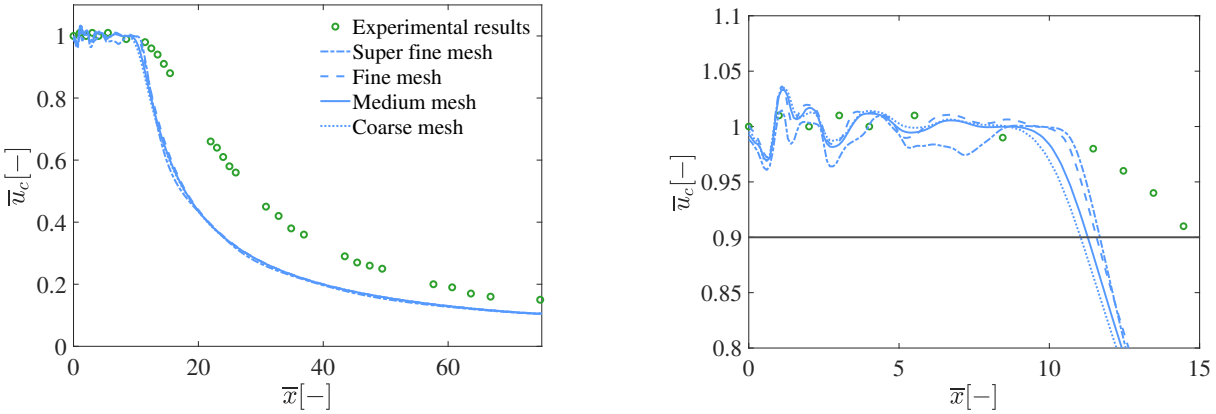

(a) Entire jet.

(b) Zoom on the potential core.

Figure 3.12: Supersonic jet in cold atmosphere: Comparison of the dimensionless axial centerline velocity for different refinements, gradually of 33865, 58814, 128685 and 257154 elements, of structured meshes with the experiments.

Richardson's interpolation is thus based on the potential core length [18]. The refinement factor is expressed as

$$f = \sqrt{\frac{N_{\text{finer}}}{N_{\text{coarser}}}}, \tag{3.2}$$

with N the number of cells in the mesh. Let f_1 be the refinement factor between the medium and the coarse meshes and f_2 between the fine and the medium meshes,

$$g = \frac{1}{\ln(f_2)} \left| \ln \left| \frac{\psi_1}{\psi_2} \right| + q(g) \right|, \tag{3.3}$$

where g is the apparent order of the method, $\psi = \phi_{\text{coarse}} - \phi_{\text{fine}}$, ϕ is the solution of interest, here the potential length, and

$$q(g) = \ln\left(\frac{f_2^g - s}{f_1^g - s}\right), \tag{3.4}$$

with $s = sgn(\psi_1/\psi_2)$.

The extrapolated value ϕ_{ext} can then be computed along with the extrapolated relative error e_{ext}.

$$\phi_{\text{ext}} = \frac{f_2^g \phi_{\text{fine}} - \phi_{\text{medium}}}{f_2^g - 1}, \tag{3.5}$$

and

$$e_{\text{ext}} = \left|\frac{\phi_{\text{ext}} - \phi_{\text{mesh}}}{\phi_{\text{ext}}}\right|. \tag{3.6}$$

Therefore the potential core length computed on a converged mesh can be estimated from Eq. 3.5. It is equal to $11.77D_{\text{out}}$. The relative errors expressed in Eq. 3.6 are listed in Table 3.1 for each mesh. The medium mesh is used for the last steps of the validation process and to extract results. The finer meshes are indeed more sensitive and obtaining a converged solution is more difficult. The medium mesh is thus a good compromise.

Table 3.1: Supersonic jet in cold atmosphere: Richardson's correlation on the potential core length [17, 18].

	Coarse mesh	Medium mesh	Fine mesh	Super fine mesh
N	33865	58814	128685	257154
e_{ext}[%]	6.10	3.97	1.43	0.58

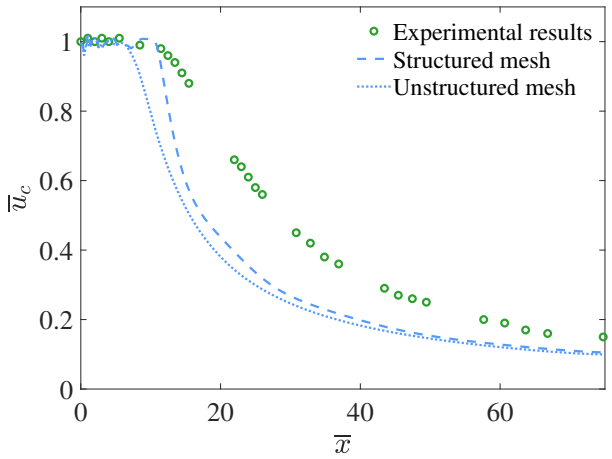

Figure 3.13: Supersonic jet in cold atmosphere: Comparison of the dimensionless axial centerline velocity for the finest structured, of 257154 elements, and unstructured, of 99913 elements, meshes with the experiments.

3.3.3 Influence of the boundary conditions

The influence of the boundary conditions is highlighted in Figure 3.14. The relative change of the potential length with respect to the reference set-up is listed in Table 3.2 for each boundary condition. It is asserted that the freestream has little effect on the jet. Moreover, setting the *ambiance Wall* to an inviscid wall, rather than to a freestream as in the reference simulation [12],

did not impact significantly the flow. Thus, the assumptions in the ambiance have a limited impact on the jet characteristics.

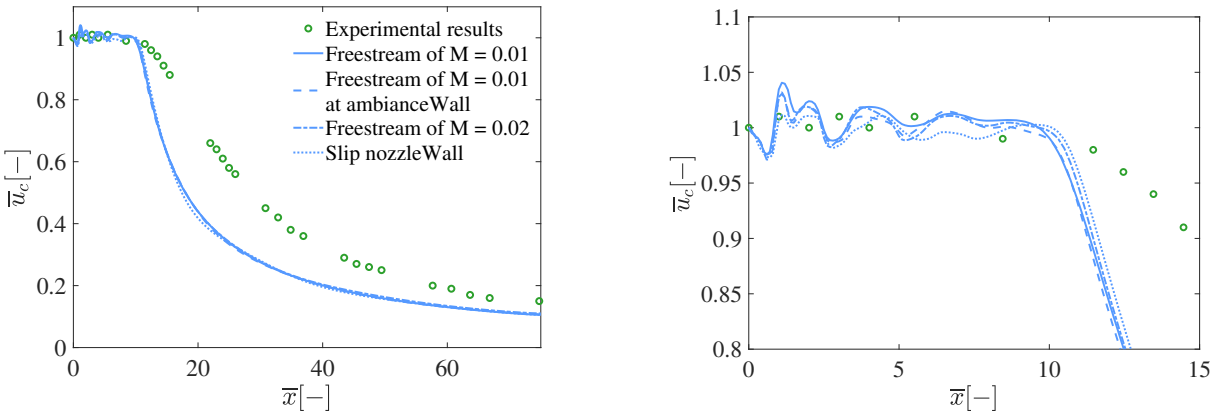

(a) Entire jet.

(b) Zoom on the potential core.

Figure 3.14: Supersonic jet in cold atmosphere: Comparison of the dimensionless axial centerline velocity for different boundary conditions with the experiments.

Table 3.2: Supersonic jet in cold atmosphere: Relative change of the potential core length with respect to the reference simulation on a medium mesh.

	Reference simulation	Freestream at the walls	Higher freestream	Slip walls
Change [%]	0	0.89	0.89	2.65

Regarding the boundary conditions in the nozzle, it can be inferred that the viscous walls have a slightly bigger effect on the jet, as it could be expected. However, it does not significantly influence the flow. This observation can be useful for further simulations to simplify the case with slip walls.

Simulations without a nozzle, with the uniform corresponding fields imposed at the outlet, have also been carried out. However, none has converged, despite changing the initial and boundary conditions. Numerical instability has been observed along the centerline and its cause could not be identified. This simplification thus cannot be made for next more complex simulations.

3.3.4 Influence of the turbulence model

Finally, the results from the different turbulence models described in Section 3.2.3 are studied and represented in Figure 3.15. It can be seen that the $k-\varepsilon$ based models estimate the potential length more accurately. Both the $k-\omega$ and the $k-\omega$ SST models underestimate the length of the potential core while $k-\omega$ with the Wilcox 2006 correction overestimates it. However it predicts the best the velocity decay. As mentioned, the modeling of free shear jets is indeed improved with the implemented modifications. In the RNG $k-\varepsilon$ model, which includes a renormalization, there is slightly less dissipation [17]. This can indeed be observed in Figure 3.15a. However, the velocity decay is still not well estimated. The better prediction is provided by the $k-\varepsilon$ Realizable model. This model indeed accounts for the round jet anomaly of the $k-\varepsilon$ model in which the spreading and the velocity decay are overestimated [31].

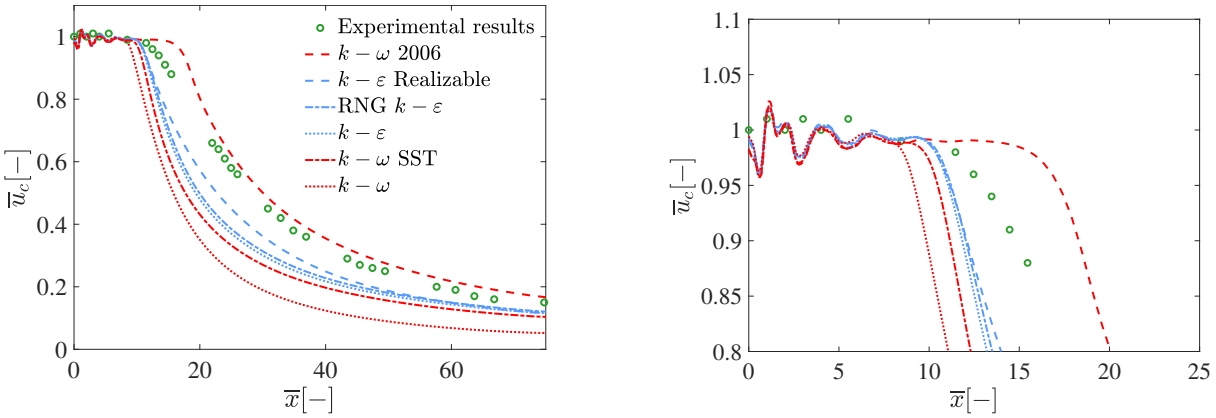

(a) Entire jet.

(b) Zoom on the potential core.

Figure 3.15: Supersonic jet in cold atmosphere: Comparison of the dimensionless axial centerline velocity for different models of turbulence with the experiments.

Those observations therefore confirm the limitations of each model presented in Section 3.2.3. However none of the models stands out from the others. An additional validation method is introduced to determine which turbulence model is optimal. For a supersonic round jets, if $x/D_{\text{out}} > 30$, the velocity profiles are self-similar. Thus, the axial velocity profiles at multiple axial positions are studied for each turbulence model. Their validity is confirmed if self-similarity is observed. The radial coordinate r is non-dimensionalized by the half-radius $r_{1/2}$, the radial distance at which the axial velocity is half of the centerline's. With this non-dimensionalization, the profiles at each axial distance should superpose [31]. Also, they should be described by the exponential law [8],

$$\overline{u}_c = \exp\left(-\log(2)\left(\frac{r}{r_{1/2}}\right)^2\right). \tag{3.7}$$

The profiles are represented for all the turbulence models in Figure 3.17. It can be seen that all profiles are self-similar except for the $k-\omega$ and the $k-\varepsilon$ Realizable models. While in Figure 3.15, the latter seemed to provide the best prediction of the flow. Its validity is now questioned. Regarding the other $k-\varepsilon$ based models, the results almost do not differ, as previously observed. For $x/D_{\text{out}} > 30$, they are close to the analytical solution. Good results are also observed for the $k-\omega$ SST model. The $k-\omega$ 2006 turbulence model also provides acceptable estimations but they are further from the reference law. Among the turbulence models, as there is little difference with the RNG $k-\varepsilon$ and the $k-\varepsilon$, the $k-\varepsilon$ turbulence model is thus selected.

While the location at which the velocity starts decaying is well approximated, the velocity decay is overestimated. To improve the prediction of the flow, as advised by Pope [31], the constants of the standard model can be adapted. They were indeed determined to fit most cases. They might therefore not be optimal for all set-ups. In his thesis, Lebon suggests to use a value of C_μ of 0.07 for this range of temperatures with the $k-\varepsilon$ model [19]. The axial centerline velocity obtained in both cases is plotted in Figure 3.16.

It can be seen that decreasing C_μ leads to a better estimation of the velocity decay. The turbulent viscosity ν_t is indeed directly proportional to this constant. The higher the turbulent viscosity, the more dissipation and thus the higher is the velocity decay. The constant value is not determined for this current set-up. For instance, here air is considered while Lebon's study is conducted with pure oxygen [19]. Hence it is compared with results obtained with other values of

C_μ. It can be seen that none of the considered values leads to an accurate prediction of the flow. The velocity decay is in fact not perfectly estimated. Below $20D_{\text{out}}$, a value of C_μ of 0.05 seems to provide better results while the prediction further down stream is more accurate with C_μ equal to 0.06. The latter is chosen to continue the analysis of the results since the characteristics at the bath, above $45D_{\text{out}}$ are sought. The choice of this value is confirmed by the correlation developed by Lebon to estimate the adequate value of C_μ. It depends on the enthalpy h of the flows as

$$C_\mu = A \exp\left(-B\frac{h_{\text{amb}}}{h_{\text{out}}}\right), \tag{3.8}$$

where A and B are constants respectively equal to 0.081 and 0.14. For this configuration, a value of C_μ of 0.064 is advised.

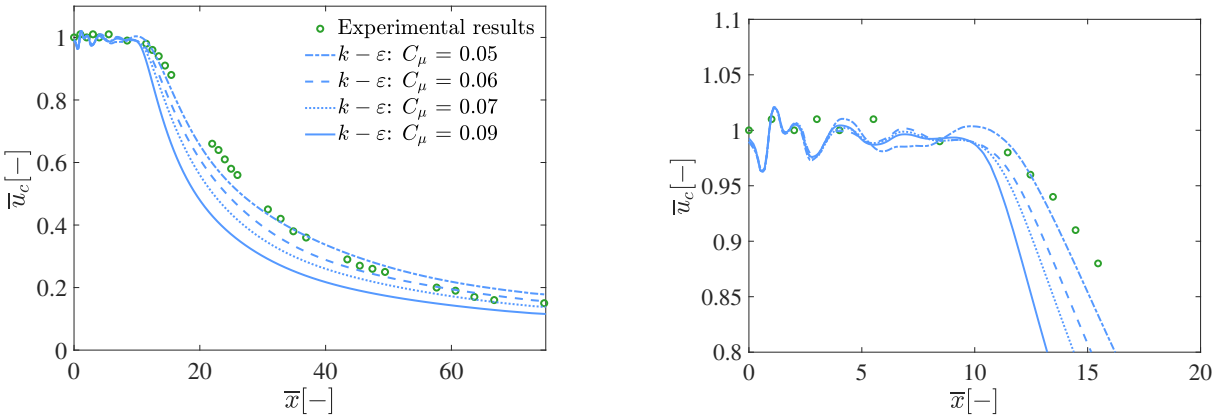

(a) Entire jet.

(b) Zoom on the potential core.

Figure 3.16: Supersonic jet in cold atmosphere: Comparison of the dimensionless axial centerline velocity for different values of C_μ with the $k-\varepsilon$ turbulence model.

The influence on the flow of the choice of the turbulence model and of the value of the coefficients is significant. It is the simulation parameters that influence the most the flow. Therefore, selecting the finest mesh is not relevant as the gain of precision is lower than the effects of the turbulence model. This reinforces the choice of pursuing the analysis with the *medium mesh*.

To conclude, the validation of the results is carried out. It is shown that the convergence of the simulation is ensured by monitoring the residuals and the mass flow rate. Additionally, the y^+ values at the walls are tracked to check that they fall in the recommended range for the use of *wallFunctions*. Afterwards, it is demonstrated that unstructured meshes do not provide reliable results, despite mesh refinements. Through a mesh convergence analysis using Richardson's correlation, the relative error on each mesh is identified [18]. The *medium mesh* is selected to analyze the results. Moreover, it is confirmed that the choice of the boundary conditions has little effect on the jet characteristics. Finally, a comparison between the turbulence models is carried out. It is highlighted that the influence of the turbulence model on the flow is the most significant among all parameters. The $k-\varepsilon$ model leads to the most accurate results. The standard coefficients value of C_μ is adjusted to 0.06. Thus, to study the characteristics of the jet, a simulation run with a $k-\varepsilon$ turbulence model with C_μ equal to 0.06 on a structured *medium mesh* is considered.

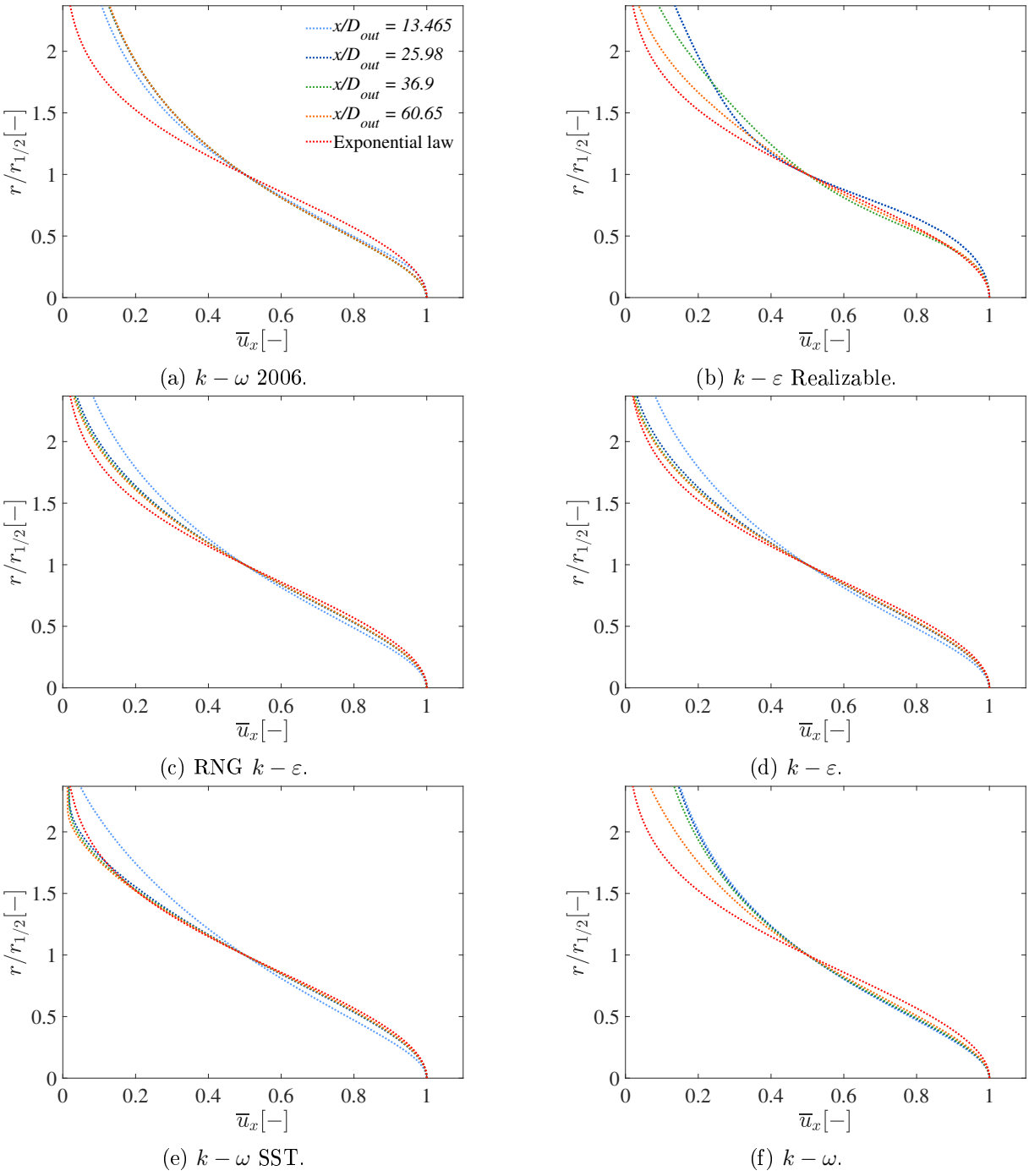

(a) $k-\omega$ 2006.

(b) $k-\varepsilon$ Realizable.

(c) RNG $k-\varepsilon$.

(d) $k-\varepsilon$.

(e) $k-\omega$ SST.

(f) $k-\omega$.

Figure 3.17: Supersonic jet in cold atmosphere: Comparison of the dimensionless axial velocity profiles at multiple axial distance for different models of turbulence with the exponential law.

3.4 Results

The validity of the simulations, of the choices, and of the assumptions is proven. Results can thus now be studied and compared to the reference experimental, analytical and numerical references. Conclusions can subsequently be drawn.

First the dimensionless centerline axial velocity is plotted against the correlation of Witze introduced in Section 2.2 and the reference numerical simulations by the NASA [9, 11]. Afterwards, the axial velocity profiles at multiple axial distances are compared with the experimental and reference numerical results. The spreading of the jet is characterized. Finally some key quantities of the jet flow, including related to the turbulence, are illustrated.

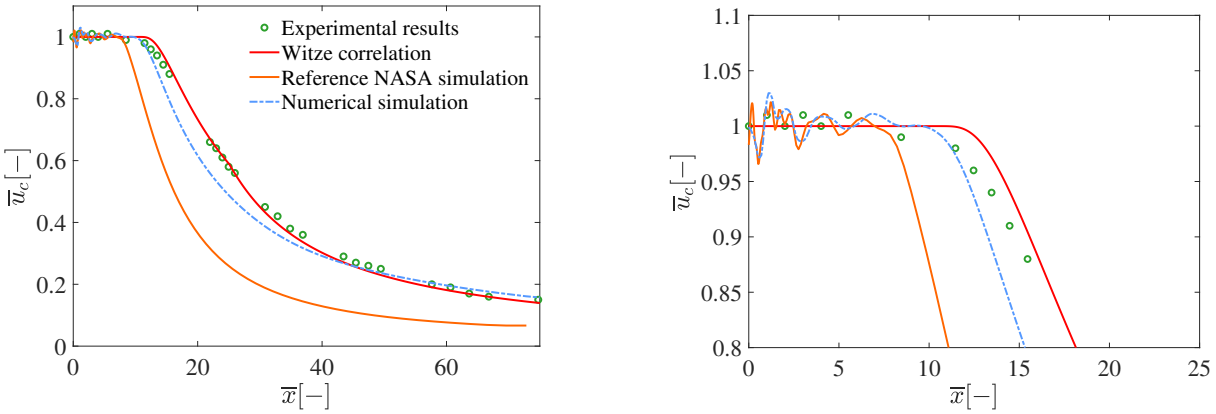

(a) Entire jet.

(b) Zoom on the potential core.

Figure 3.18: Supersonic jet in cold atmosphere: Comparison of the dimensionless axial centerline velocity from the simulation with the reference, experimental, analytical and numerical, results.

In Figure 3.18 is plotted the dimensionless axial velocity extracted from the simulation against the experimental results, the NASA numerical simulations, and the correlation of Witze introduced in Section 2.2. The computed potential core length from the correlation is $15.38 D_{\text{out}}$. Since the latter was built with Eggers' experiments as a reference, the correlation matches perfectly the experimental results. The NASA simulation provides a poor estimation of the flow. The error on the potential length is 38%. The use of Spalart-Allmaras turbulence model is probably the cause of this large error. This model is indeed not accurate due to its high-dissipative character [31].

The current study models more accurately the velocity decay. A significant improvement with respect to the reference simulation is observed. However, as for some simulations run on similar cases [12], it is still slightly overestimated. The error made on the potential length is 14.17%.

The length during which the velocity is constant is $11.2 D_{\text{out}}$, $10.0 D_{\text{out}}$ and $7.2 D_{\text{out}}$ respectively for the Witze correlation, the current simulation, and the simulation carried out by the NASA. The error of this study is then of 12% against 36% for the reference simulation. A clear improvement of the prediction is thus obtained.

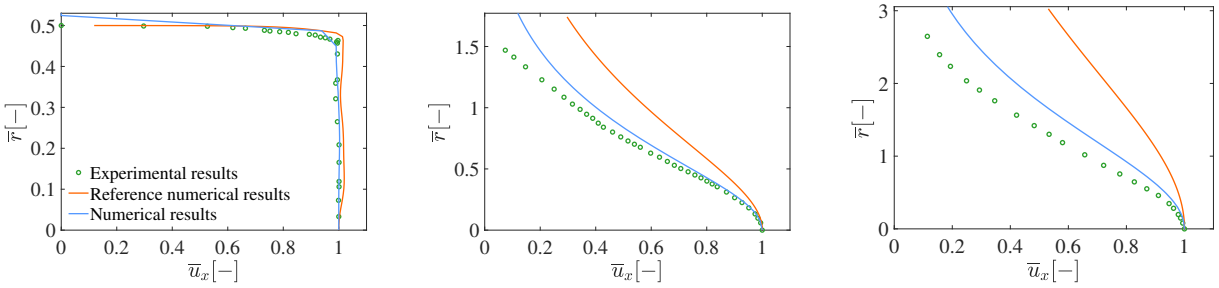

(a) $\overline{x} = 0$ (b) $\overline{x} = 13.465$ (c) $\overline{x} = 25.98$

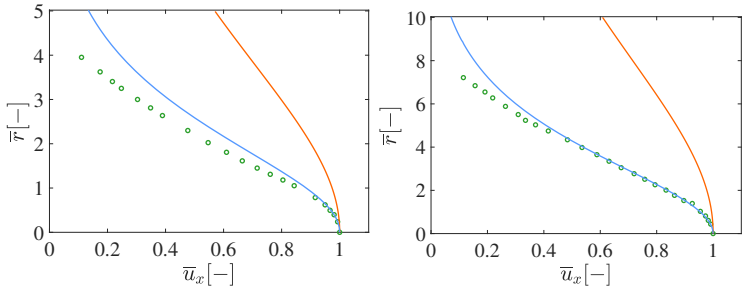

(d) $\overline{x} = 36.9$ (e) $\overline{x} = 60.65$

Figure 3.19: Supersonic jet in cold atmosphere: Comparison of the dimensionless axial velocity profiles from the numerical simulation with the reference results for multiple axial distances.

The dimensionless axial velocity profiles are plotted against the reference numerical and experimental results for multiple axial distances in Figure 3.19. At the nozzle exit, it can be seen that the profile is accurately predicted. The spreading rate is then over-predicted by the NASA numerical simulations as previously highlighted. The current study also slightly overestimates it. However, for some axial distances, a great match of the profiles is observed. The accuracy of the current model is thus demonstrated.

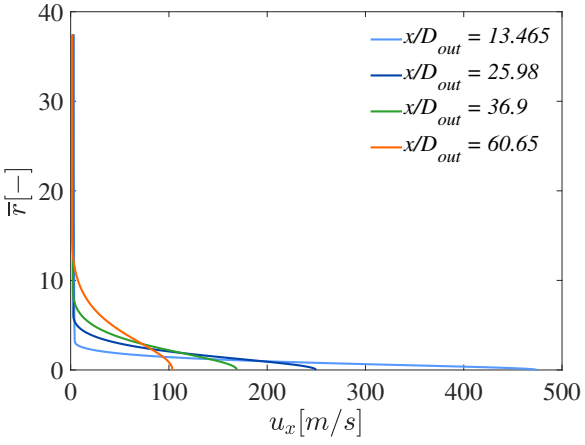

Figure 3.20: Supersonic jet in cold atmosphere: Evolution of the axial velocity profiles for multiple axial distances.

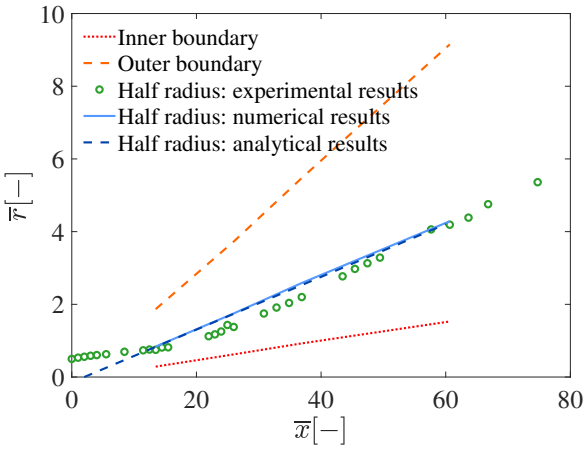

Figure 3.21: Supersonic jet in cold atmosphere: Evolution of the mixing layer's boundaries over the axial distance and comparison of the computed half radius with the reference results.

These profiles are illustrated together in Figure 3.20. The spreading and the dissipation of the jet is highlighted. The effects of the jet described in Section 1 can be inferred. The further

the jet is from the bath, the smoother, the wider, and the slower is the jet at the bath level. Therefore a high lance configuration is used to oxidize the silicon. A lower lance leads to a narrow, fast, penetrating jet ideal for the removal of the carbon content.

The spreading can be further studied by computing the boundaries of the mixing layer. The inner and outer boundaries are defined as the radial distance where the velocity is respectively equal to $U_{\text{amb}} + 0.9(U_{\text{c}} - U_{\text{amb}})$ and $U_{\text{amb}} + 0.1(U_{\text{c}} - U_{\text{amb}})$ [31]. Additionally, the half radius, the radial distance at which the velocity is half of the centerline's, can be computed and compared with the experimental data. In the self-similarity region, the free shear jet spreads linearly [8, 31]. The half radius can then be expressed as

$$r_{1/2} = S(x - x_0), \tag{3.9}$$

with S, the spreading rate, and x_0 the virtual origin. Figure 3.21 illustrates these jet's characteristics.

As stated, the half radius increases linearly with the axial distance. By identification, it is found that S and $\overline{x}_0$ are respectively equal to 0.0725 and 2. It can be once again observed that the spreading of the jet is correctly evaluated. The spreading is linked to the development of the mixing layer. The latter is induced by turbulent entrainment. Therefore, by adapting the value of C_μ, the turbulent entrainment is correctly estimated and susequently the spreading as well.

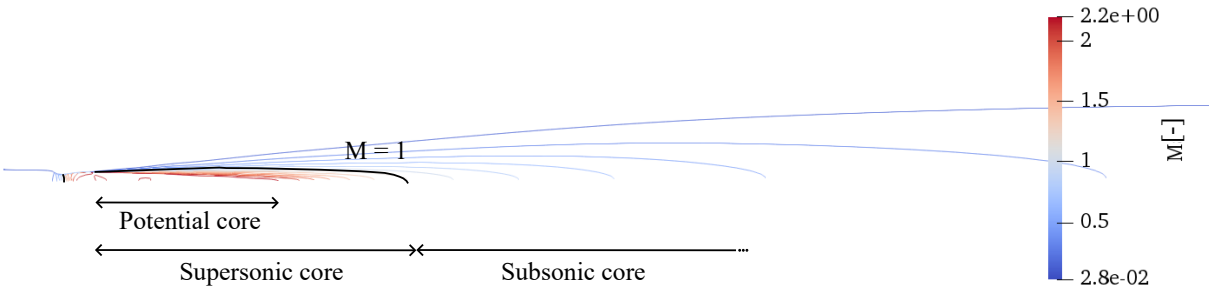

Figure 3.22: Supersonic jet in cold atmosphere: Contour plot of the evolution of Mach number trough the flow.

The spreading and the smoothing of the jet can also be observed on the Mach contour plot illustrated in Figure 3.22. Moreover, the sonic point is highlighted in black. It can thus be seen that Mach 1 is reached at the throat. The supersonic length can be identified. It lasts $18D_{\text{out}}$. Also, the design Mach is obtained at the nozzle exit. At the outlet, the contour indicates that shocks might however occur. Numeric schlieren and a shadowgraph are used in the optic of verifying this observation.

The numeric schlieren is displayed in Figure 3.23 and the shadowgraph in Figure 3.24. The range is restrained to observe the flow at the nozzle outlet. Some shocks then appear in the divergent and in the potential length. The nozzle is thus not perfectly adapted. A perfectly adapted nozzle is indeed rare. Moreover previous results verify the model. The validity of the model is therefore not questioned.

Finally, the turbulent viscosity and turbulent kinetic energy are represented in Figure 3.25. The turbulent kinetic energy is high along the potential core, where the velocity gradients are the most important, while the turbulent viscosity is high in the downstream of the jet. The turbulent viscosity is indeed linked with the turbulent entrainment starting after the potential

core length. It causes the the development of the mixing layer. Its spreading can be observed.

(a) x-direction: Entire range.

(b) x-direction: Custom range.

(c) y-direction: Entire range.

(d) y-direction: Custom range.

Figure 3.23: Supersonic jet in cold atmosphere: Numeric schlieren at the nozzle exit.

(a) Entire range.

(b) Custom range.

Figure 3.24: Supersonic jet in cold atmosphere: Shadowgraph at the nozzle exit.

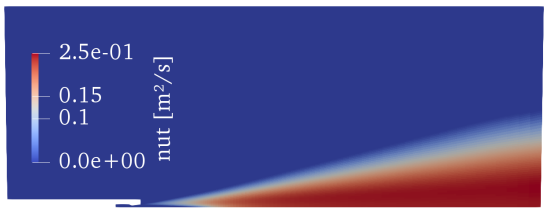

(a) Turbulent viscosity ν_t.

(b) Turbulent kinetic energy k.

Figure 3.25: Supersonic jet in cold atmosphere: Illustration of the turbulent quantities, the turbulent viscosity and turbulent kinetic energy, in the flow.

To conclude, the experiments of a cold jet in cold atmosphere conducted by Eggers [8] are reproduced with success using only open source tools. After validating the results, it is shown that the current simulation produces more accurate estimations of the flow than the reference simulation [11]. Both the centerline axial velocity and the velocity profiles are analyzed. The spreading rate and mixing layer boundaries are computed. The model reproduces accurately the experimental results. The tools to analyze the flow are presented as well. As the model for a cold case is verified, the case of a cold jet in hot atmosphere conducted by Sumi [16] can now be studied. This configuration is important to get a closer reproduction of the BOF conditions. The effects of the temperature on the supersonic jet is then highlighted.

4 Supersonic jet in hot atmosphere

The single supersonic jet in cold atmosphere model is validated. However the aim of this study is to develop a model in a hot temperature field to get a close reproduction of the BOF environment. In fact, in the BOF, temperature increases up to around 1900K.

Therefore the effects of temperature on the jet are now studied. The experiments conducted by Sumi introduced in Section 2 are reproduced [16]. Three ambient temperatures are considered in that study: 285K, 772K, and 1002K. The hotter case is first considered to validate the model in a high temperature field. The process is conducted similarly as for the cold jet in cold atmosphere. Afterwards, the behavior of the jet at bath level is investigated. It is indeed the aim of the model. Finally the results are analyzed for each experimental condition. The influence of the temperature on the flow is highlighted. The impact of temperature fluctuations on the BOF process is consequently determined.

4.1 Case set-up

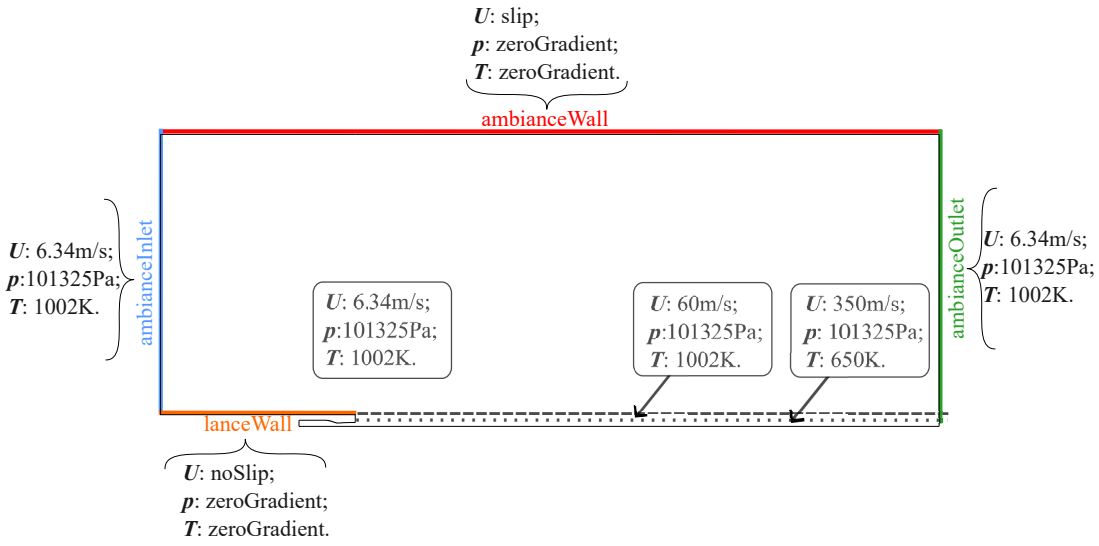

(a) Overall domain.

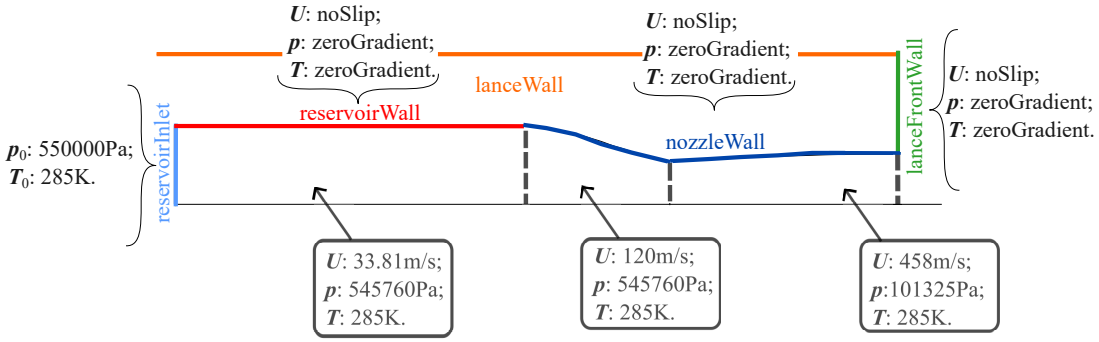

(b) Zoom on the nozzle.

Figure 4.1: Supersonic jet in hot atmosphere: Boundary conditions, in color, and initial conditions, in gray.

The case is set-up similarly to the cold jet in cold atmosphere. The parametrization of the geometry is the same with the nozzle coordinates adapted according to Appendix A. The transfinite mesh is constructed as described in Section 3.1.

Also, the same types of boundary conditions are used. Their value is however adapted to the current case. They are represented in Figure 4.1 along with the initial conditions. The limitations of these assumptions can therefore be inferred from the cold case. A Mach 0.01 freestream is still considered in the ambiance to avoid any numerical instabilities. The total pressure set at the *reservoirInlet* is higher than the one prescribed in the simulations conducted by Alam to account for the losses in the nozzle [13]. In fact, as presented in Figure 2.7, the nozzle was not simulated by Alam. However, in the case of a cold jet in cold atmosphere, this simulation was unsuccessful due to numerical instabilities. A similar domain to the cold case is thus built.

The same zones as the previous case are defined for the initial conditions. Here a non-uniform temperature field is additionally set. Large temperature fluctuations indeed occur in the flow. Hence these initial conditions ease the convergence. As for the cold case, the values are determined such that the variations of the fields between each zone is smooth.

Regarding the thermophysical properties, the same laws are used and adapted to pure oxygen. It is indeed assumed that, contrary to the atmosphere composition listed in Table 2.3, only oxygen is present. This assumption seems reasonable at high temperature since the concentration of the other species is low with respect to the oxygen's. With respect to the BOF, this composition of the jet is therefore accurately modeled. However the complexity of the ambiance composition is not maintained. The mixing of the species is therefore not modeled. This assumption impacts the spreading prediction of the flow. The density of the ambiance is indeed not accurate and the possible reactions are disregarded.

Finally, in the light of the results from Section 3.3, the $k-\varepsilon$ turbulence model is chosen to conduct the validation process. Moreover, this model was also selected by Alam, with nevertheless some modifications [13].

4.2 Validation

The results provided by the model in a hot temperature field are verified. The same validation process as for the cold jet is pursued. The convergence of the residuals, of the mass flow rate and the y^+ values are checked. They are however not illustrated again to avoid redundancy. The reliability of the selected turbulence model must be checked.

The prediction on the converged mesh is plotted against the experimental results in Figure 4.2. It can be seen that the simulation predicts poorly the centerline axial velocity. Also oscillations in the potential core are observed. They reflect a possible non-adaptation of the flow. This is verified in Section 4.3.

Moreover the velocity decay is overestimated. With respect to the case of a cold jet in cold atmosphere, higher temperature fluctuations now occur in the flow. Thus its influence on the thermophysical properties might have to be considered to accurately model the flow.

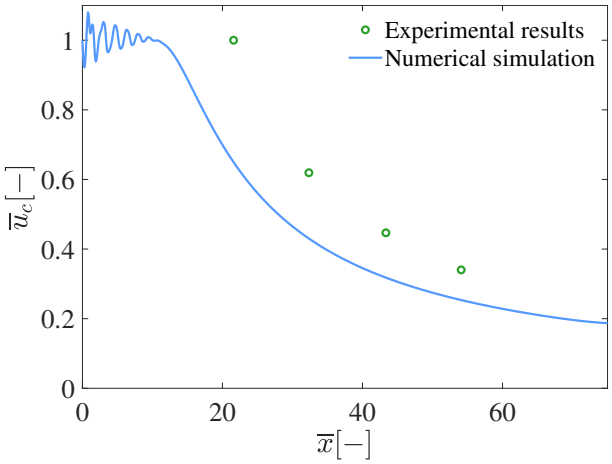

Figure 4.2: Supersonic jet in hot atmosphere: Comparison of the dimensionless axial centerline velocity of a simulation with the $k-\varepsilon$ model with the experimental results.

4.2.1 Influence of the thermophysical properties

In the current simulation, the only variable assumed constant with temperature is the heat capacity at constant pressure c_p. Its variation with temperature can be taken into account according to the JANAF tables [15].

With $a_0, ..., a_4$ the temperature constants, R the gas constant and T the temperature, the heat capacity at constant temperature can be expressed as

$$c_p = R((((a_4T + a_3)T + a_2)T + a_1)T + a_0). \tag{4.1}$$

The comparison between the constant and the JANAF calculated values is represented in Figure 4.3. It can be seen that while the fluctuations were small in the cold atmosphere, they are significant between a cold jet and a hot field. Taking them into account should thus provide a closer reproduction of reality.

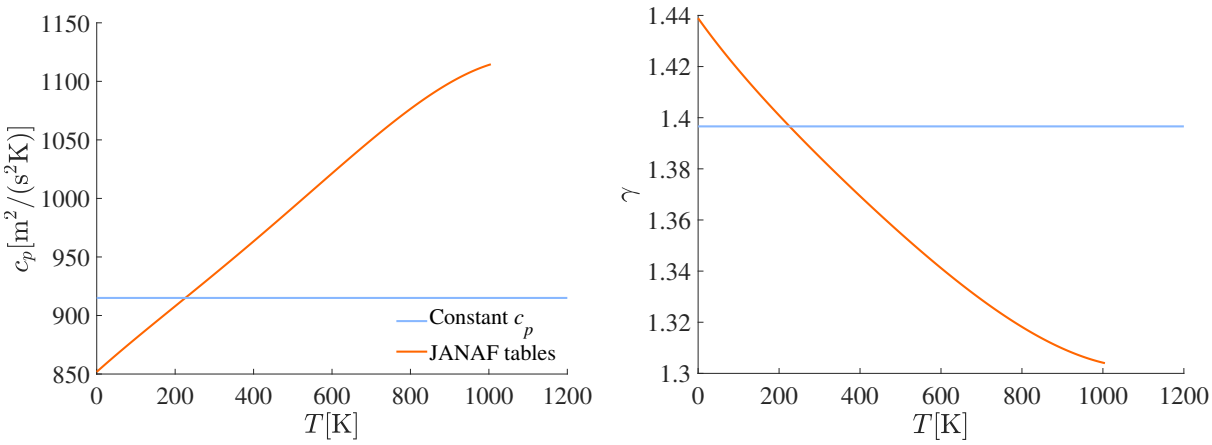

(a) Heat capacity at constant pressure.

(b) Heat capacity ratio.

Figure 4.3: Supersonic jet in hot atmosphere: Evolution of the thermophysical properties with the temperature and comparison with a constant value [15].

In the model, two sets of coefficients are prescribed, for the low and high temperatures. The coefficients switch at the *common temperature* of 1000K. Only the low temperature coefficients are thus used in this case. The lowest and highest temperature of the model must be defined as well. The lowest temperature allowed by the model is 200K but in the simulation it falls as low as 170K. The lower limit is thus adapted. As it can be seen in Figure 4.3, modifying this limit is acceptable since the polynomial behavior does not change in this range.

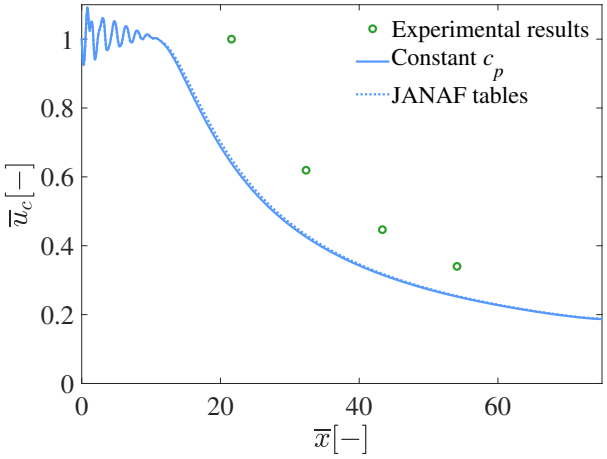

Figure 4.4: Supersonic jet in hot atmosphere: Comparison of the dimensionless axial centerline velocity obtained with constant and temperature dependent thermophysical properties.

The dimensionless axial centerline velocity obtained in both cases is represented in Figure 4.4. An almost unnoticeable change in the velocity decay can be observed. The thermophyscial properties are thus not responsible for the inaccurate estimation of the flow. The choice of the turbulence model is thus investigated.

4.2.2 Influence of the turbulence model

In the reference simulation conducted by Alam [13], a corrected $k-\varepsilon$ turbulence model is built to take into account the influence of high temperature gradients. It is an adaptation of the correction proposed by Abdol-Hamid [35].

With the modifications introduced by Alam, the value of C_μ is computed as

$$C_\mu = \frac{0.09}{C_\mathrm{T}}, \tag{4.2}$$

with

$$C_\mathrm{T} = 1 + \frac{1.2T_\mathrm{g}^{0.6}}{1 + f(\mathrm{M}_\tau)}. \tag{4.3}$$

In Eq. 4.3, M_τ is the turbulence Mach number. It is expressed as

$$\mathrm{M}_\tau = \frac{\sqrt{2k}}{a}, \tag{4.4}$$

where k is the turbulent kinetic energy and a is the speed of sound. The function of the turbulence Mach number $f(\mathrm{M}_\tau)$ is then calculated according to

$$f(\mathrm{M}_\tau) = (\mathrm{M}_\tau^2 - \mathrm{M}_{\tau 0}^2)H(\mathrm{M}_\tau - \mathrm{M}_{\tau 0}), \tag{4.5}$$

with $M_{\tau 0}$, a constant equal to 0.1 and $H(x)$, the Heaviside function.

Finally, the variable T_g in Eq. (4.3) can be obtained as a function of the local total temperature T^0,

$$T_g = \frac{|\nabla T^0|(k^{3/2}/\varepsilon)}{T^0}. \tag{4.6}$$

Thus, this model requires an access to the temperature, the turbulent quantities as well as the pressure to compute the speed of sound.

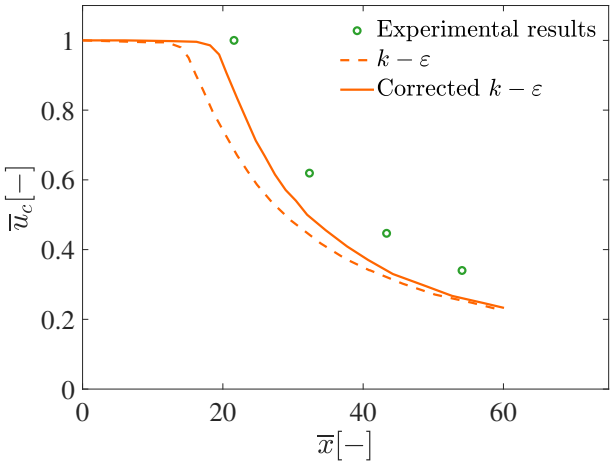

Figure 4.5: Alam's simulations: Comparison of the dimensionless axial centerline velocity with the standard $k-\varepsilon$ and the corrected $k-\varepsilon$ turbulence models [16].

The results obtained by Alam with both models are compared in Figure 4.5. The corrected turbulence model predicts significantly more accurately the potential length. Using this turbulence model for the simulation is thus highly attractive. In OpenFOAM®, this modification is not implemented and no turbulence model takes into account the temperature fluctuations. Only the velocity and the density fields are indeed communicated with the *momentumTransportModel*. The latter must be modified to take into account the temperature and the pressure. However, this model is one of the main basic component. It is thus incorporated into most of the solver's files. Modifying the latter would thus require a deep reconstruction of the entire solver. Other options to reproduce the results are thus investigated.

Some studies also obtained reliable results without implementing the correction [6, 30]. For instance, in his thesis, Doh adapted the values of C_μ according to the calculations of Lebon [19]. This is suggested by Pope as well [31]. The standard values have indeed been determined to accurately model most cases. Nevertheless, in some situations, another set of coefficients is more optimal as it has been illustrated for the cold atmosphere. The adjusted values are listed in Table 4.1.

Table 4.1: Supersonic jet in hot atmosphere: Adjusted values of C_μ for different ambiance temperatures computed by Lebon[19].

T [K]	285	772	1002
C_μ [-]	0.07	0.06	0.05

Therefore, firstly, the turbulence models described in Section 3.2.3 are plotted against each other. Also, a simulation with the modified C_μ is conducted. The comparison of the dimensionless axial centerline velocity for all models is represented in Figure 4.6.

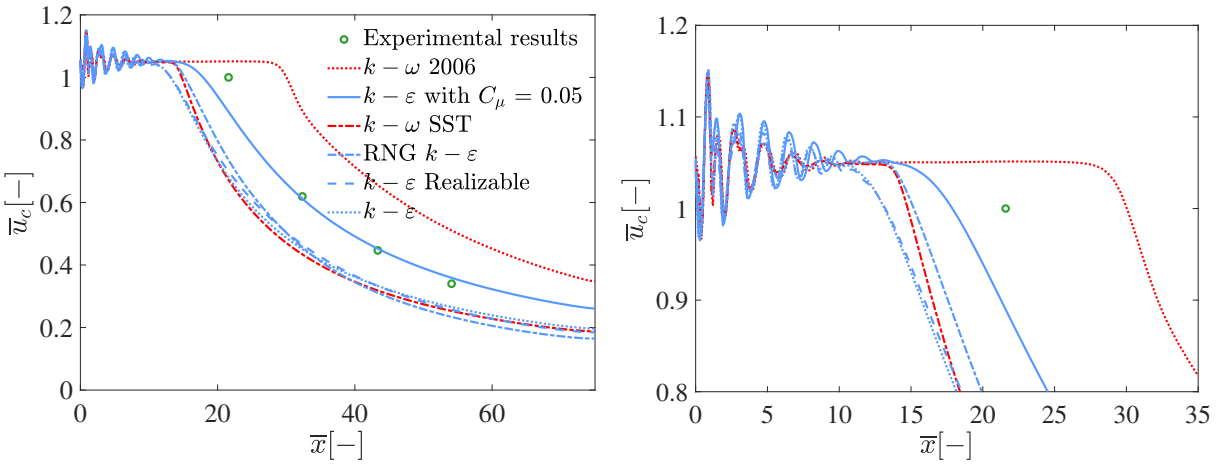

(a) Entire jet.

(b) Zoom on the potential core.

Figure 4.6: Supersonic jet in hot atmosphere: Comparison of the dimensionless axial centerline velocity for different models of turbulence with the experiments.

It can be first observed that the turbulence models behave differently from the case in cold atmosphere. However, some similarities can be inferred. The $k-\omega$ model with the Wilcox 2006 modification also overestimates the potential length in this set-up. However, the $k-\varepsilon$ based models no longer provide significantly better results. Their estimation of the velocity decay is however more accurate than the $k-\omega$ SST model. The RNG $k-\varepsilon$ estimates slightly better the flow than the other models with the standard coefficients. The $k-\varepsilon$ model taking into account the change of C_μ reproduces the flow the most accurately. The estimation of the potential length and of the velocity decay is indeed the closest to the experimental results.

To further validate these observations, the axial velocity profiles at multiple axial distances are plotted for each model in Figure 4.7. Self-similarity should be observed for axial distance over $30D_{\text{out}}$ [31].

Except for the $k-\varepsilon$ Realizable model, they all respect self-similarity. The $k-\omega$ 2006 also provides less reliable results. As expected, the $k-\omega$ SST, the RNG $k-\varepsilon$, and the $k-\varepsilon$ models present similar results with slight variations. The results of the $k-\varepsilon$ model with the adjusted C_μ stands out again. Self-similarity is indeed observed for all profiles along the axial centerline. The accuracy of this model is thus verified. Despite being less elegant, it is a good alternative to the correction of the $k-\varepsilon$ model.

The results with this turbulence model can be further studied. The influence of the temperature and of the lance height on the blowing are key results to better understand the BOF process. They are therefore investigated.

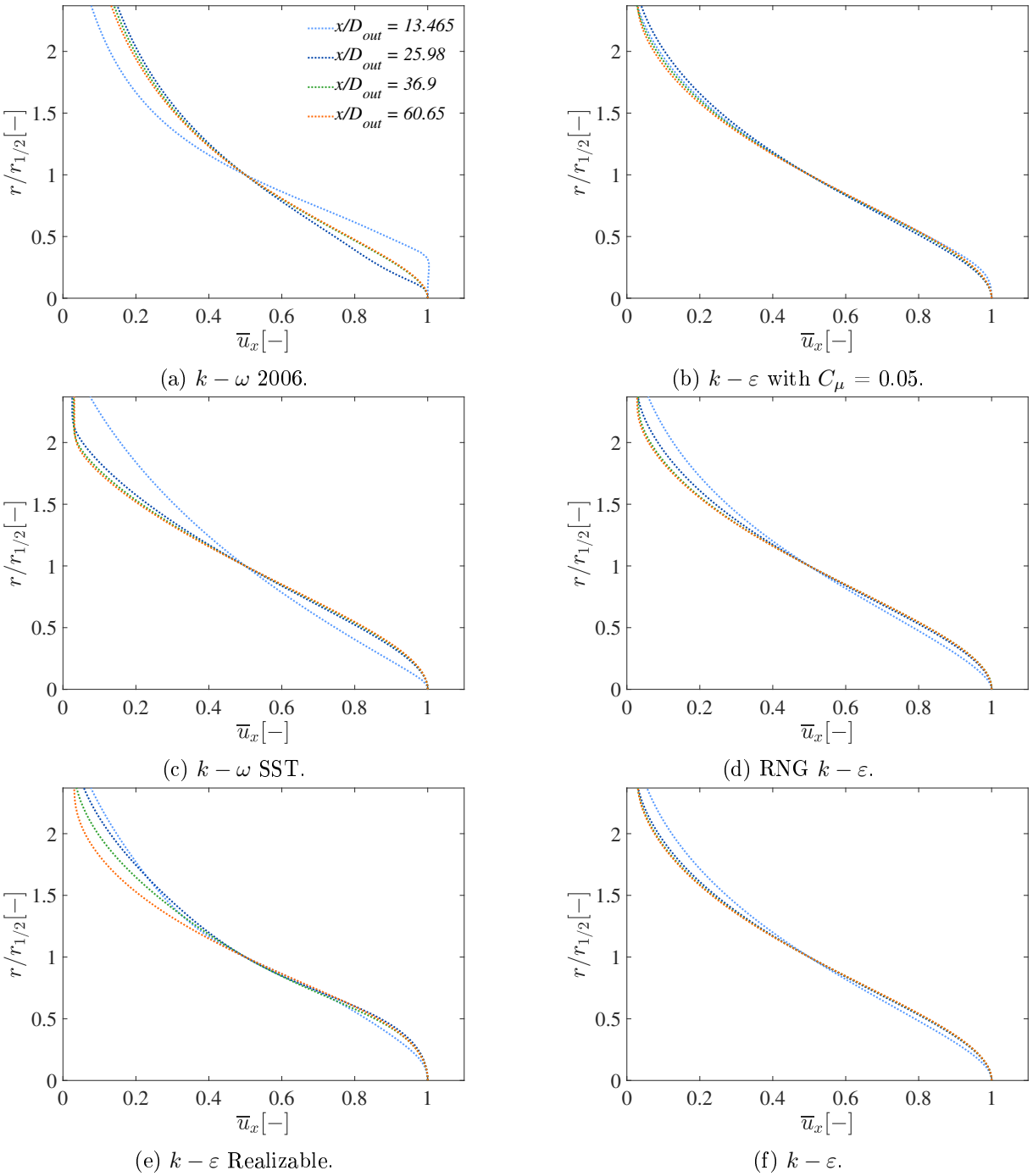

(a) $k-\omega$ 2006.

(b) $k-\varepsilon$ with $C_\mu = 0.05$.

(c) $k-\omega$ SST.

(d) RNG $k-\varepsilon$.

(e) $k-\varepsilon$ Realizable.

(f) $k-\varepsilon$.

Figure 4.7: Supersonic jet in hot atmosphere: Comparison of the dimensionless axial velocity profiles at multiple axial distance for different models of turbulence.

4.3 Results

The adequate parameters to model accurately the supersonic jet in a hot temperature field are identified. The latter is developed to reproduce the BOF environment. Consequently the influence of the temperature on the flow is highlighted. The results are also studied to understand the behavior of the flow at bath level. The characteristics of the jet at the nozzle outlet are interesting to identify the zones of damage of the lance as well.

Firstly, the dimensionless axial centerline velocity is compared with the reference results. They are illustrated in Figure 4.8. It can be seen that, as designed, the correlation of Ito and Muchi predicts precisely the flow. The correlation of Witze also provides a reliable estimation despite being developed for other configurations. Both correlations can therefore be used to validate further simulations for which experimental results are not available. The simulations conducted by Alam approximate better the potential core length than the current simulation. However, downstream of the nozzle, this study stands out. It indeed estimates accurately the velocity decay. This results is significant to accurately predict the flow at the bath level.

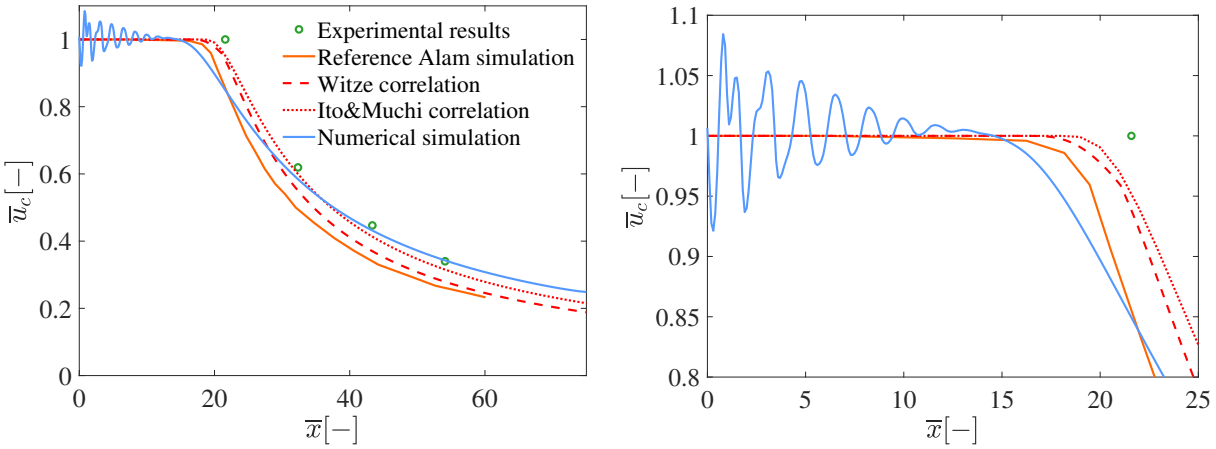

(a) Entire jet.

(b) Zoom on the potential core.

Figure 4.8: Supersonic jet in hot atmosphere: Comparison of the dimensionless axial centerline velocity from the simulation with the reference, experimental, analytical and numerical, results.

Oscillations can be observed along the entire potential core for this model. This might indicate a possible in-adaptation of the nozzle which results in shocks downstream. The numeric schlieren and the shadowgraph are studied to validate this observation. They are respectively displayed in Figure 4.9 and Figure 4.10.

As for the cold case, the range is adapted to obtain a clear image. Clear shocks along the entire potential length can then be observed. They start to propagate after the nozzle throat. The nozzle is therefore not adapted. As illustrated in Section 1, this is a consequence of a too high static pressure in the nozzle with respect to the ambiance. The total pressure in the reservoir should thus be adjusted. This configuration is less critical than an under-expanded nozzle. Then the lance tip is now longer cooled down by the flow and it erodes. Over-expanded nozzles are however not wanted as it decreases the performance. The investigation of the adequate value is left for future work.

(a) x-direction: Entire range.

(b) x-direction: Custom range.

(c) y-direction: Entire range.

(d) y-direction: Custom range.

Figure 4.9: Supersonic jet in hot atmosphere: Numeric schlieren at the nozzle exit.

(a) Entire range.

(b) Custom range.

Figure 4.10: Supersonic jet in hot atmosphere: Shadowgraph at the nozzle exit.

The axial velocity, the dynamic pressure and the temperature profiles are plotted for two lance heights in Figure 4.11. As mentioned in Section 1, the lance distance from the bath varies between 1.8m and 3m depending on the type of blowing sought. In Section 3.1, it is computed that it corresponds to a distance from the nozzle of $45D_{\text{out}}$ to $75D_{\text{out}}$.

A lance close to the bath results in a violent stirring jet. In this configuration, the carbon is oxidized. If the lance is higher, the jet is smoother and the other impurities react. Those characteristics of the jet can be observed in Figure 4.11.

At a lance distance of $45D_{\text{out}}$, the jet impacts the bath at a velocity of about 180m/s. This corresponds to the subsonic region. The jet is approximately 0.14m wide. If a lance of five nozzles is assumed and the coalescence of the jet neglected, this corresponds to an impacted area of 0.077m^2 or $909D_{\text{out}}^2$. In a higher configuration, the jet blows onto the bath at around 110m/s. A spreading of 0.25m is identified. This corresponds to an impacted area of 0.245m^2, or equivalently $2900D_{\text{out}}^2$. For comparison, the bath surface is $12272D_{\text{out}}^2$. Hence, between both configurations, the axial velocity decreases of slightly less than one third. Regarding the spreading of the jet, the impacted area is three times larger.

A similar evolution of the temperature profiles can be observed in Figure 4.11c. The closer the jet is to the bath, the lower is the temperature as the jet travels for a shorter time in the high temperature field. The influence of the temperature of the jet on the oxidation process has not been highlighted. Conclusions regarding the effects on the process therefore cannot be drawn.

The dynamic pressure, or $0.5\rho u^2$, is plotted in Figure 4.11b. As it has been observed, the further is the lance from the bath, the higher is the centerline velocity and the lower is the temperature of the jet. Consequently its density is larger and the dynamic pressure is higher. The difference between both configuration is significant. A high dynamic pressure leads to a deep penetration of the bath by the jet. The latter impacts the surface more violently. A lower lance thus, as expected, leads to a more penetrating, violent blowing.

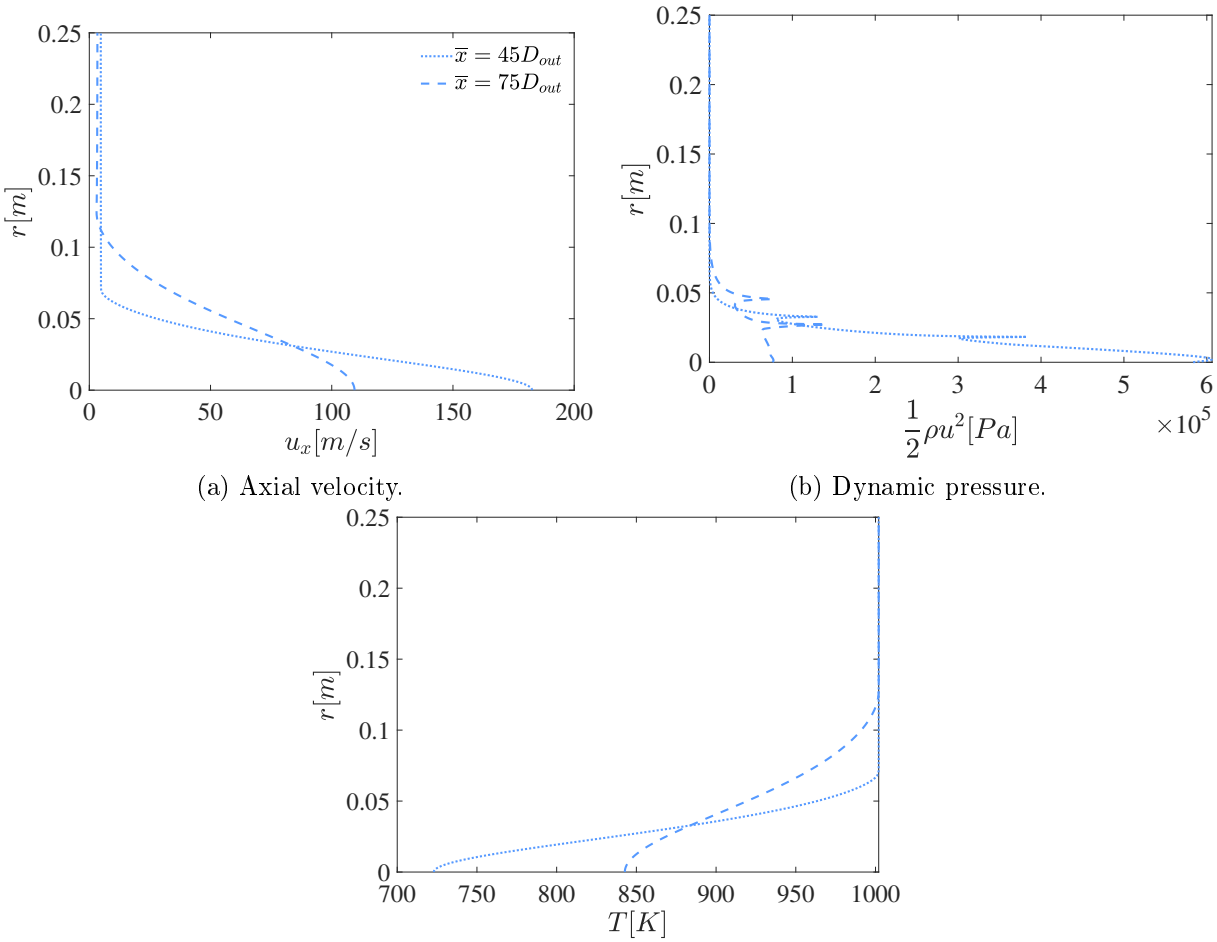

(a) Axial velocity.

(b) Dynamic pressure.

(c) Temperature.

Figure 4.11: Supersonic jet in hot atmosphere: Comparison of the axial velocity, dynamic pressure, and temperature profiles at the two lance heights.

These results should however be considered carefully. The BOF ambient temperature of 1900K is indeed not modeled. Here the ambiance is at 1002K. In a higher temperature field, the jet velocity decay is lower and the spreading is decreased. Consequently the jets impacts the bath at a higher velocity. The impacted area is lower. An insight at the influence of the temperature on the jet is taken to illustrate these expectations.

The model for the other temperatures is identical to the one with an atmosphere at 1002. The ambient temperature and the C_μ value are however adapted according to the experiments and Lebon's correction [32, 19].

The evolution of the centerline quantities are plotted against the experimental results for the different temperatures in Figure 4.12. In Figure 4.12a is represented the dimensionless axial centerline velocity. Firstly it can be mentioned that in the case at 285K, the velocity decay is not smooth. This is probably a consequence of the in-adaptation of the nozzle. Determining the adequate total pressure of the nozzle is therefore the first step that should be pursued in future works. Beside this off-behavior, the results predict reliably the flow.

As stated, the potential core length increases with temperature. Consequently, at the same axial distance, the axial velocity along the centerline is higher. This difference is significant for

small axial distance i.e., when the lance is close to the bath. The further the lance is from the bath, the less significant is the velocity difference due to ambient temperature.

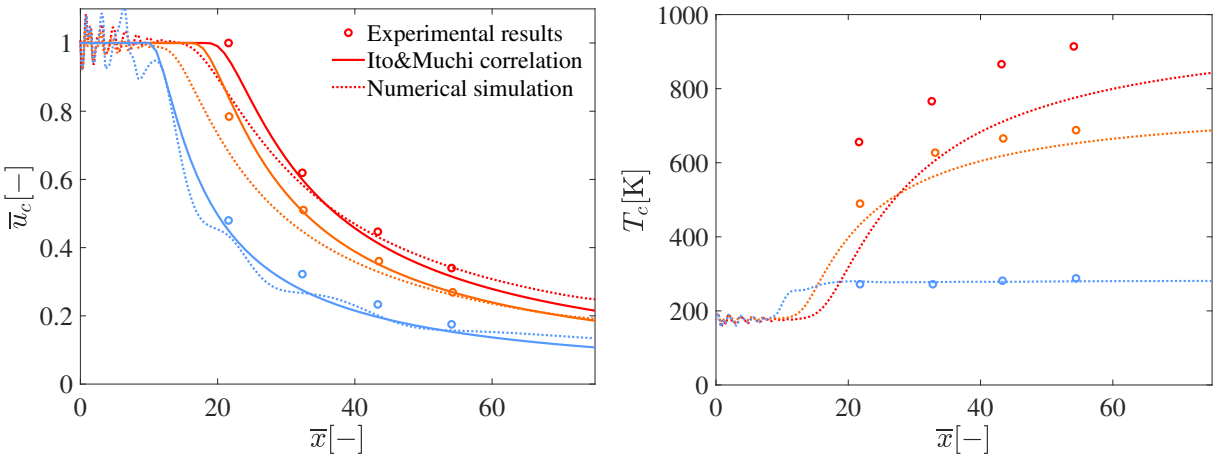

(a) Dimensionless axial centerline velocity.

(b) Centerline temperature.

Figure 4.12: Supersonic jet in hot atmosphere: Comparison of the centerline quantities for different ambient temperatures. The ambient temperature of 1002K is plotted in red, and of 285K in blue.

However, as it can be seen in Figure 4.12b, the temperature of the jet at the bath will largely differ. In fact, for the high lance configuration, the jet temperature reaches the ambient's. This might influence the oxidation process.

Also, for the jet in an atmosphere at 285K, the evolution of the temperature is accurately predicted. However, for the hotter cases, the temperature increase of the jet is underestimated. As explained by Alam, this large error takes root in the turbulence model. In the latter, the turbulent transport of heat is constant with temperature fluctuations. Nevertheless, for large temperature gradients, the heat transfer through the turbulent shear layer increases. Hence, the turbulent transport of heat should be adapted [13].

To highlight the impact of the temperature on the flow velocity, the profiles are plotted against each other for various axial distances in Figure 4.13. In the potential length, the profiles are similar. The nozzles indeed operate in identical conditions. The jet at the nozzle exit is therefore the same and the properties are kept throughout the entire potential core length. This observation can be useful to test the lance in in-adapted configurations. A first insight at the behavior of the jet can be taken at ambient temperature. Experiments in a hot temperature field are however necessary to identify the damage and erosion due to the contact with hot air.

The higher is the temperature field, the narrower and the faster is the jet. The BOF temperature is not easily controlled. In fact, most of the heat is released during the exothermic oxidation process. Adapting it is therefore slow and interferes with the first purpose of the BOF. Hence the lance height is adapted. Depending on the desired properties of the jet and on the current ambient temperature, the adequate lance distance from the bath can be derived. This observation shows the importance of developing a model from which guidelines for the operation can be inferred.

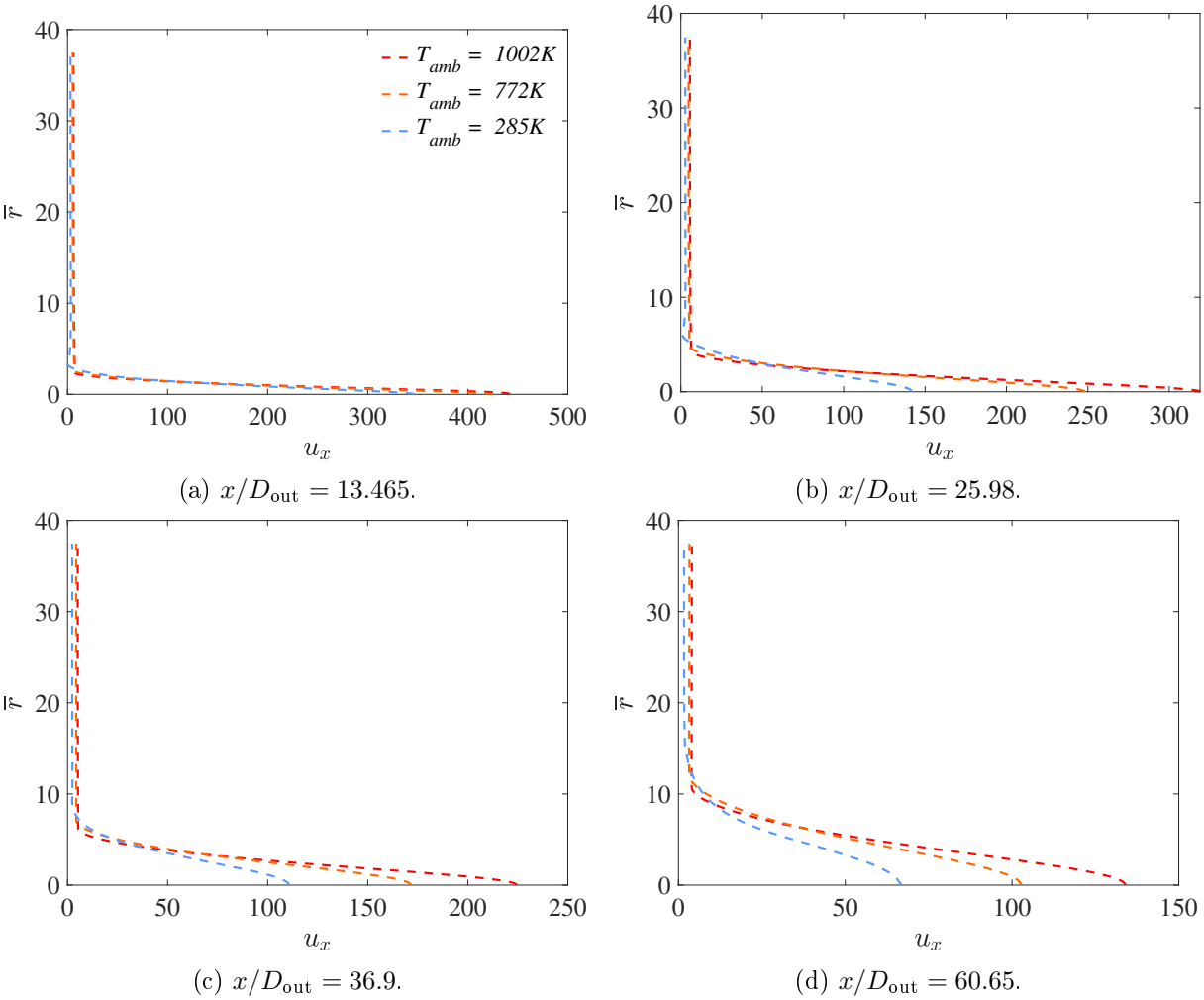

(a) $x/D_{\text{out}} = 13.465$.

(b) $x/D_{\text{out}} = 25.98$.

(c) $x/D_{\text{out}} = 36.9$.

(d) $x/D_{\text{out}} = 60.65$.

Figure 4.13: Supersonic jet in hot atmosphere: Comparison of the evolution of the axial velocity profiles at multiple axial distances for different ambient temperatures.

Additionally, the plots in Figure 4.13c and Figure 4.13d correspond to the range of lance heights. It can be seen that, despite being less significant, the differences between the ambient temperatures is not negligible. Hence the observations from Figure 4.11 must be taken carefully. An insight at the behavior of the jet at the bath level can be taken but no rigorous conclusion can be drawn.

The mixing layer's boundaries along with the half radius are plotted in Figure 4.14 for the different temperatures. The analytical expression expressed in Eq. (3.9) models the evolution of the half radius along the axial distance. The spreading rate and the virtual origins are listed in Table 4.2 for each temperature.

It can be seen that the virtual origin varies with temperature. In fact, the jets starts to spread after the potential length ends as turbulent entrainment begins. As the potential core length increases with temperature, the spreading starts at higher axial distances. Regarding the spreading rate, it is expected to decrease with an increase in the ambient temperature. In fact, the density of the ambient flow is lower. Consequently, the mass addition to the jet is lower and the growth rate of the turbulent mixing growth rate decreases. Hence the standard values of the turbulence model have been adjusted. This observations cannot be inferred from these simulations. In fact, the rate decreases between the ambiance at 772K and 1002K but not between 285K

and 772K. However it is previously highlighted in Figure 4.12a that the results in the current cold case are not reliable. The latter should therefore be accurately solved before drawing conclusions.

Table 4.2: Supersonic jet in hot atmosphere: Analytical expression of the half-radius evolution: The coefficients' values.

T_{amb}	S	$\overline{x}_0$
K	-	-
285	0.08	-3
772	0.09	5
1002	0.085	7.5

To conclude, a model for the supersonic jet in hot atmosphere is developed. Through the validation process, it is shown that the turbulence model plays a significant role in the accuracy of the predictions. Moreover it is highlighted that the standard models are not adequate for high temperature fluctuations. In fact, at high temperatures, due to the lower mass addition, the turbulence mixing growth rate decreases. For the $k-\varepsilon$, the C_μ value must be adapted. The most accurate way to take into account the influence of the temperature is to modify the turbulence model. However, the implementation is complex and another option is preferred. The value is adjusted according to Lebon's investigations. Consequently the flow is efficiently predicted. In the analysis of the results, it is however highlighted that the heat transfer through the turbulent shear layer is underestimated. The calculation of the turbulent transport of heat should therefore be adapted as well. Also the prescribed total pressure at the reservoir is too high leading to an non-adapted nozzle. The right value should thus be investigated.

The profiles at the bath level are studied. The sought characteristics of the jet in both high and low lance configurations are observed. The narrow, fast, penetrating jet at small distances from the bath and the wide, smooth and slower jet further from the lance are identified. Additionally, the influence of temperature on those profiles and on the centerline quantities is investigated. In a higher temperature field, at the same axial distance, the jet is narrower and faster. Depending on the current ambient temperature and on the sought properties of the jet, the lance height should therefore be adjusted throughout the process.

The modeling of a single supersonic jet in hot atmosphere with opensource tools is successful. This simplified model could be used to identify some recommendations. However, the temperature of the ambiance should be adapted to match the BOF's. Moreover, the ambient composition can be more closely reproduced. This would however require a change of the solver to handle multi-phase flows.

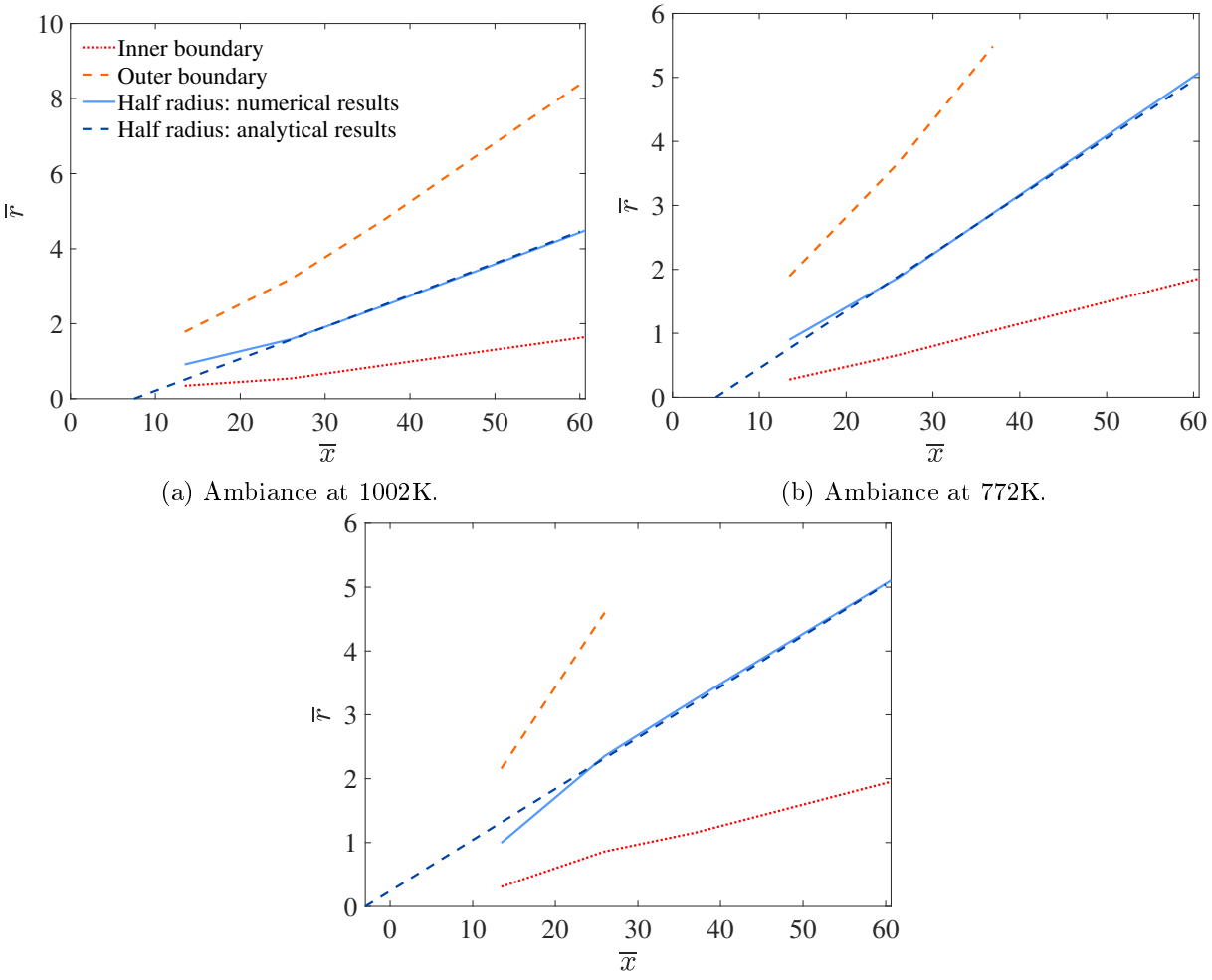

(a) Ambiance at 1002K.

(b) Ambiance at 772K.

(c) Ambiance at 285K.

Figure 4.14: Supersonic jet in hot atmosphere: Evolution of the mixing layer's boundaries and of the half radius over the axial distance for different ambient temperatures.

Conclusions

To better understand the operation of the Basic Oxygen Furnace during the steel making process, numerous experiments and modeling have been carried out. The previous numerical simulations have all been conducted on licensed software. The main objective of this paper is thus to investigate open source tools and to develop expertise in these materials. The Gmsh and OpenFOAM® software are selected to conduct the simulations [1, 20].

Beforehand, the context of use of the oxygen lance is presented. The different steps of the blowing are described. These are determined by the lance height above the bath. The latter impacts the blowing, the formation of phases, and the oxidation. Hence the supersonic jet is characterized to identify different zones. The potential core length i.e., the distance during which the velocity and the pressure stays constant, is taken as a reference point for the validation of the tools. This characteristic of the flow is indeed easy to monitor.

Afterwards, the available results on which the validation of the tools is based are presented. The experiments considered in this study are carried out by Eggers and Sumi respectively for the cold atmosphere, at 291.66K, and the hot atmosphere, at 285K, 772K, and 1002K [8, 16]. From these experiments, the correlations of Witze and of Ito and Muchi are derived [9, 10]. Additionally, they were reproduced numerically by the NASA and by Alam[11, 13]. These results are taken as a reference for the validation of the open source tools.

Thus, firstly, the cold jet in cold atmosphere is modeled. The set-up is presented. During the validation process, it is shown that structured meshes provide significantly better results than unstructured's. Also, the choice of the type of boundary conditions has little influence on the flow. Most importantly, setting a freestream in the ambiance does not impact considerably the jet. The available turbulence models are compared as well. It is identified that the $k-\varepsilon$ provides the best results. The value of C_μ is adjusted to 0.06 to improve the accuracy of the predictions of turbulent entrainment. During this validation process, an additional validation methodology is developed. For a round jet, the profiles at multiple axial distances must be self-similar. This property is thus additionally checked. To characterize the flow, numerous parameters can be investigated. The velocity profiles, the boundaries of the mixing layer, the supersonic length, etc. can be identified. These materials are useful to understand the influence of the jet during the oxidation process.

Secondly, the high temperature field is considered. Due to the high temperature gradients, the thermophysical properties are adapted to take these fluctuations into account. Moreover, to consider these important variations, the $k-\varepsilon$ should be adapted. However, this modification is complex to implement in OpenFOAM®. This indeed requires a deep change of the solver as the temperature is not transmitted in the definition of the model. This task is beyond the scope of this work but is introduced for further developments. Therefore, as an alternative, as for the cold case, the C_μ constant is adjusted. This option also provides accurate results despite being less elegant. The influence of the ambient temperature on the flow is then highlighted. It is shown that the temperature field has a similar influence of the flow as the lance height. The higher is the ambient temperature or the lower is the lance, the narrower and the faster is the jet. The lance height can therefore be adjusted to counteract the influence of the temperature on the jet properties.

To conclude, knowledge has been gathered about the industrial context and on reference experimental, analytical, and numerical results. These provides a insight into the possibilities and challenges of future work. Also, guidelines have been drawn to efficiently set-up the model of a supersonic jet with Gmsh and OpenFOAM®. Moreover an additional validation method is introduced besides the comparison of the potential core length. The self-similarity of the axial velocity profiles is checked to verify the reliability of the model. Consequently the use of the open source tools is validated through this work. It has been shown that reliable results can be obtained to simulate a cold supersonic jet in hot atmosphere.

This setup is the first step towards the implementation of models including more characteristics of the BOF environment. First of all, the temperature of the BOF should be accurately modeled. It has been highlighted in this work that either the C_μ value of the $k-\varepsilon$ model must be adapted or the turbulence model must be modified to take into account the temperature fluctuations. The latter would be an elegant method worth implementing. Also the calculations of the heat transfer through the shear layer should be adapted with the temperature variations. Additionally, to get a closer reproduction of the ambiance, the composition of the air can be defined. Different species are then present in the simulation. The mixing between the different compositions is considered. The post-combustion process can also be studied. This would require the use of combustion solvers such as *rhoReactingFoam* [20]. Moreover the bath can be modeled. Furthermore, the other phases, the slag and the emulsion, can be added to the model. These improvements of the modeling would require multi-phase solvers.

One of the other next simulations that could be of great interest is the study of the coalescence of the jets. This has been simulated once [17]. This corresponds to a 3-dimensional model. Since the simulations without a nozzle were unsuccessful, the geometry cannot be simplified. Also, predictions made on unstructured meshes are inaccurate. A 3D structured mesh including the nozzle should therefore be generated. Attempts have been started but have not been pursued due the lack of time. The model generated in Gmsh is illustrated in Appendix B.
The first encountered difficulty is the definition of the regions. In order to incorporate smoothly the nozzle outlet into the mesh, different surfaces and volumes must be build. Due to the definition of transfinite elements in Gmsh, these multiple volumes have to be translated across the entire domain. Over twenty volumes are then generated.
Consequently, the second issue has arisen. The mesh does not pass the *checkMesh* tool. All the warnings are activated. Also, the translation of the mesh from Gmsh to OpenFOAM® did not proceed smoothly. Because of the complexity, the mesh quality could not be improved. This work is therefore left for the future.

The model can therefore be improved to get a closer reproduction of the BOF environment. This would lead to a greater understanding of the complex phenomena taking place. Conclusions could be drawn and the lance tip design could be adapted to optimize both the process and its service life. Consequently a move towards a greener steel could be taken. The first step towards these work is achieved through this study.

Acknowledgments

First of all, I would like to thank my academic supervisor Pr. Vincent Terrapon. I am infinitely grateful to him for sharing his expertise, offering his guidance, and providing his support. His help to navigate through this work was precious.

Also I would like to thank Dr. Jean-Philippe Thomas. His warm welcoming at Soudobeam S.A., his invaluable theoretical insights, and his countless suggestions have been key elements to the accomplishment of this work. His valuable remarks of improvements for this report guided me through the writing.

At the same time, I would like to thank the entire team at Soudobeam S.A. who made me feel welcome. By following them during their working day, they offered me an priceless insight into their work that helped me understand the challenges of manufacturing.

Additionally I would like to thank the team of the Multiphysic and Turbulent Flow Computation at the University of Liège. I cannot stress enough how their help to master the various tools was meaningful.

I would like to thank Dr. Marc Duflot for his feedback on the report. His precious remarks and suggestions have been incredibly helpful.

Finally I would like to thank my relatives for their unfailing patience and unconditional support. Their presence throughout my studies is invaluable.

A Supersonic jet in hot atmosphere: nozzle coordinates

In Table A.1 are listed the nozzle coordinates considered for the simulation of a single supersonic jet in hot atmosphere. The outlet diameter D_{out} is equal to $9.2e^{-3}$m.

Table A.1: Supersonic jet in hot atmosphere: Coordinates of the nozzle and the reservoir.

Axial coordinate x [m]	Radial coordinate y [m]
-7.2222 $\cdot D_{\text{out}}$	0.7896 $\cdot D_{\text{out}}$
-4.0276 $\cdot D_{\text{out}}$	0.7896 $\cdot D_{\text{out}}$
-3.9288 $\cdot D_{\text{out}}$	0.7893 $\cdot D_{\text{out}}$
-3.8390 $\cdot D_{\text{out}}$	0.7879 $\cdot D_{\text{out}}$
-3.7385 $\cdot D_{\text{out}}$	0.7863 $\cdot D_{\text{out}}$
-3.6499 $\cdot D_{\text{out}}$	0.7794 $\cdot D_{\text{out}}$
-3.5347 $\cdot D_{\text{out}}$	0.7670 $\cdot D_{\text{out}}$
-3.4401 $\cdot D_{\text{out}}$	0.7519 $\cdot D_{\text{out}}$
-3.3496 $\cdot D_{\text{out}}$	0.7343 $\cdot D_{\text{out}}$
-3.2492 $\cdot D_{\text{out}}$	0.7107 $\cdot D_{\text{out}}$
-3.1412 $\cdot D_{\text{out}}$	0.6824 $\cdot D_{\text{out}}$
-3.0405 $\cdot D_{\text{out}}$	0.6521 $\cdot D_{\text{out}}$
-2.9467 $\cdot D_{\text{out}}$	0.6224 $\cdot D_{\text{out}}$
-2.8492 $\cdot D_{\text{out}}$	0.5869 $\cdot D_{\text{out}}$
-2.7411 $\cdot D_{\text{out}}$	0.5540 $\cdot D_{\text{out}}$
-2.6444 $\cdot D_{\text{out}}$	0.5206 $\cdot D_{\text{out}}$
-2.5438 $\cdot D_{\text{out}}$	0.4864 $\cdot D_{\text{out}}$
-2.4441 $\cdot D_{\text{out}}$	0.4581 $\cdot D_{\text{out}}$
-2.3499 $\cdot D_{\text{out}}$	0.4382 $\cdot D_{\text{out}}$
-2.2489 $\cdot D_{\text{out}}$	0.4293 $\cdot D_{\text{out}}$
-2.1477 $\cdot D_{\text{out}}$	0.4327 $\cdot D_{\text{out}}$
-2.0449 $\cdot D_{\text{out}}$	0.4391 $\cdot D_{\text{out}}$
-1.9427 $\cdot D_{\text{out}}$	0.4426 $\cdot D_{\text{out}}$
-1.8456 $\cdot D_{\text{out}}$	0.4487 $\cdot D_{\text{out}}$
-1.7438 $\cdot D_{\text{out}}$	0.4559 $\cdot D_{\text{out}}$
-1.6420 $\cdot D_{\text{out}}$	0.4625 $\cdot D_{\text{out}}$
-1.5448 $\cdot D_{\text{out}}$	0.4690 $\cdot D_{\text{out}}$
-1.4411 $\cdot D_{\text{out}}$	0.4750 $\cdot D_{\text{out}}$
-1.3481 $\cdot D_{\text{out}}$	0.4594 $\cdot D_{\text{out}}$
-1.2362 $\cdot D_{\text{out}}$	0.4783 $\cdot D_{\text{out}}$
-1.1388 $\cdot D_{\text{out}}$	0.4804 $\cdot D_{\text{out}}$

Continued on next page

Table A.1 – *Continued from previous page*

Axial coordinate x [m]	Radial coordinate y [m]
-1.0413 $\cdot D_{\text{out}}$	0.4813 $\cdot D_{\text{out}}$
-0.9451 $\cdot D_{\text{out}}$	0.4842 $\cdot D_{\text{out}}$
-0.8360 $\cdot D_{\text{out}}$	0.4904 $\cdot D_{\text{out}}$
-0.7465 $\cdot D_{\text{out}}$	0.4937 $\cdot D_{\text{out}}$
-0.6480 $\cdot D_{\text{out}}$	0.4963 $\cdot D_{\text{out}}$
-0.5444 $\cdot D_{\text{out}}$	0.4981 $\cdot D_{\text{out}}$
-0.4404 $\cdot D_{\text{out}}$	0.4992 $\cdot D_{\text{out}}$
-0.3410 $\cdot D_{\text{out}}$	0.4997 $\cdot D_{\text{out}}$
-0.2433 $\cdot D_{\text{out}}$	0.4999 $\cdot D_{\text{out}}$
-0.1451 $\cdot D_{\text{out}}$	0.5000 $\cdot D_{\text{out}}$
0.0000	0.5000 $\cdot D_{\text{out}}$

B 3D model: Generation in Gmsh [1]

The attempt at building a 3-dimensional model is illustrated in Figure B.1 and Figure B.2 for the geometry, and in Figure B.3 and Figure B.4 for the mesh. A zoom on the mesh in the nozzle is represented in Figure B.5. The different zones that had to be defined to incorporate smoothly the nozzle exit in the mesh can be identified.

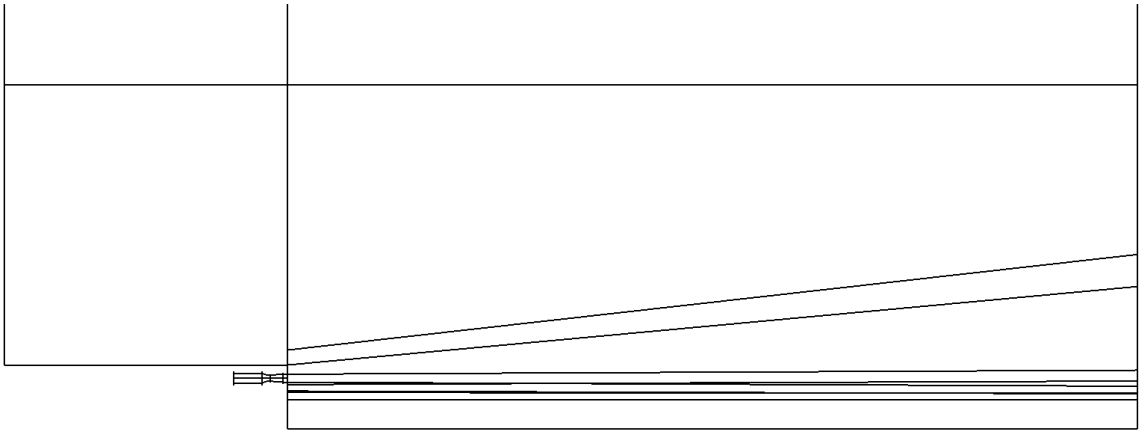

Figure B.1: 3D model: Geometry along the x- and y-axis.

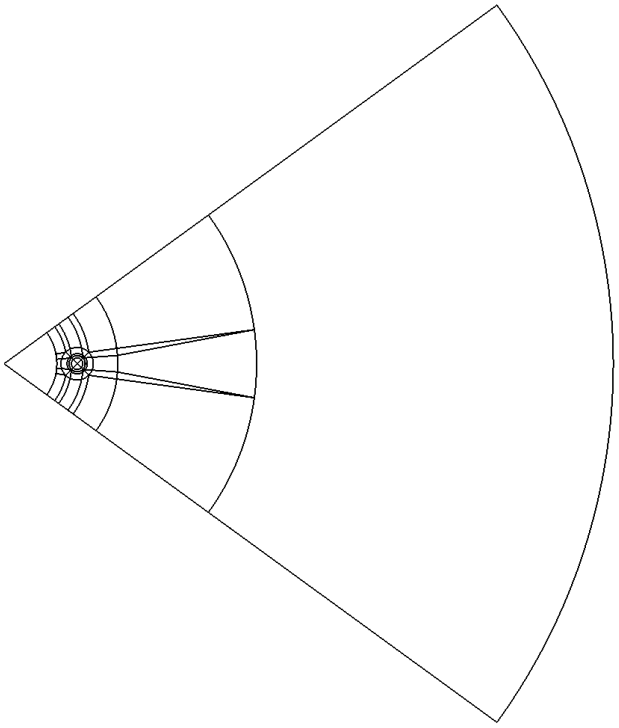

Figure B.2: 3D model: Geometry along the y- and z-axis.

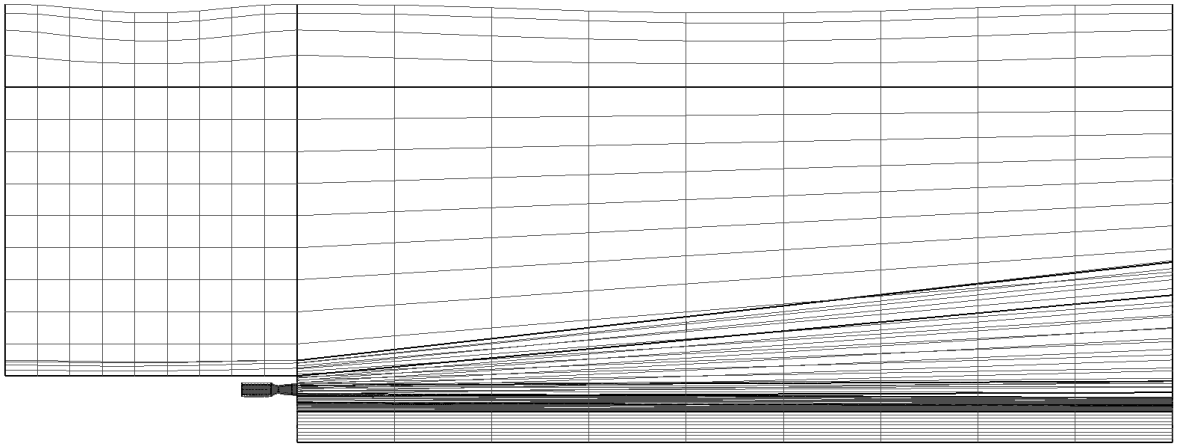

Figure B.3: 3D model: Mesh along the x- and y-axis.

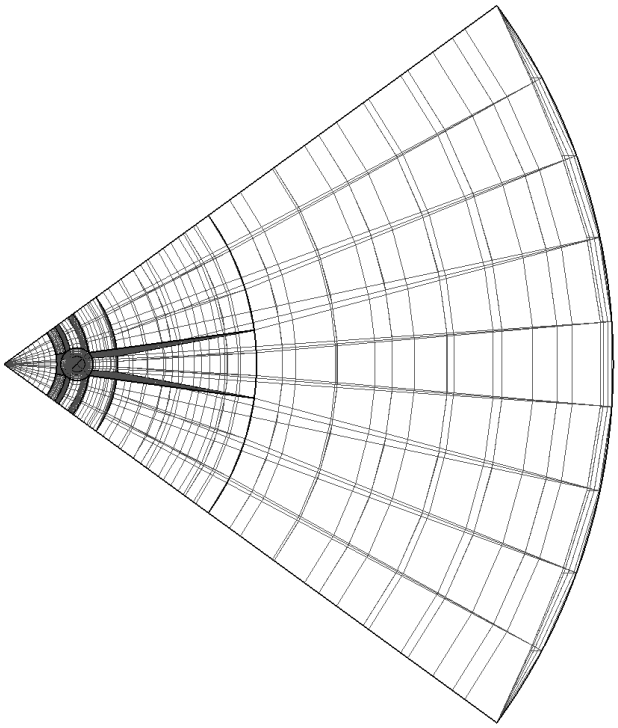

Figure B.4: 3D model: Mesh along the y- and z-axis.

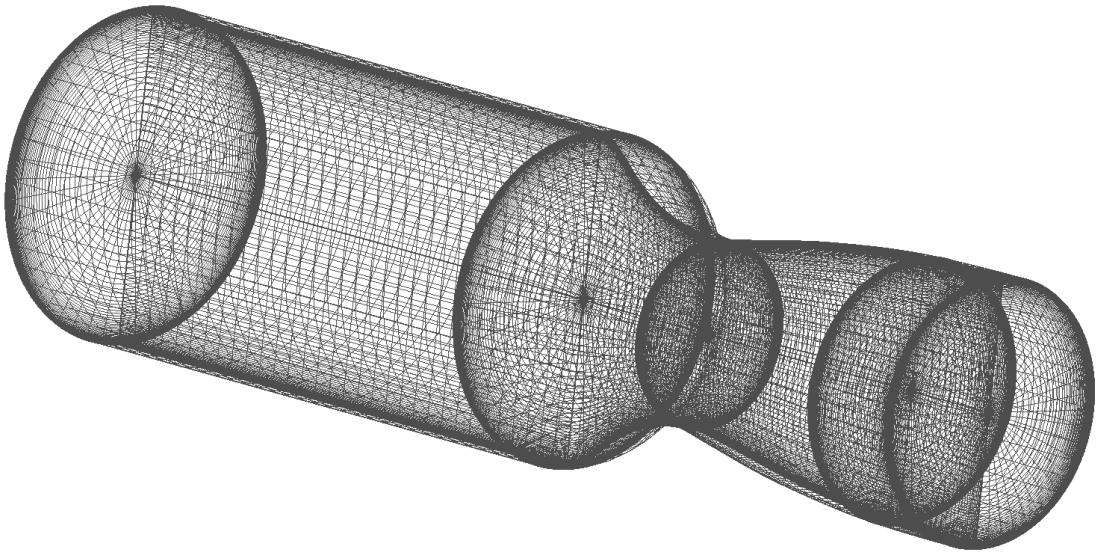

Figure B.5: 3D model: Mesh in the nozzle.

References

[1] C. Geuzaine and J. Remacle, "Gmsh: A 3-D finite element mesh generator with built-in pre- and post-processing facilities," *International Journal for Numerical Methods in Engineering*, vol. 79, pp. 1309–1331, Sept. 2009.

[2] MINMET, "Electric arc furnace in stainless steel process," Apr. 2020.

[3] JNE Automation, "Basic Oxygen Furnace Automated Tapping System."

[4] R. J. Fruehan and AISE Steel Foundation, eds., *The making, shaping, and treating of steel*. Pittsburgh, PA: AISE Steel Foundation, 11th ed ed., 1998.

[5] M. Evestedt and A. Medvedev, "GAS JET IMPINGING ON LIQUID SURFACE: CAVITY SHAPE MODELLING AND VIDEO-BASED ESTIMATION," *IFAC Proceedings Volumes*, vol. 38, no. 1, pp. 1065–1070, 2005.

[6] Y. N. Doh, *Modélisation multiphysique du convertisseur d'aciérie*. PhD thesis, 2012.

[7] M. Li, Q. Li, S. B. Kuang, and Z. Zou, "Coalescence Characteristics of Supersonic Jets From Multi-Nozzle Oxygen Lance in Steelmaking BOF," *steel research international*, vol. 86, pp. 1517–1529, Dec. 2015.

[8] J. M. Eggers, "Velocity Profiles and Eddy Viscosity Distributions Downstream of a Mach 2.22 Nozzle Exhausting to Quiescent Air," *NASA Technical Note D-3601*, Sept. 1966.

[9] P. O. Witze, "Centerline Velocity Decay of Compressible Free Jets," *AIAA Journal*, vol. 12, pp. 417–418, Apr. 1974.

[10] S. Ito and I. Muchi, "Transport Phenomena of Supersonic Jet in Oxygen Top Blowing Converter," *Tetsu-to-Hagane*, vol. 55, no. 13, pp. 1152–1163, 1969.

[11] C. Rumsey, "ACSSJ: Axisymmetric Cold Supersonic Jet," May 2024.

[12] V. Dippold, "Seiner Nozzle with Mach 2.0, Heated Jet Flow."

[13] M. Alam, J. Naser, and G. A. Brooks, "Cfd simulation of supersonic oxygen jet behaviour inside a high temperature field," 2009. Publisher: [object Object].

[14] W. Sutherland, "LII. *The viscosity of gases and molecular force*," *The London, Edinburgh, and Dublin Philosophical Magazine and Journal of Science*, vol. 36, pp. 507–531, Dec. 1893.

[15] T. C. Allison, "NIST-JANAF Thermochemical Tables - SRD 13," Jan. 2013.

[16] I. Sumi, Y. Kishimoto, Y. Kikuchi, and H. Igarashi, "Effect of High-temperature Field on Supersonic Oxygen Jet Behavior," *ISIJ International*, vol. 46, no. 9, pp. 1312–1317, 2006.

[17] I. Klioutchnikov, H. Olivier, and J. Odenthal, "Numerical investigation of coaxial jets entering into a hot environment," *Computers & Fluids*, vol. 86, pp. 490–499, Nov. 2013.

[18] "Procedure for Estimation and Reporting of Uncertainty Due to Discretization in CFD Applications," *Journal of Fluids Engineering*, vol. 130, no. 7, p. 078001, 2008.

[19] G. S. B. Lebon, *Unstructured finite volume algorithms for compressible multiphase flow*. PhD thesis, 2011.

[20] C. Greenshields, *OpenFOAM v8 User Guide*. the openfoam foundation ed., 2020.

[21] The Euopean Steel Association, "What is steel and how is steel made ?," Mar. 2020.

[22] World Steel association, *The Steel Story*. 2013.

[23] ArcelorMittal, "Les départements industriels," 2024.

[24] M. Bramat, C. Mayer, and M. Villeneuve, *Technologie des métaux: contrôles et essais des soudures*. Soudage, Repentigny (Canada), Bruxelles, Paris: R. Goulet diff. De Boeck, 2008.

[25] A. V. Nguyen and G. M. Evans, "Computational fluid dynamics modelling of gas jets impinging onto liquid pools," *Applied Mathematical Modelling*, vol. 30, pp. 1472–1484, Nov. 2006.

[26] S. Koria, "Fundamentals of Converter Steelmaking Technology," Mar. 2011.

[27] B. T. Maia, R. K. Imagawa, A. C. Petrucelli, and R. P. Tavares, "Effect of blow parameters in the jet penetration by physical model of BOF converter," *Journal of Materials Research and Technology*, vol. 3, pp. 244–256, July 2014.

[28] M. Alam, G. Irons, G. Brooks, A. Fontana, and J. Naser, "Inclined Jetting and Splashing in Electric Arc Furnace Steelmaking," *ISIJ International*, vol. 51, no. 9, pp. 1439–1447, 2011.

[29] S. S. Park, N. Dyussekenov, and H. Sohn, "The Penetration Behavior of an Annular Gas–Solid Jet Impinging on a Liquid Bath: Comparison with a Conventional Circular Jet," *Metallurgical and Materials Transactions B*, vol. 41, pp. 51–62, Feb. 2010.

[30] H.-J. Odenthal, U. Falkenreck, and J. Schlüter, "CFD Simulation of Multiphase Melt FLows in Steelmaking Converters," Sept. 2006.

[31] S. B. Pope, *Turbulent flows*. Cambridge: Cambridge University Press, 2000. OCLC: 1181578420.

[32] I. Sumi, G. Okuyama, S. Nabeshima, H. Matsuno, and Y. Kishimoto, "Behavior of Top-Blown Jet under Reduced Pressure," *ISIJ International*, vol. 47, no. 1, pp. 73–79, 2007.

[33] C. J. Shoemaker, "Performance of Seven Semicircular Lift-Producing Nozzles," *NASA Technical Note D-2731*, Apr. 1965.

[34] G. Kleinstein, "Mixing in turbulent axially symmetric free jets," *Journal of Spacecraft and Rockets*, vol. 1, pp. 403–408, July 1964.

[35] K. S. Abdol-Hamid, S. P. Pao, S. J. Massey, and A. Elmiligui, "Temperature Corrected Turbulence Model for High Temperature Jet Flow," *Journal of Fluids Engineering*, vol. 126, pp. 844–850, Sept. 2004.

[36] H. G. Weller, G. Tabor, H. Jasak, and C. Fureby, "A tensorial approach to computational continuum mechanics using object-oriented techniques," *Computers in Physics*, vol. 12, pp. 620–631, Nov. 1998.

[37] C. Geuzaine and J. Remacle, *Gmsh Reference Manual for Gmsh 4.13.1*. May 2024.

[38] W. Polifke, *Simulation of Thermo-Fluids with Open Source Tools*. PhD thesis, Technical University of Munich, Dec. 2023.

[39] B. Zang, V. Us, H. Lim, X. Wei, and T. New, "An assessment of OpenFOAM solver on RANS simulations of round supersonic free jets," *Journal of Computational Science*, vol. 28, pp. 18–31, Sept. 2018.

[40] P. P. Nair, V. Narayanan, A. Suryan, and H. D. Kim, "Prediction and visualization of supersonic nozzle flows using OpenFOAM," *Journal of Visualization*, vol. 25, pp. 1227–1247, Dec. 2022.

[41] B. Zang, U. S. Vevek, and T. H. New, "RANS Simulation of Over- and Under-expanded Beveled Nozzle Jets Using OpenFOAM," in *31st International Symposium on Shock Waves 2* (A. Sasoh, T. Aoki, and M. Katayama, eds.), pp. 1155–1162, Cham: Springer International Publishing, 2019.

[42] "Tips and tricks in OpenFOAM®."

[43] R. Nichols, *Turbulence Models and Their Application to Complex Flows.*

[44] D. C. Wilcox, "Formulation of the k-w Turbulence Model Revisited," *AIAA Journal*, vol. 46, pp. 2823–2838, Nov. 2008.

[45] A. Rona and X. Zhang, "Time accurate numerical study of turbulent supersonic jets," *Journal of Sound and Vibration*, vol. 270, pp. 297–321, Feb. 2004.

[46] C. F. Chenault, P. S. Beran, and R. D. W. Bowersox, "Numerical Investigation of Supersonic Injection Using a Reynolds-Stress Turbulence Model," *AIAA Journal*, vol. 37, pp. 1257–1269, Oct. 1999.